

Corrosion Mechanisms of Mild Steel in Weak Acids

A dissertation presented to
the faculty of
the Russ College of Engineering and Technology of Ohio University

In partial fulfillment
of the requirements for the degree
Doctor of Philosophy

Thu N.B. Tran

August 2014

© 2014 Thu N.B. Tran. All Rights Reserved.

This dissertation titled
Corrosion Mechanisms of Mild Steel in Weak Acids

by

THU N.B. TRAN

has been approved for
the Department of Chemical and Biomolecular Engineering
and the Russ College of Engineering and Technology by

Srdjan Nesic

Professor of Chemical and Biomolecular Engineering

Dennis Irwin

Dean, Russ College of Engineering and Technology

ABSTRACT

TRAN, THU N.B., Ph.D., August 2014, Chemical Engineering

Corrosion Mechanisms of Mild Steel in Weak Acids

Director of Dissertation: Srdjan Nestic

The corrosion of mild steel in the presence of weak acids is a challenge for the oil and gas industry. Weak acids, such as carbonic acid (in CO₂ corrosion) and acetic acid, are reported to accelerate the cathodic reaction, but there is still little agreement as to their role in corrosion mechanisms. Although assumed in many studies, there is no proof that direct reduction of these weak acids occurs and needs to be taken into account. Therefore, the intent of this research is to determine whether these weak acids mainly provide hydrogen ions via their dissociation, with resultant hydrogen ions being directly reduced at the steel surface, or if the direct reduction of weak acids is also important.

Electrochemical techniques including linear polarization resistance (LPR), electrochemical impedance spectroscopy (EIS), and polarization sweeps were used to investigate the corrosion mechanisms. The experiments began with acetic acid, a low-molecular-weight weak organic acid commonly found in oil and gas production. The results suggested that the direct reduction of acetic acid is negligible at the steel surface. Similar results were obtained for carbonic acid, i.e., the direct reduction of carbonic acid was insignificant compared to the reduction of hydrogen ions. The corrosion mechanisms for other weak acids such as formic acid, water and hydrogen sulfide were also explored. Finally, an electrochemical model was proposed using FREECORP as a platform, developed by the Institute for Corrosion and Multiphase Technology.

DEDICATION

To My Family

ACKNOWLEDGMENTS

First, I wish to express my extreme gratitude to Dr. Srdjan Nestic, for his guidance and support during my Ph.D. studies. His passion, knowledge, and amazing energy have inspired me for the last four and a half years. He is a great professor, from whom I learned to cultivate a critical mind, and to ask questions.

I would like to acknowledge my project leader, Bruce Brown who assisted me with the experimental work and gave valuable suggestions for my research. I feel fortunate to have him as a project leader.

Dr. David Young provided expert guidance in chemistry, and also care, help, and kindness. I will never forget his help during my first days in the United States.

The laboratory technicians at the Institute for Corrosion and Multiphase Technology (ICMT), especially Alexis Barxias and Cody Shafer were immensely helpful.

The academic advice of Dr. Marc Singer, and Dr. Yoon-Seok Choi is greatly appreciated, as is the assistance of Dr. Bernard Tribollet at the Laboratoire Interfaces et Systèmes Electrochimiques (LISE), University Pierre and Marie Curie for the work conducted in France.

Last but not least, I would like to thank all the staff and students at ICMT for creating a wonderful working environment.

TABLE OF CONTENTS

	Page
Abstract.....	3
Dedication.....	4
Acknowledgments.....	5
List of Tables	8
List of Figures.....	10
Chapter 1: Introduction.....	18
Chapter 2: Literature review	23
2.1 Basics of CO ₂ corrosion process.....	23
2.2 Key parameters affecting CO ₂ corrosion mechanism.....	26
2.2.1 Effect of pH.....	26
2.2.2 Effect of flow	26
2.2.3 Effect of temperature	28
2.2.4 Effect of partial pressure of CO ₂	28
2.3 Direct reduction vs. buffering effect mechanism in CO ₂ corrosion.....	30
2.4 Direct reduction vs. buffering effect in acetic acid corrosion.....	36
Chapter 3: Research objectives and hypotheses	43
3.1 Research objectives.....	43
3.2 Hypotheses.....	43
3.2.1 HAc corrosion.....	43
3.2.2 CO ₂ corrosion.....	45
Chapter 4: Methodology and experimental design.....	50
4.1 Methodology.....	50
4.2 Experimental setup.....	53
4.3 Test matrix and experimental procedures	56
4.3.1 HAc corrosion.....	56
4.3.2 CO ₂ corrosion.....	59
Chapter 5: Results and discussions.....	66
5.1.1 Introduction.....	66

	7
5.1.2 Results and Discussion	66
5.1.3 Conclusions.....	75
5.2 CO ₂ corrosion mechanism	76
5.2.1 Introduction.....	76
5.2.2 Results and discussion	76
5.2.3 Conclusions.....	86
5.3 Corrosion mechanism of mild steel in other weak acids	87
5.3.1 Formic acid	87
5.3.2 Hydrogen sulfide.....	89
5.3.3 Water.....	95
Chapter 6: Electrochemical corrosion model prediction	97
6.1 Introduction.....	97
6.2 Theory of FREECORP – direct reduction model	98
6.2.1 Chemical reactions.....	98
6.2.2 Electrochemical reactions.....	99
6.3 Theory of modified FREECORP–buffering effect model	104
6.3.1 Cathodic reaction	104
6.3.2 Anodic reaction.....	105
6.4 Comparison between the models and experimental data.....	106
6.5 Conclusions.....	123
Chapter 7: Conclusions and recommendations.....	124
7.1 Conclusions.....	124
7.1.1 Corrosion mechanism of mild steel in aqueous HAc environment	124
7.1.2 Corrosion mechanism of mild steel in aqueous CO ₂ environment.	124
7.1.3 Corrosion mechanism of mild steel in weak acid environment.....	125
7.1.4 Corrosion prediction model	125
7.2 Recommendations for future research	126
Appendix A: Corrosion rate calculation	139
Appendix B: Equipment improvement and test reproducibility.....	140
Appendix C: Permission to reproduce figures from NACE international	154

LIST OF TABLES

	Page
Table 1: Chemical and electrochemical reactions involved in the CO ₂ corrosion process	24
Table 2: Chemical composition of carbon steel X65 (mass percent)	52
Table 3: Chemical composition of stainless steel SS304 (mass percent)	52
Table 4: Chemical composition of stainless steel Ni200 (mass percent).....	52
Table 5: Test matrix to test the effect of HAc concentration on the charge transfer current at pH4.....	56
Table 6: Test matrix to test the effect of HAc concentration on the charge transfer current at pH3.....	57
Table 7: Test matrix to test the effect of HAc concentration on the charge transfer current at 80°C.....	57
Table 8: Test matrix to test the effect of pH on the charge transfer current without the presence of HAc.....	57
Table 9: Test matrix to test the effect of pH on the charge transfer current in the presence of HAc.....	58
Table 10: Test matrix to test the effect of H ₂ CO ₃ concentration on the charge transfer current at pH4	60
Table 11: Test matrix to test the effect of H ₂ CO ₃ concentration on the charge transfer current at pH5	60
Table 12: Test matrix to test the effect of H ₂ CO ₃ concentration on the charge transfer current at pH6	60
Table 13: Test matrix to test the effect of H ₂ CO ₃ concentration on the charge transfer current at 80°C	61
Table 14: Test matrix to test the effect of pH on the charge transfer current without CO ₂	61
Table 15: Test matrix to test the effect of pH on the charge transfer current at 0.97 bar pCO ₂	61

Table 16: Test matrix to test the effect of pH on the charge transfer current at 9.97 bar pCO ₂	62
Table 17: Test matrix to test the effect of HCOOH concentration on the charge transfer current at pH3	88
Table 18: Chemical reactions related to CO ₂ and HAc corrosion.	98
Table 19: Exchange current density calculation	106
Table 20: Comparison between calculated and measured limiting currents at pH4.0, 25°C, 3 wt.% NaCl, RCE 1000 rpm.....	114
Table 21: Comparison between calculated and measured limiting currents at pH3.0, 25°C, 3 wt.% NaCl, RCE 1000 rpm.....	114
Table 22: Comparison between calculated and measured limiting currents at pH4.0, 80°C, 3 wt.% NaCl, RCE 1000 rpm.....	114
Table 23: Summary of the comparison between experimental and predicted corrosion rates	122

LIST OF FIGURES

Page

Figure 1: Schematic of buffering effect mechanism in CO ₂ corrosion: (a) Hydration of CO ₂ to form H ₂ CO ₃ ; (b) dissociation of H ₂ CO ₃ in the bulk to give a hydrogen ion; (c) hydrogen ion from the bulk diffuses to the metal surface; (d) adsorbed hydrogen ion gets reduced at the metal surface; (e) hydrogen atom forms from the reduction of adsorbed hydrogen ion.	32
Figure 2: Schematic of direct reduction mechanism in CO ₂ corrosion: (a) Hydration of CO ₂ to form H ₂ CO ₃ ; (b) dissociation of H ₂ CO ₃ in the bulk to give a hydrogen ion; (c) H ₂ CO ₃ (and hydrogen ion) from the bulk diffuses to the metal surface; (d) adsorbed H ₂ CO ₃ (and hydrogen ion) gets reduced at the metal surface; (e) bicarbonate ion and hydrogen atoms form at the metal surface.	33
Figure 3: Schematic of buffering effect mechanism in HAc corrosion: (a) dissociation of HAc in the bulk to give a hydrogen ion; (b) hydrogen ion from the bulk diffuses to the metal surface; (c) adsorbed hydrogen ion gets reduced at the metal surface; (d) hydrogen atom forms from the reduction of adsorbed hydrogen ion.	41
Figure 4: Schematic of direct reduction mechanism in HAc corrosion: (a) dissociation of HAc in the bulk; (b) HAc (and hydrogen ion) diffuse to the metal surface; (c) HAc (and hydrogen ion) adsorb on the metal surface; (d) adsorbed HAc (and hydrogen ion) reduced directly at the metal surface; (e) acetate ion and hydrogen atoms formed at the metal surface.	42
Figure 5: Illustration of corrosion rate change as a function of HAc concentration for direct reduction and buffering effect mechanism (at same pH).	44
Figure 6: Illustration of cathodic behavior if direct reduction of HAc were dominant, with points indicating the intersection between the anodic line and the cathodic line.	45
Figure 7: Illustration of cathodic behavior if the buffering effect mechanism were dominant, with points indicating the intersection between the anodic line and the cathodic line.	45
Figure 8: Illustration of corrosion rate change as a function of CO ₂ partial pressure for direct reduction and buffering effect mechanism.	47
Figure 9: Illustration of cathodic behavior if direct reduction of carbonic acid were dominant at the surface, with points indicating the intersection between the anodic line and the cathodic line.	47

Figure 10: Illustration of cathodic behavior if buffering effect mechanism is dominant, with points indicating the intersection between the anodic line and the cathodic line.	48
Figure 11: Similarities and differences between buffering effect and direct reduction mechanism, and expected consequences from each mechanism.	49
Figure 12: Comparison of cathodic sweeps of SS304 and X65, at 25°C, pH4.0, 1 bar pCO ₂ , 3 wt. percent NaCl, 1000 rpm.	52
Figure 13: Schematic of a 2 L glass cell. Images courtesy of Cody Shafer, ICMT.	54
Figure 14: Schematic of a 7.5 L autoclave. Images courtesy of Cody Shafer, ICMT).....	55
Figure 15: Schematic of the sample used for working electrode: a) RCE specimen used for glass cell experiment (area of 5.4 cm ²); b) RDE specimen used for glass cell experiment (area of 0.2 cm ²); c) Specimen used for autoclave experiment (area of 6.0 cm ²).	55
Figure 16: Comparison of potentiodynamic sweeps obtained using a SS304 for different HAc concentrations at 25°C, saturated N ₂ solution, pH4.0, 3wt.% NaCl, RCE rotating speed 1000 rpm.	69
Figure 17: Comparison of potentiodynamic sweeps obtained using a SS304 for different HAc concentrations at 25°C, saturated N ₂ solution, pH4.0, 3 wt.% NaCl, RDE rotating speed 1000 rpm.	70
Figure 18: Comparison of potentiodynamic sweeps obtained using a SS304 for different HAc concentrations at 25°C, saturated N ₂ solution, pH3.0, 3 wt.% NaCl, RCE rotating speed 1000 rpm.	70
Figure 19: Comparison of potentiodynamic sweeps obtained using a SS304 for different HAc concentrations at 80°C, saturated N ₂ solution, pH4.0, 3 wt.% NaCl, RCE rotating speed 1000 rpm.	71
Figure 20: Comparison of potentiodynamic sweeps obtained using a SS304 for different pH at 25°C, saturated N ₂ solution, 0 ppm HAc with 3 wt.% NaCl, RCE rotating speed 1000 rpm.	72
Figure 21: Comparison of potentiodynamic sweeps obtained using a SS304 for different pH at 25°C, saturated N ₂ solution, 100 ppm HAc with 3 wt.% NaCl, RCE rotating speed 1000 rpm.	72
Figure 22: Nyquist plot at -0.6 V vs. a saturated Ag/AgCl electrode for different undissociated HAc concentrations at 25°C, pH4.0, aqueous solution saturated with N ₂ , 3 wt.% NaCl, RDE rotating speed 1000 rpm.	74

Figure 23: Nyquist plot at -0.6 V vs. a saturated Ag/AgCl electrode obtained by using an SS304 RCE electrode for different pH at 25°C, aqueous solution saturated with N ₂ , 0 ppm HAc, 3 wt.% NaCl, RCE rotating speed 1000 rpm.	74
Figure 24: Nyquist plot at -0.6 V vs. a saturated Ag/AgCl electrode obtained by using an SS304 RCE electrode for different pH at 25°C, aqueous solution saturated with N ₂ , 100 ppm HAc, 3 wt.% NaCl, RCE rotating speed 1000 rpm.	75
Figure 25: Comparison of charge transfer current on SS304 at different pH, without CO ₂ , 25°C, 3 wt.% NaCl, RCE rotating speed 1000 rpm.....	77
Figure 26: Comparison of charge transfer current on SS304 at different pH, 1 bar pCO ₂ , 25°C, 3 wt.% NaCl, impeller stirring speed 800 rpm.	78
Figure 27: Comparison of charge transfer current on SS304 at different pH, 10 bar pCO ₂ , 25°C, 3 wt.% NaCl, impeller stirring speed 800 rpm.	78
Figure 28: Comparison of charge transfer current on SS304 at different pCO ₂ , pH4.0, 25°C, 3 wt.% NaCl, impeller stirring speed 800 rpm.	79
Figure 29: Comparison of charge transfer current on SS304 at different pCO ₂ , pH5.0, 25°C, 3 wt.% NaCl, impeller stirring speed 800 rpm.	80
Figure 30: Comparison of charge transfer current on SS304 at different pCO ₂ , pH6.0, 25°C, 3 wt.% NaCl, impeller stirring speed 800 rpm.	81
Figure 31: Comparison of charge transfer current on SS304 at different pCO ₂ , pH 6.0, 80°C, 3 wt.% NaCl, impeller stirring speed 800 rpm.	82
Figure 32: Comparison of charge transfer current on Ni200 at different pCO ₂ , pH4.0, 25°C, 3 wt.% NaCl, impeller stirring speed 800 rpm.	83
Figure 33: Comparison of charge transfer current on Ni200 vs. SS304, at different pCO ₂ , pH4.0, 25°C, 3 wt.% NaCl, impeller stirring speed 800 rpm.	84
Figure 34: Comparison of charge transfer current on X65 without and with CO ₂ at 1 bar total pressure, without inhibitor, 100 ppm H ₂ S, 25°C, pH4.0, 1 wt.% NaCl, RCE 1000 rpm. Experimental data provided by Juan Dominguez, ICMT.[76]	85
Figure 35: Comparison of charge transfer current on X65 without and with CO ₂ at 1 bar total pressure, with inhibitor, 100 ppm H ₂ S, 25°C, pH4.0, 1 wt.% NaCl, RCE 1000 rpm. Experimental data provided by Juan Dominguez, ICMT.[76]	86
Figure 36: Comparison of charge transfer current on SS304 with different formic acid concentrations, at 1 bar saturated N ₂ , 25°C, pH3.0, 3 wt.% NaCl, 1000 rpm.	89

- Figure 37: Comparison of charge transfer current on SS316L with different concentration of H₂S, at 30°C, pH6.0, 1 wt.% NaCl, RCE rotating speed 1000 rpm. Experimental data provided by Yougui Zheng, ICMT. [80] 90
- Figure 38: Effect of H₂S on polarization curves on mild steel X65, at 30°C, pH4.0, RCE rotating speed 1000 rpm, 1 wt.% NaCl. Experimental data taken from Zheng's publication. [77]..... 91
- Figure 39: Lattice structure of the Fe atoms in ferrite on the [100] plane. Figure was made by David Young, ICMT, using Crystal MakerTM. 92
- Figure 40: Lattice structure of mackinawite on the [001] plane. S atoms are in yellow. Fe atoms are in orange. Figure was made by David Young, ICMT, using Crystal MakerTM. 92
- Figure 41: Adsorption sites of H₂S on Fe [100] from side view and top view: (a) on top; (b) bridge; (c) hollow. Fe atoms are in gray. S atoms are in yellow, H atoms are in blue. Images courtesy of Cody Shafer, ICMT. Adapted from [83]. 94
- Figure 42: H₂S dissociation on Fe [100] from top view. Fe atoms are in gray. S atoms are in yellow, H atoms are in blue. Images courtesy of Cody Shafer, ICMT. Adapted from [83]. 94
- Figure 43: Crystal structure of siderite. Fe atoms are in orange. C atoms are in black, O atoms are in red. Figure was made by David Young, ICMT, using Crystal MakerTM. 94
- Figure 44: Molecular structure of (a) hydrogen sulfide (H₂S); (b) carbonic acid (H₂CO₃); (c) acetic acid (CH₃COOH); (d) formic acid (HCOOH). H atom is in white. S atom is in yellow. C atom is in black. O atom is in red. Picture sources: <http://commons.wikimedia.org/wiki> 95
- Figure 45: Comparison between experimental (solid lines) and predicted sweeps (dashed lines) at 30°C, 1 bar total pressure, saturated N₂ solution, RCE 1000 rpm, X65. FREECORP-direct reduction model was used. Experimental data provided by Yougui Zheng, ICMT. [77]..... 107
- Figure 46: Comparison between experimental (solid lines) and predicted sweeps (dashed lines) at 30°C, 1 bar total pressure, saturated N₂ solution, RCE 1000 rpm, X65. FREECORP-buffering effect model was used. Experimental data provided by Yougui Zheng, ICMT. [77]..... 107
- Figure 47: Comparison between experimental (solid lines) and predicted sweeps (dashed lines) at 25°C, 1 bar pCO₂, RCE 1000 rpm, 3 wt.% NaCl, X65. FREECORP-direct reduction model was used. 108

Figure 48: Comparison between experimental (solid lines) and predicted sweeps (dashed lines) at 25°C, 1 bar pCO ₂ , RCE 1000 rpm, 3 wt.% NaCl, X65. FREECORP-buffering effect model was used.	108
Figure 49: Comparison between experimental (solid lines) and predicted sweeps (dashed lines) at 25°C, pH4.0, 0.5 m/s, 3 wt.% NaCl, X65. FREECORP-direct reduction model was used.	109
Figure 50: Comparison between experimental (solid lines) and predicted sweeps (dashed lines) at 25°C, pH4.0, 0.5 m/s, 3 wt.% NaCl, X65. FREECORP-buffering effect model was used.	110
Figure 51: Comparison between experimental (solid lines) and predicted sweeps (dashed lines) at 25°C, pH5.0, 0.5 m/s, 3 wt.% NaCl, X65. FREECORP-direct reduction model was used.	110
Figure 52: Comparison between experimental (solid lines) and predicted sweeps (dashed lines) at 25°C, pH5.0, 0.5 m/s, 3 wt.% NaCl, X65. FREECORP-buffering effect model was used.	111
Figure 53: Comparison between experimental (solid lines) and predicted sweeps (dashed lines) at 25°C, pH6.0, 0.5 m/s, 3 wt.% NaCl, X65. FREECORP-direct reduction model was used.	111
Figure 54: Comparison between experimental (solid lines) and predicted sweeps (dashed lines) at 25°C, pH6.0, 0.5 m/s, 3 wt.% NaCl, X65. FREECORP-buffering effect model was used.	112
Figure 55: Comparison between experimental (solid lines) and predicted sweeps (dashed lines) at 25°C, pH4.0, 1 bar total pressure, saturated N ₂ solution, 3 wt.% NaCl, RCE 1000 rpm, X65. FREECORP-direct reduction model was used.	113
Figure 56: Comparison between experimental (solid lines) and predicted sweeps (dashed lines) at 25°C, pH4.0, 1 bar total pressure, saturated N ₂ solution, 3 wt.% NaCl, RCE 1000rpm, X65. FREECORP-buffering effect model was used.	113
Figure 57: Comparison between experimental and predicted corrosion rates at 30°C, 1 bar total pressure, saturated N ₂ solution, RCE 1000 rpm, 1 wt.% NaCl X65. Error bars represent standard deviation of the experimental values. Experimental data provided by Yougui Zheng, ICMT. [77].....	115
Figure 58: Comparison between experimental and predicted corrosion rates at 25°C, 1 bar pCO ₂ , RCE 1000 rpm, 3 wt.% NaCl, X65. Error bars represent standard deviation of the experimental values.	116

Figure 59: Comparison between experimental and predicted corrosion rates at 25°C, 10 bar pCO ₂ , 0.5 m/s, 3 wt.% NaCl, X65. Error bars represent standard deviation of the experimental values.	116
Figure 60: Comparison between experimental and predicted corrosion rates at 25°C, pH4.2, 10 bar pCO ₂ , 1 wt.% NaCl, X65. Experimental data taken from Nor's publication. [42].....	117
Figure 61: Comparison between experimental and predicted corrosion rates at 25°C, pH3.0, 10 bar pCO ₂ , 1 wt.% NaCl, X65. Experimental data taken from Nor's publication. [42].....	117
Figure 62: Comparison between experimental and predicted corrosion rates at 25°C, pH3.0, 80 bar pCO ₂ , 1 wt.% NaCl, X65. Experimental data taken from ICMT database.	118
Figure 63: Comparison between experimental and predicted corrosion rates at 60°C, 10 bar pCO ₂ , pH 5.0, 1 wt.% NaCl, AISI 1018. Error bars represent maximum and minimum experimental values. Experimental data taken from Wang's publication. [52].....	118
Figure 64: Comparison between experimental and predicted corrosion rates at 60°C, pH5.0, 1 m/s, 1 wt.% NaCl, AISI 1018. Error bars represent maximum and minimum experimental values. Experimental data taken from Wang's publication. [52].....	119
Figure 65: Comparison between experimental and predicted corrosion rates at 22°C, 1 bar pCO ₂ , pH4.0, 3 wt.% NaCl, 1000 rpm, X65. Error bars represent maximum and minimum experimental values. Experimental data taken from George's publication). [58]	120
Figure 66: Comparison between experimental and predicted corrosion rates at 40°C, 1 bar pCO ₂ , pH4.0, 3 wt.% NaCl, 1000 rpm, X65. Error bars represent maximum and minimum experimental values. Experimental data taken from George's publication. [58]	120
Figure 67: Comparison between experimental and predicted corrosion rates at 60°C, 1 bar pCO ₂ , pH4.0, 3 wt.% NaCl, 1000 rpm, X65. Error bars represent maximum and minimum experimental values. Experimental data taken from George's publication). [58]	121
Figure 68: Comparison between experimental and predicted corrosion rates at 25°C, 1 bar total pressure, saturated N ₂ solution, pH4.0, 3 wt.% NaCl, 1000 rpm, X65. Error bars represent standard deviation of the experimental values.	121
Figure 69: Comparison between glass cell vs. SS autoclave experiment. Inconsistent charge transfer currents at 1 bar pCO ₂ experiment, pH4.0, 25°C, 3 wt% NaCl in the SS autoclave using a stationary electrode, impeller stirring speed 100rpm.	141

Figure 70: Comparison between using a RCE vs. without rotation. Inconsistent charge transfer currents at 1 bar CO ₂ experiment, pH4.0, 25°C, 3 wt% NaCl in the glass cell, without rotation, using magnetic stirring bar.....	141
Figure 71: Experiments conducted in the glass cell, without rotation: (a) Schematic of glass cell; (b) Bubble formation on sample at low stirring speed; (c) No bubbles on the sample at high stirring speed.....	142
Figure 72: Schematic of the acrylic autoclave.....	143
Figure 73: Comparison between glass cell vs. acrylic autoclave experiments. Consistent charge transfer currents at 1 bar CO ₂ experiment, pH4.0, 25°C, 3 wt% NaCl, in the acrylic autoclave using a stationary electrode, impeller stirring speed 800rpm.....	144
Figure 74: Comparison between glass cell vs. SS autoclave experiments. Consistent charge transfer currents at 1 bar CO ₂ experiment, pH4.0, 25°C, 3 wt% NaCl, in the SS autoclave using a stationary electrode, impeller stirring speed 800rpm.....	144
Figure 75: Comparison between glass cell vs. SS autoclave experiments. Consistent charge transfer currents at 1 bar CO ₂ experiment, pH5.0, 25°C, 3 wt% NaCl, in the SS autoclave using a stationary electrode, impeller stirring speed 800rpm.....	145
Figure 76: Reproducible charge transfer currents at 10 bar CO ₂ experiment, pH5.0, 25°C, 3 wt% NaCl in the SS autoclave using a stationary electrode, impeller stirring speed 800rpm.....	145
Figure 77: Repeated potentiodynamic sweeps using a SS304 for different pH at 25°C, saturated N ₂ solution, 3 wt.% NaCl, RCE rotating speed 1000 rpm.....	146
Figure 78: Repeated potentiodynamic sweeps using a SS304 for different HAc concentrations at 25°C, saturated N ₂ solution, pH4.0, 3 wt.% NaCl, RCE rotating speed 1000 rpm.....	147
Figure 79: Repeated potentiodynamic sweeps using a SS304 for different pH at 25°C, saturated N ₂ solution, 100ppm HAc, 3 wt.% NaCl, RCE rotating speed 1000 rpm.....	147
Figure 80: Repeated potentiodynamic sweeps using a SS304 for different HAc concentration at 80°C, saturated N ₂ solution, pH4.0, 3 wt.% NaCl, RCE rotating speed 1000 rpm.....	148
Figure 81: Repeated potentiodynamic sweeps using a SS304 at different pCO ₂ , pH4.0, 25°C, 3 wt.% NaCl, impeller stirring speed 800 rpm.....	148
Figure 82: Repeated potentiodynamic sweeps using a SS304 at different pCO ₂ , pH5.0, 25°C, 3 wt.% NaCl, impeller stirring speed 800 rpm.....	149

Figure 83: Repeated potentiodynamic sweeps using a SS304 at different pCO ₂ , pH6.0, 80°C, 3 wt.% NaCl, impeller stirring speed 800 rpm.	149
Figure 84: Repeated potentiodynamic sweeps using a SS304 at different pCO ₂ , pH6.0, 25°C, 3 wt.% NaCl, impeller stirring speed 800 rpm.	150
Figure 85: Repeated potentiodynamic sweeps using a Ni200 at different pCO ₂ , pH4.0, 25°C, 3 wt.% NaCl, impeller stirring speed 800 rpm.	150
Figure 86: Repeated potentiodynamic sweeps using a X65 at 1 bar pCO ₂ , pH4.0, 25°C, RCE rotating speed 1000 rpm, 3 wt.% NaCl.	151
Figure 87: Repeated potentiodynamic sweeps using a X65 at 1 bar pCO ₂ , pH5.0, 25°C, RCE rotating speed 1000 rpm, 3 wt.% NaCl.	151
Figure 88: Repeated potentiodynamic sweeps using a X65 at 1 bar pCO ₂ , pH6.0, 25°C, RCE rotating speed 1000 rpm, 3 wt.% NaCl.	152
Figure 89: Repeated potentiodynamic sweeps using a X65 at 10 bar pCO ₂ , pH4.0, 25°C, 3 wt.% NaCl, impeller stirring speed 800 rpm.	152
Figure 90: Repeated potentiodynamic sweeps using a X65 at 10 bar pCO ₂ , pH5.0, 25°C, 3 wt.% NaCl, impeller stirring speed 800 rpm.	153
Figure 91: Repeated potentiodynamic sweeps using a X65 at 10 bar pCO ₂ , pH6.0, 25°C, 3 wt.% NaCl, impeller stirring speed 800 rpm.	153

CHAPTER 1: INTRODUCTION

Corrosion of mild steel has been a challenge for the oil and gas industries for decades, negatively affecting profit, human health and safety, and the natural environment [1]. Mild steel has been widely used in oil and gas production due to its low cost and broadly applicable mechanical properties [1]. Compared to corrosion resistant alloys (CRAs), mild steel is more cost effective when used in the construction of thousands of miles of pipeline. Although corrosion inhibitors are regularly applied, their effectiveness is often limited due to many factors, both technical and human. For example, non-compliance with so-called inhibitor availability targets is a main issue, leaving oil and gas pipelines exposed to corrosion. Depending on the concentrations of corrosive species, corrosion of mild steel can become a major problem.

In addition to hydrogen sulfide (H_2S) corrosion (sour corrosion), carbon dioxide (CO_2) corrosion (sweet corrosion) is common in the oil and gas industry [1-3]. CO_2 is generally present in the raw natural gas and crude oil obtained from hydrocarbon reservoirs. Other weak organic acids, which can be found in many upstream oil and gas production lines, are also corrosive species and are severely detrimental to mild steel [4-7]. The corrosive effects of weak organic acids on mild steel have been confirmed for so-called bottom-of-the-line corrosion, as well as in top-of-the-line corrosion arising from water condensation [7]. The effect of these weak acids can be significant at all stages of production and can affect the entire infrastructure, from downhole tubing to surface equipment.

Failures related to CO₂ corrosion and organic acid corrosion have been widely reported, and cause considerable economic loss [1,6]. Aqueous concentrations of organic acids in the field are typically 100 ppm, though in some cases concentrations as high as 3000 ppm have been reported [7]. Among organic acids, acetic acid (CH₃COOH, or HAc) is known as the dominant low-molecular-weight organic acid found in produced fluids (usually 50-90 percent of the organic acids) [8]. As a result, extensive research has been dedicated to understanding the corrosion mechanism in CO₂ environments with acetic acid present. The corrosion mechanism is complex, and is influenced by a number of factors (e.g. temperature, pH, CO₂ partial pressure, HAc concentration, etc.), however, significant progress has been made in its understanding [1,9]. Corrosion prediction models have been developed by numerous researchers, and also by several oil and gas companies, as tools to predict corrosion failures. Chemical and electrochemical reactions in CO₂ corrosion and in HAc corrosion have been investigated, and basic corrosion mechanisms have been established [10,11].

Some studies have suggested that hydrogen ions are the main cathodic species in acid solutions and are reduced at the steel surface, resulting in iron dissolution (corrosion of iron) [12-15]. There is disagreement on whether direct reduction of carbonic and acetic acids at the steel surface also contribute to the corrosion process [10,16-19].

When CO₂ is present in the solution, carbonic acid (H₂CO₃) forms as a weak acid and provide hydrogen ions via partial dissociation. This is commonly referred to as the *buffering effect*, in which carbonic acid (in this case) becomes a reservoir of hydrogen ions. Extensive research shows that the corrosion rate of carbon steel in the presence of

CO₂ is higher than in a strong acid solution at the same pH. It is difficult to explain this behavior with only one electrochemical reaction (hydrogen ion reduction), especially at high pH, where it appears that the contribution of hydrogen ions is negligible. An alternative mechanism, known as *direct reduction*, has been suggested in several studies, and is frequently assumed to be an additional reaction alongside the buffering effect. It is important to note that the buffering effect and the direct reduction mechanisms are equal in terms of thermodynamics—the initial and final states are the same, only the pathway is different, leading to a difference in kinetics. This difference is critical for corrosion prediction modeling, particularly in extreme conditions, such as high temperature or high pressure. It remains unclear, however, whether the direct reduction of carbonic acid contributes significantly to the corrosion process. Similar mechanisms have been proposed for HAc, which is also a weak acid. The direct reduction of HAc is commonly assumed to predict corrosion rates, though there is uncertainty whether the use of direct reduction of HAc at the steel surface is actually appropriate in corrosion prediction [20].

Numerous mechanistic and empirical models have been developed based on the assumption of direct reduction of carbonic acid and HAc without a reasonable verification of the dominance of such reactions [10,11,16,20]. Few models have suggested that the buffering effect is sufficient to explain the CO₂ corrosion mechanism or the HAc corrosion mechanism, and evidence suggesting that the direct reduction of carbonic acid or HAc is negligible is not convincing [17,18].

Corrosion models currently used in the Institute for Corrosion and Multiphase Technology at Ohio University (ICMT) are based on the direct reduction of carbonic acid

and HAc. To conduct more accurate modeling, it would be beneficial to validate these assumptions, or to modify them based on actual physical phenomena.

Present research focuses on mild steel corrosion mechanisms in an aqueous carbonic acid or HAc solution. The work includes a study of mild steel corrosion mechanisms in the presence of HAc, and then relates it to the CO₂ corrosion mechanism. The reason to study the HAc mechanism first is that higher concentrations of HAc can be achieved in glass cell experiments at atmospheric pressure. The experiments are done at higher pressure to study the role of carbonic acid on the cathodic reaction and, therefore, determine the mild steel corrosion mechanism in an aqueous CO₂ solution.

Furthermore, in a parallel study, the same methodology was applied to study the effect of another common weak acid present in the field – hydrogen sulfide (H₂S) – on the cathodic reaction. The question of whether or not the direct reduction of H₂S at the steel surface is significant also needs to be answered. The corrosion mechanism of mild steel in the presence of H₂S, HAc and carbonic acid could then be compared. A hypothesis based on the molecular structure of weak acids is proposed to explain the ability of H₂S to have direct reaction with the iron surface. Mechanisms of reduction for other weak acids, such as formic acid (HCOOH), and water (H₂O) will also be discussed.

This dissertation is structured as follows: Chapter 2 is a review of key research on the corrosion of mild steel in CO₂ aqueous solution, and in the presence of HAc. It includes a detailed description of the two mechanisms: the buffering effect, and direct reduction. Chapter 3 defines research objectives and hypotheses. Chapter 4 provides the methodology and experimental description, and is followed by a discussion of the results

for HAc and carbonic acid in Chapters 5, along with a discussion on the use of the substrate and the inhibitor. In the same chapter, the corrosion mechanisms of mild steel in other weak acids such as HCOOH, H₂O, and H₂S are also discussed. In Chapter 6, an electrochemical model is developed based on a proposed mechanism. Finally, Chapter 7 presents a summary of important points of this research, and a way forward.

Parts of this work have been published in the internal confidential reports of the Ohio University Corrosion Center Joint Industry (CC-JIP) Advisory Board meetings over the period 2010 – 2014 [21-28]. Excerpts from the work were published at NACE (National Association of Corrosion Engineers) International conferences and in the Corrosion Journal [29,30].

CHAPTER 2: LITERATURE REVIEW

2.1 Basics of CO₂ corrosion process

Sweet corrosion (or CO₂ corrosion) is recognized as a major problem in pipeline corrosion [1-3]. It is important to point out that CO₂ gas itself is not a corrosive species. In the presence of water, however, CO₂ forms carbonic acid, which is corrosive. The corrosion process is described below.

The CO₂ gas dissolves in water. A very small fraction of dissolved CO₂ hydrates to carbonic acid. As a weak acid, carbonic acid partially dissociates into hydrogen ions and bicarbonate ions, which is followed by the dissociation of bicarbonate ions that form additional hydrogen ions and carbonate ions. Hydrogen ions are reduced to hydrogen gas. In addition to the reduction of hydrogen ions, it is often assumed that carbonic acid is directly reduced at the metal surface [10,16]. In some conditions, such as at high pH or high partial pressure of CO₂, the reduction of bicarbonate ions might also be considered [31]. Iron, giving up electrons to balance the charge, dissolves to produce ferrous ions, resulting in metal corrosion. These reactions are listed in Table 1. In certain conditions, a solid iron carbonate layer can form at high pH and high temperature when the solution is supersaturated in ferrous iron. The properties and behavior of this layer is beyond the scope of this research.

Table 1: Chemical and electrochemical reactions involved in the CO₂ corrosion process.

Process	Reactions	
Dissolution of CO ₂	$CO_{2(g)} \rightleftharpoons CO_{2(aq)}$	(1)
Hydration of CO ₂	$CO_{2(aq)} + H_2O_{(l)} \rightleftharpoons H_2CO_{3(aq)}$	(2)
Dissociation of carbonic acid	$H_2CO_{3(aq)} \rightleftharpoons H^+_{(aq)} + HCO_3^-_{(aq)}$	(3)
Dissociation of bicarbonate	$HCO_3^-_{(aq)} \rightleftharpoons H^+_{(aq)} + CO_3^{2-}_{(aq)}$	(4)
Reduction of hydrogen ion	$2H^+_{(aq)} + 2e^- \rightarrow H_{2(g)}$	(5)
Reduction of carbonic acid	$2H_2CO_{3(aq)} + 2e^- \rightarrow H_{2(g)} + 2HCO_3^-_{(aq)}$	(6)
Reduction of bicarbonate	$2HCO_3^-_{(aq)} + 2e^- \rightarrow H_{2(g)} + 2CO_3^{2-}_{(aq)}$	(7)
Dissolution of iron	$Fe \rightarrow Fe^{2+}_{(aq)} + 2e^-$	(8)

Two mechanisms coexist in the literature that explain the role of carbonic acid in corrosion of mild steel in a CO₂ aqueous environment. If only hydrogen ions are reduced at the metal surface (reaction 5), the mechanism is called the buffering effect. The term “buffer” in this case means carbonic acid acts as a reservoir of hydrogen ions. When hydrogen ions are consumed by the corrosion process, carbonic acid provides additional hydrogen ions via dissociation (reaction 3). If the direct reduction of carbonic acid is taken into account (reaction 6) along with the hydrogen evolution reaction, the mechanism is referred to as direct reduction. Although a large number of publications assumes the direct reduction of carbonic acid in order to explain a higher corrosion rate of steel in the presence of CO₂ compared to a strong acid solution at the same pH, it

remains unclear whether the direct reduction of carbonic acid (reaction 6) is significant compared to the reduction of hydrogen ions (reaction 5) [10,11,16].

While there are several possible cathodic reactions depending on the environment, the only dominant anodic reaction is iron dissolution (reaction 8). This reaction was extensively studied by a large number of researchers for a wide range of pH conditions [32-40]. Although hydrogen ions do not appear in the iron dissolution reaction (reaction 8), their effect has been demonstrated in several mechanistic studies [35-37]. Bockris proposed several multi-step mechanisms for iron dissolution in strong acids [35]. The most widely accepted is the BDD mechanism:



This mechanism predicts a dependence of the iron dissolution rate on OH^- , and is often assumed to apply in CO_2 corrosion [9]. De Waard and Milliams adopted the BDD mechanism in their work for aqueous CO_2 corrosion [16]. Davies and Burstein introduced the effect of bicarbonate ions on the iron dissolution in bicarbonate solutions with the formation of complex anions of the type $Fe(CO_3)_2^{2-}$ [40].

More recently, Nescic, et al. conducted galvanostatic measurements and potentiodynamic sweeps on mild steel in the presence of CO_2 , and proposed different anodic mechanisms with pH as main parameter [32]. At $pH < 5$, the anodic dissolution rate depends on both OH^- concentration and partial pressure of CO_2 . At $pH > 5$, the dependence of the anodic reaction on pH vanishes. This observation agrees with Videm's

work [39]. Nesic, et al. also suggested that iron dissolution was catalyzed by a carbonic species as a chemical ligand and the influence of partial pressure of CO₂ did not change with pH.

2.2 Key parameters affecting CO₂ corrosion mechanism

2.2.1 Effect of pH

As the cathodic reaction occurring at the metal surface, the hydrogen evolution reaction has been widely studied by researchers since the 1950s indicating that pH plays a key role in the corrosion process [12-15]. Data from numerous experiments demonstrates that a pH decrease (which means an increase of hydrogen ion concentration) promotes the cathodic reaction (reaction 5), which accelerates the corrosion process. On the other hand, an increase of pH helps to slow down the corrosion rate. Indeed, at high pH and high temperature, iron carbonate might form when the solution is supersaturated, which gives a degree of protection to the steel surface. The pH not only affects the cathodic reaction, which involves the reduction of hydrogen ions, but also influences the anodic dissolution, as discussed above [35,37,38].

2.2.2 Effect of flow

Transportation of species to and from the metal surface is another important aspect of the corrosion process. High flow brings more cathodic species to the metal surface, where they are consumed by the corrosion reaction. Consequently, high flow increases corrosion rates. Up to a certain point, when the corrosion process changes from

being mass transfer controlled to being charge transfer controlled, increasing the flow has no effect on corrosion rates. In the case of film forming conditions, flow can interfere with the precipitation or dissolution of the protective corrosion product layer and consequently affects the corrosion process.

Extensive time was dedicated to study the effect of flow in sweet corrosion [2,41-43]. Nesic et al. compared the effect of two different flow geometries on the corrosion rates by using a rotating cylinder and pipe flow [41]. The authors observed that the flow dependence corrosion rates at pH values of 4 and 5 could be explained by the mass transfer of hydrogen ions. At pH6, however, due to the slow hydration reaction of CO_2 , the limiting current has a diffusion-controlled component and a chemical reaction-controlled component, which corroborated findings by Schmitt and Rothman [44].

In 1995, Pots proposed two mechanistic models to predict CO_2 corrosion rates under multiphase flow conditions [11]. The first one is the limiting corrosion rate (LCR) model, which was based on the assumption that corrosion rate was controlled by the transport and production of cathodic species (such as hydrogen ions and carbonic acid). The LCR model is only able to provide an upper limit of corrosion rate because at higher flow, charge transfer should be the rate determining step, not mass transfer. In order to improve the corrosion rate prediction, especially at high flow velocities, an advanced numerical model was proposed. The advantage of a numerical model is that coupled mass transport equations can be solved to calculate concentration profiles near the metal surface. Charge transfer control was implemented for better corrosion rate prediction at high flow velocities.

More recently, Nor et al. investigated the effect of flow in a high pressure, high temperature, flow loop system [42]. The authors explained that a slight sensitivity of corrosion rates with flow, even at low pH, might be due to the dominance of the slow chemical reaction of aqueous CO₂ hydration, rather than the mass transport of hydrogen ions and carbonic acid. They also reported that the anodic reaction was unaffected by flow since it was under charge transfer control.

2.2.3 Effect of temperature

Temperature greatly affects the corrosion process. In general, increasing temperature accelerates transport and chemical/ electrochemical reactions. Therefore, corrosion rates will progressively increase with temperature. This was observed in many experimental results [45,46]. Fang studied CO₂ corrosion at low temperature, and concluded that the corrosion process changes from mixed charge transfer/ limiting current control to a pure charge transfer control mechanism [47].

In some circumstances, increased temperature also speeds up the kinetics of precipitation of film formation, which reduces corrosion rates. The effect of temperature on the corrosion product has been well investigated [48-50].

2.2.4 Effect of partial pressure of CO₂

Corrosion rates of mild steel at high partial pressure of CO₂ have been widely reported [42,51,52]. Using a rotating cylinder electrode autoclave and a pipe flow loop system, Nor et al., measured corrosion rates up to 30 mm/y at 10 bar CO₂ and 50°C [42].

Their results also suggested that increasing partial pressure of CO_2 reduced the flow-sensitivity of the CO_2 corrosion rate due to the slow CO_2 hydration reaction step. In another study, Wang reported that partial pressure of CO_2 did not affect the anodic reaction, but affected the limiting current [52]. The increase of the limiting currents with partial pressure of CO_2 has been well explained in other work [44].

In general, the effect of increasing partial pressure of CO_2 was known to enhance the cathodic reaction, resulting in an increase of corrosion rates. In fact, increasing partial pressure of CO_2 results in a higher concentration of carbonic acid in the solution. This is where the issue of distinguishing between the buffering effect and direct reduction mechanisms arises. In either case, the dissociation of carbonic acid that forms hydrogen ions is followed by their reduction at the metal surface. Therefore, increasing partial pressure of CO_2 promotes the reduction of hydrogen ions because carbonic acid acts as a reservoir of hydrogen ions via dissociation. Moreover, if the direct reduction of carbonic acid is taken into account in addition to the reduction of hydrogen ions, cathodic reactions are thus accelerated due to this additional electrochemical reaction. As a result, increasing CO_2 partial pressure usually increases the corrosion rate. In certain other conditions, increased partial pressure of CO_2 might reduce corrosion rate when formation of iron carbonate is favored. A detailed analysis of the effect of partial pressure of CO_2 , along with the description of the two proposed mechanisms (direct reduction and buffering effect) is presented below.

2.3 Direct reduction vs. buffering effect mechanism in CO₂ corrosion

Two mechanisms coexist to explain a high corrosion rate of mild steel in the presence of CO₂. In the buffering effect mechanism, carbonic acid, formed from the hydration of CO₂, partially dissociates to provide H_{bulk}^+ and HCO_3^- (reaction 12). Hydrogen ions from the bulk (H_{bulk}^+) are then adsorbed onto the surface (reaction 13) and are subsequently reduced (reaction 14). The schematic of this mechanism is shown in Figure 1.

The role of carbonic acid in this case is to provide additional hydrogen ions when they are consumed at the metal surface.



In the direct reduction mechanism, reactions 12-14 are still valid. Carbonic acid is also adsorbed onto the metal surface (reaction 15), and is then directly reduced (reaction 16). The schematic of this mechanism is shown in Figure 2.



Although the direct reduction and buffering effect mechanisms are identical from a thermodynamic point of view, the distinction of the pathway is essential for modeling. To better predict corrosion rates, particularly at extreme conditions, such as high pressure, high pH, and high temperature, one must understand the mechanism behind the observed processes. Numerous models have been developed based on different

assumptions, i.e., whether direct reduction of carbonic acid at the metal surface is taken into account [11,16,20,53]. None, however, can prove the direct reduction of carbonic acid.

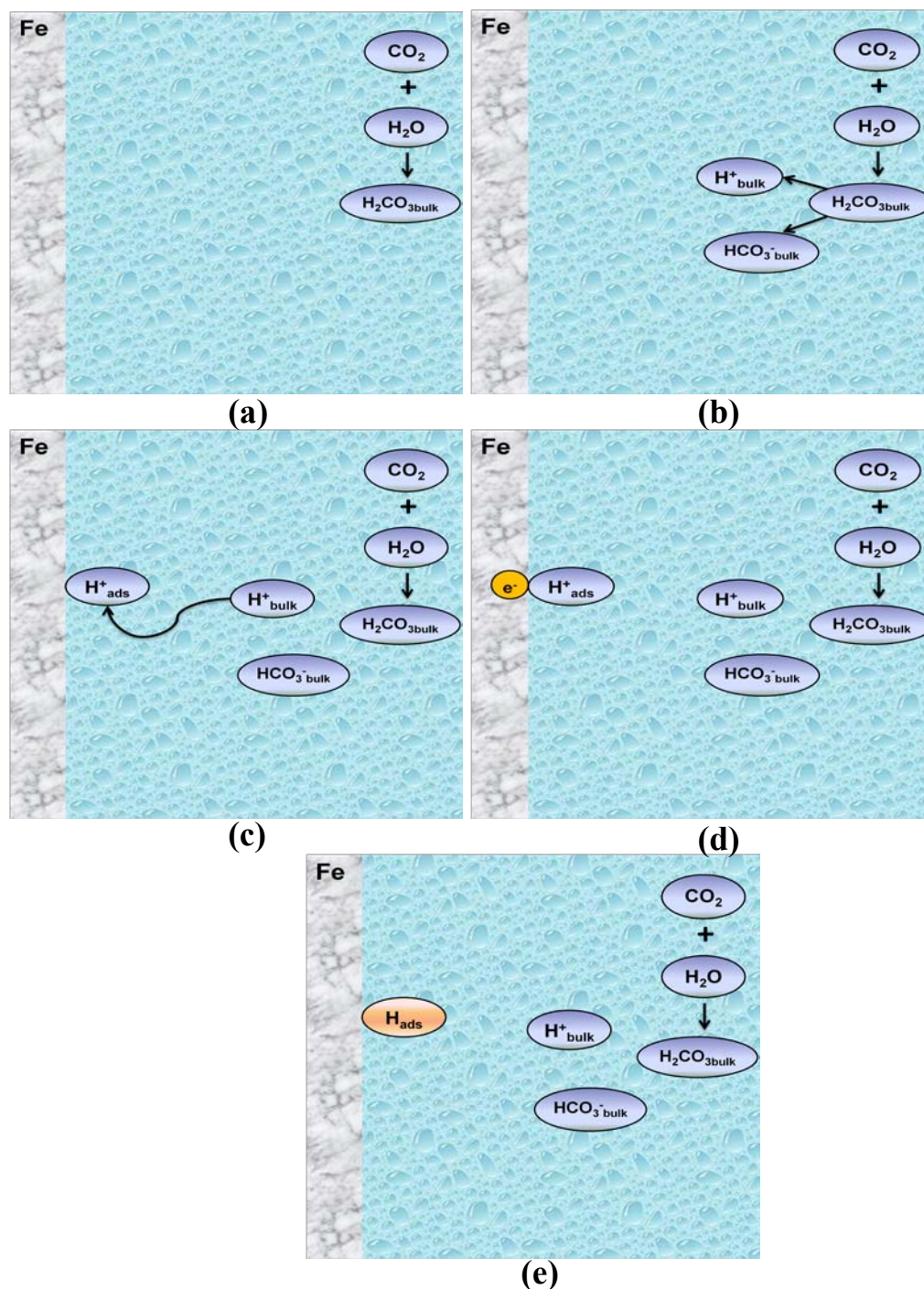


Figure 1: Schematic of buffering effect mechanism in CO₂ corrosion: (a) Hydration of CO₂ to form H₂CO₃; (b) dissociation of H₂CO₃ in the bulk to give a hydrogen ion; (c) hydrogen ion from the bulk diffuses to the metal surface; (d) adsorbed hydrogen ion gets reduced at the metal surface; (e) hydrogen atom forms from the reduction of adsorbed hydrogen ion.

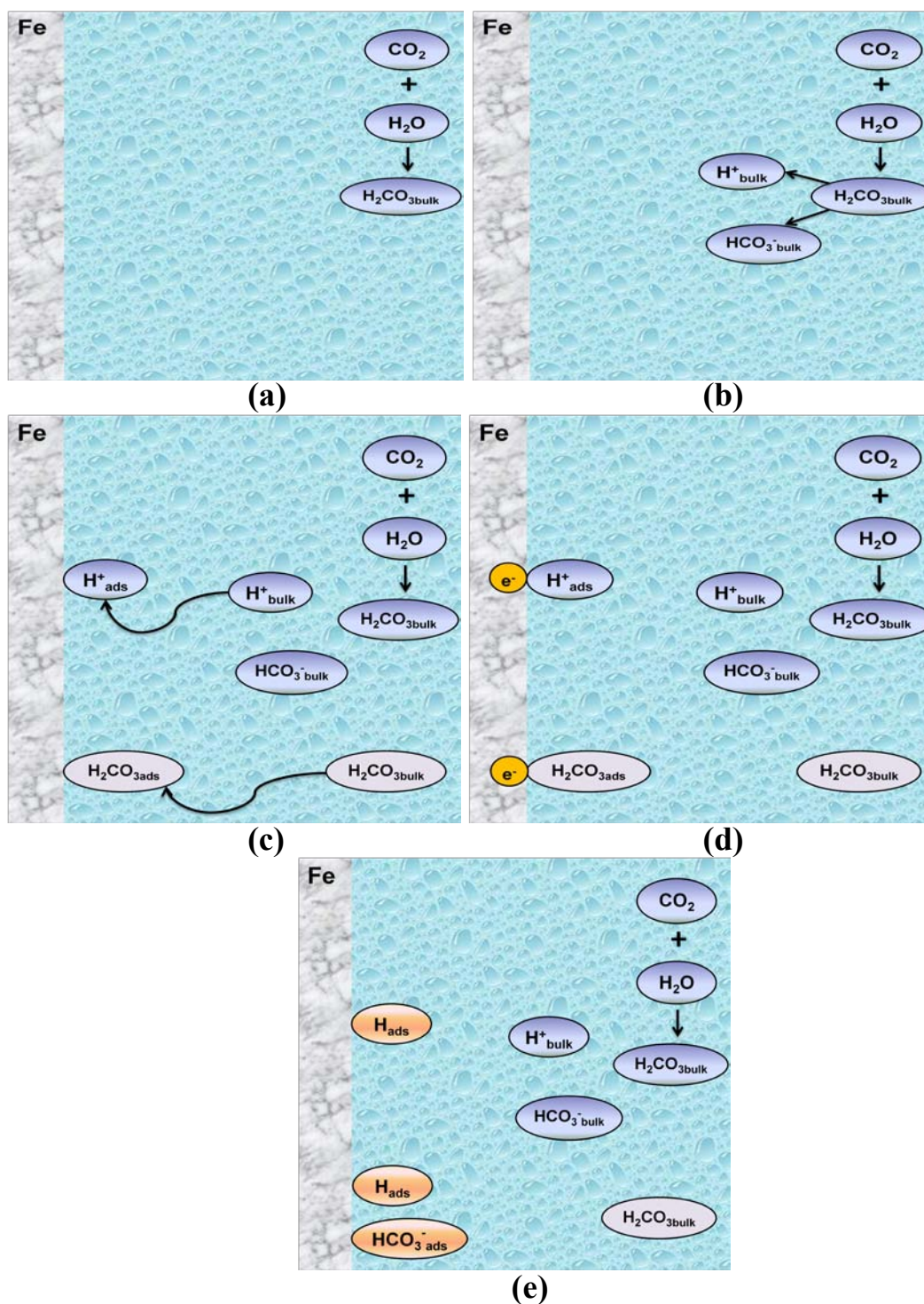


Figure 2: Schematic of direct reduction mechanism in CO_2 corrosion: (a) Hydration of CO_2 to form H_2CO_3 ; (b) dissociation of H_2CO_3 in the bulk to give a hydrogen ion; (c) H_2CO_3 (and hydrogen ion) from the bulk diffuses to the metal surface; (d) adsorbed H_2CO_3 (and hydrogen ion) gets reduced at the metal surface; (e) bicarbonate ion and hydrogen atoms form at the metal surface.

The first CO₂ corrosion model was proposed by de Waard and Milliams in 1975 [16]. The authors related the corrosion rate of carbon steel and CO₂ partial pressure. A higher corrosion rate was observed in the CO₂ saturated solution compared to a completely dissociated acid at the same concentration. Quantitatively, the authors found that the corrosion rate increases proportionally to the partial pressure of CO₂ raised to the power of 0.67. This result was attributed to the direct reduction of carbonic acid at the metal surface. However, only the effect of temperature and partial pressure of CO₂ was included in this model, and the maximum tested pressure was no higher than atmospheric. Further, the de Waard and Milliams model assumed that the corrosion reaction is charge transfer controlled. Mass transport was also neglected. In subsequent papers correcting factors were added to account for the effects of pH, flow, scaling, and inhibition [54]. Although it is only a semi-empirical model lacking accuracy and physical meaning, the de Waard and Milliams model is widely used in corrosion prediction.

Though mass transport was ignored by de Waard and Milliams, it was the focus of Schmitt and Rothmann's study two years later [44]. By conducting cathodic polarization on platinum and steel in a CO₂ saturated solution, the authors pointed out that the cathodic limiting current was comprised of two components: a diffusion controlled component, and a chemical reaction controlled component. The former occurs due to the diffusion of hydrogen ions and undissociated carbonic acid, the latter occurs due to the slow hydration of CO₂ to form carbonic acid, and its rapid dissociation. The authors attributed an increase of current to the direct reduction of adsorbed, undissociated carbonic acid at the metal surface. Although their study agreed with de Waard and

Milliams on the existence of the direct reduction of carbonic acid, Schmitt and Rothmann suggested that the hydration reaction of adsorbed CO_2 determines rate, and explains the reactions leading to the limiting current.

In a 1989 paper, Gray and Anderson proposed a similar mechanism [2,55]. They disagreed with Schmitt and Rothmann about the surface adsorption of CO_2 prior to the hydration reaction. Since similar limiting currents were observed on platinum and iron, the authors proposed instead a homogenous hydration of CO_2 , which has been widely accepted since then.

Most of the alternative mechanisms proposed by later researchers assume the direct reduction of carbonic acid at the metal surface, but the nature of the direct reduction has hardly been discussed. Netic was one of the few researchers suggesting that carbonic acid reduction must be accounted for in the corrosion process [10]. However, most of his experiments were conducted in a glass cell at atmospheric pressure, where the effects of carbonic acid could be far less than those of hydrogen ions. Netic et al. developed a mechanistic model which included direct reduction of carbonic acid for a range of parameters to predict uniform CO_2 corrosion [53]. A similar assumption of the direct reduction of carbonic acid was included in the mechanistic models proposed by Pots in order to predict CO_2 corrosion rates under multiphase flow conditions [11].

On the other hand, some researchers claimed that hydrogen ion reduction was sufficient to explain the high corrosion rate in the presence of CO_2 . Linter and Burstein agreed with Hurlen, who described the effect of dissolved CO_2 as a buffer source for the reduction of hydrogen ions [56,57]. Linter and Burstein concluded that the reduction of

carbonic acid was not a contributing factor because it was thermodynamically unfavorable in comparison to the reduction of hydrogen ions.

In another study, Remita et al. conducted glass cell experiments using a rotating disk electrode [17]. The authors showed that the effect of carbonic acid was to create additional hydrogen ions, which corresponded to the buffering effect mechanism. They argue that the direct reduction of carbonic acid would lead to an increase of the surface pH in the presence of CO₂ compared to a saturated N₂ solution, which was not observed in their measurements. The authors therefore concluded that the buffering effect of carbonic acid was sufficient to explain the CO₂ corrosion mechanism. Again, however, their experiments were limited to atmospheric pressure.

2.4 Direct reduction vs. buffering effect in acetic acid corrosion

In the past few decades, a number of studies have been dedicated to investigating the effect of HAc on mild steel corrosion in aqueous environments [58-63]. Dougherty and Gulbrandsen conducted a thorough review of studies investigating the effect of HAc on CO₂ corrosion [64,65]. Some studies reported the detrimental effects of HAc, while others claimed HAc served as a corrosion inhibitor [66,67].

Similar to the carbonic acid found in CO₂ saturated aqueous solutions, HAc is a weak acid, which partially dissociates (see reaction 17) to an extent which is governed by pH and the solution temperature.



Where K_a is the equilibrium constant, defined as:

$$K_a = \frac{[H^+][Ac^-]}{[HAc]} \quad (18)$$

According to most mechanistic studies, HAc enhances the corrosion rate of mild steel by accelerating the rate of the cathodic hydrogen evolution reaction. However, the exact mechanism remains controversial. In the buffering effect, HAc dissociates and provides an additional source of free hydrogen ions near the steel surface, and the dominant cathodic reaction remains a reduction of hydrogen ions. The alternative possibility is that the adsorbed undissociated HAc molecule is reduced at the surface (in addition to any reduction of free hydrogen ions); this is the direct reduction mechanism. These mechanisms are identical thermodynamically—the beginning and end of each process is the same. The difference is in the pathway, and consequently, the kinetics. In both mechanisms, the anodic reaction that occurs simultaneously at the metal surface in order to balance the charge is the oxidative dissolution of iron:



These two mechanisms are reviewed in detail below.

In the buffering effect, the role of HAc is to act as a buffer, providing more hydrogen ions as they are consumed by the corrosion reaction at the surface. This mechanism is illustrated in Figure 3. HAc produces hydrogen ions and acetate ions through dissociation (reaction 19); hydrogen ions diffuse from the bulk to adsorb at metal surface (reaction 13), where they are reduced to form a hydrogen atom (reaction 14), just like what happens with strong acids.



Hurlen et al. investigated the effect of acetate buffer on the cathodic reaction of an iron electrode [68]. The authors reported that the effect of HAc concentration on the charge transfer current is negligible; its effect only appears in the limiting current at more negative potentials. This can be interpreted as an indication that the buffering effect mechanism is dominant.

By conducting a series of potentiodynamic sweeps on a rotating cylinder electrode at pH4, George, Nescic, and de Waard suggested the validity of the buffering effect mechanism [58]. According to George, only the cathodic limiting current is significantly accelerated in the presence of HAc, while the anodic reaction is slightly retarded [18,58]. He argued that if HAc was directly reduced at the surface, the corrosion current density would increase proportionally with increasing HAc concentrations, which was not observed in the experimental data. Therefore, the author suggested that HAc provides hydrogen ions as needed to feed the cathodic reaction. In a subsequent paper the same authors made arguments in favor of a different mechanism—direct reduction of HAc [59].

In the direct reduction of HAc, the reactions 13, 14, and 19 underlying the buffering effect mechanism are assumed to remain valid. According to this mechanism, HAc is also adsorbed onto the metal surface (reaction 20) and reduced directly, according to reaction 21. The schematic of the direct reduction mechanism is shown in Figure 4.



This mechanism was favored by many authors, and was used to explain a high corrosion rate of mild steel in the presence of HAc. Garsany et al. studied the role of the acetate ion on the corrosion rate of carbon steel in a CO₂ environment using a rotating disk electrode [19]. Their voltammograms showed two “waves”, apparently resulting from the reduction of free hydrogen ions and direct reduction of HAc. However, the authors also pointed out that due to the rapid dissociation of HAc, it is very difficult to experimentally distinguish between the direct reduction of HAc and that of hydrogen ions. Matos et al., used square wave voltammetry, and observed two different peaks on a platinum microdisk working electrode, suggesting the reduction of both free hydrogen ions and HAc [69].

In Zhang’s studies of thermodynamic calculations of a system of CO₂ containing oilfield formation water in the presence of HAc, the author concluded that HAc direct reduction dominates the cathodic process due to its lower negative-equilibrium potential of the reduction of HAc [70].

Singer et al. studied the combined effect of H₂S partial pressure and free HAc concentration on CO₂ corrosion at the bottom-of-the-line [71]. The authors observed an increase in corrosion rate in the presence of HAc, and attributed this behavior to the direct reduction of HAc. A similar conclusion has been made by the same author in a study of top-of-the-line corrosion in the presence of HAc and CO₂ [72].

The brief review of critical literature shows that the answer to the question whether direct reduction of HAc is significant remains unclear. The objective of this project was to provide additional evidence to help determine whether the direct reduction of HAc is important. Furthermore, a study leading to improved understanding of HAc corrosion mechanisms provided a starting point for similar analytical studies of CO₂ corrosion mechanisms where experimentation is more difficult.

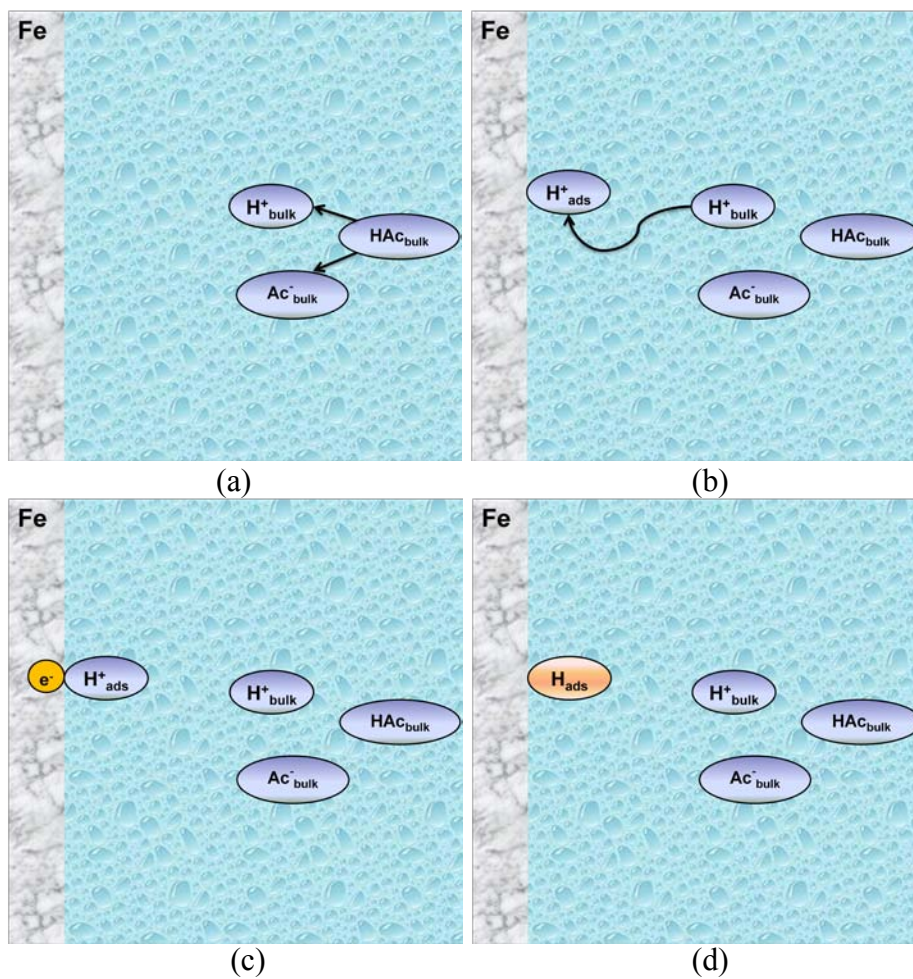


Figure 3: Schematic of buffering effect mechanism in HAc corrosion: (a) dissociation of HAc in the bulk to give a hydrogen ion; (b) hydrogen ion from the bulk diffuses to the metal surface; (c) adsorbed hydrogen ion gets reduced at the metal surface; (d) hydrogen atom forms from the reduction of adsorbed hydrogen ion.

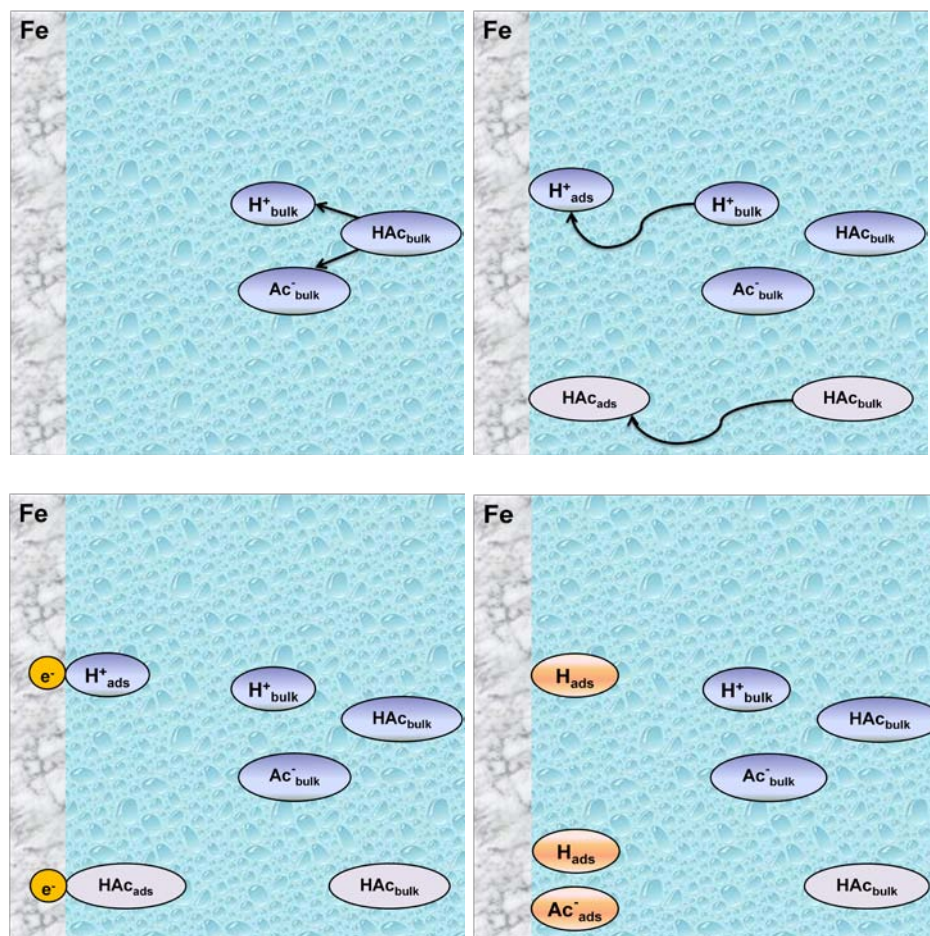


Figure 4: Schematic of direct reduction mechanism in HAC corrosion: (a) dissociation of HAC in the bulk; (b) HAC (and hydrogen ion) diffuse to the metal surface; (c) HAC (and hydrogen ion) adsorb on the metal surface; (d) adsorbed HAC (and hydrogen ion) reduced directly at the metal surface; (e) acetate ion and hydrogen atoms formed at the metal surface.

CHAPTER 3: RESEARCH OBJECTIVES AND HYPOTHESES

3.1 Research objectives

The literature review outlines the need to clarify the corrosion mechanisms of mild steel in the presence of aqueous CO₂ and HAc. The experimental work is divided into two parts. In the first part, corrosion mechanisms in the presence of HAc are discussed. The results are then compared to CO₂ corrosion mechanisms. The decision to arrange the study this way was made because higher concentrations of HAc can be achieved in the glass cell at atmospheric pressure. Similar methodology is applied to carbonic acid work by subjecting the experimental part to higher pressure in order to study the role of carbonic acid on the cathodic reaction, and thereby determine the corrosion mechanism of mild steel in CO₂ aqueous solution. The research is also extended to the corrosion mechanisms of mild steel in other weak-acid environments, specifically formic acid, water, and hydrogen sulfide. An electrochemical model was then developed based on the proposed mechanism, taking into account important parameters (i.e., pH, temperature, flow, partial pressure of CO₂) that affect the corrosion process.

3.2 Hypotheses

3.2.1 HAc corrosion

It remains important to distinguish the two principal mechanisms in HAc corrosion of mild steel (direct reduction versus buffering effect), not least because the corrosion rate behavior and prediction depends strongly on the chosen pathway. If direct reduction of HAc is dominant at the steel surface, the corrosion rate will steadily increase

with the increasing HAc concentration (at the same pH), irrespective of the rate controlling step (charge or mass transfer control, Figure 5). This is due to an increase of both the charge and mass transfer limiting currents with increasing HAc concentration (as show in Figure 6). However, if the dominant cathodic reaction at the metal surface is the reduction of hydrogen ions, as proposed by the buffering effect, the corrosion rate will stop increasing beyond a certain HAc concentration (Figure 5). This happens when the cathodic reaction rate control shifts from mass transfer (which responds to HAc concentration) to charge transfer of hydrogen ions, which is insensitive to HAc concentration (Figure 7).

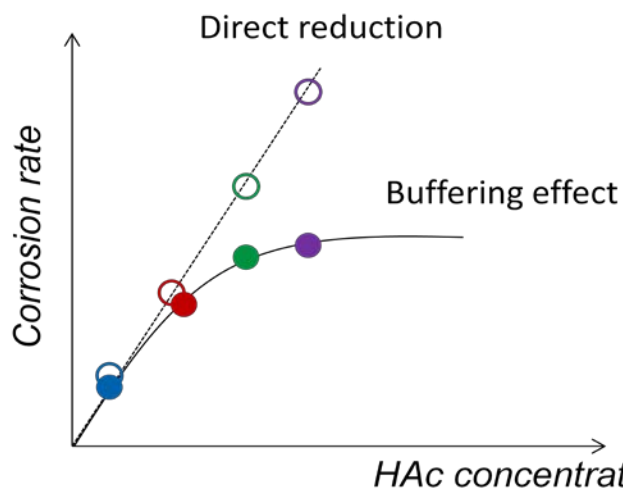


Figure 5: Illustration of corrosion rate change as a function of HAc concentration for direct reduction and buffering effect mechanism (at same pH).

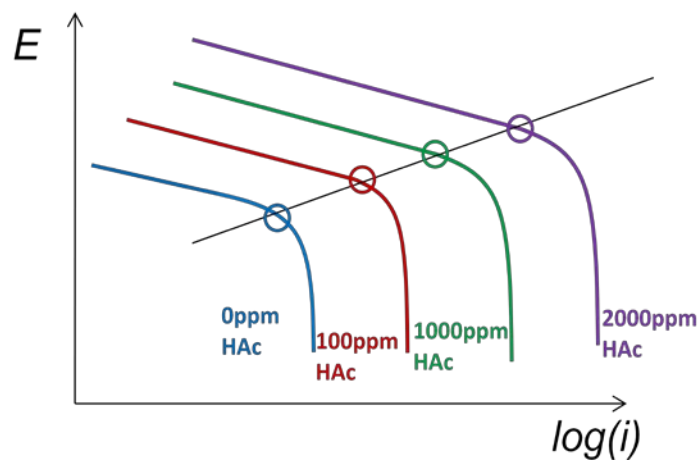


Figure 6: Illustration of cathodic behavior if direct reduction of HAc were dominant, with points indicating the intersection between the anodic line and the cathodic line.

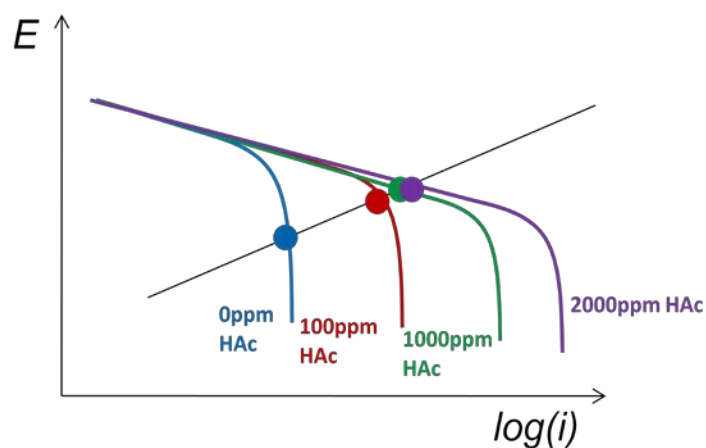


Figure 7: Illustration of cathodic behavior if the buffering effect mechanism were dominant, with points indicating the intersection between the anodic line and the cathodic line.

3.2.2 CO_2 corrosion

Similar to HAc, the corrosion rate calculation of mild steel in the presence of CO_2 is strongly affected depending on the mechanistic pathway. As shown in Figure 8, if the direct reduction of carbonic acid is assumed, the corrosion rate should increase steadily

with partial pressure of CO_2 , regardless of the controlling step (i.e., mass transfer control or charge transfer control). On the other hand, if the dominant cathodic reaction is the reduction of hydrogen ions, increasing CO_2 partial pressure does not affect the corrosion rate when the corrosion process is charge transfer controlled. This implies that if the buffering effect mechanism is assumed, the corrosion rate should stop increasing beyond a certain partial pressure of CO_2 (Figure 8).

Consequently, if the potential is plotted versus the logarithm of current density, the corrosion mechanism can be revealed. Figure 9 shows an illustration of the cathodic behavior if the direct reduction of carbonic acid is dominant at the surface. The charge transfer current increases in accordance with an increase of CO_2 partial pressure. That explains an increase of the corrosion rate with increasing partial pressure of CO_2 , regardless of the controlling step. On the other hand, if the buffering mechanism is dominant, the charge transfer current remains the same despite the change of CO_2 partial pressure. In this case, when the controlling step shifts from mass transfer to charge transfer, the corrosion rate stops changing beyond a certain CO_2 partial pressure. In both mechanisms, an increase of limiting currents is observed due to the ability of carbonic acid to replenish hydrogen ions via dissociation as the latter are consumed at the steel surface by the corrosion reaction.

A summary of the hypotheses and expected results are shown in Figure 11.

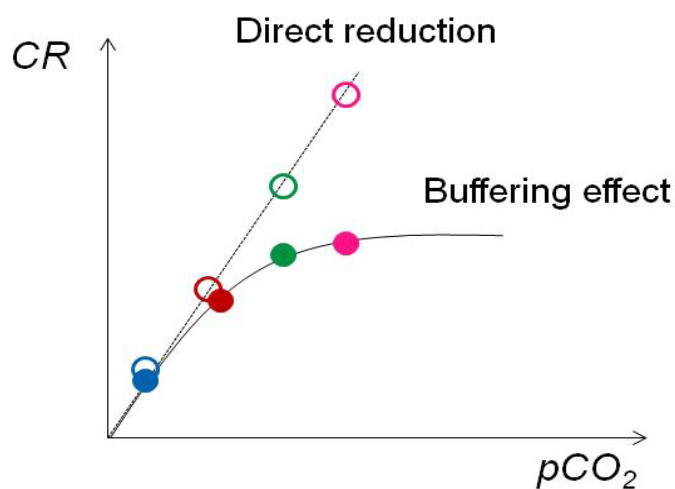


Figure 8: Illustration of corrosion rate change as a function of CO_2 partial pressure for direct reduction and buffering effect mechanism.

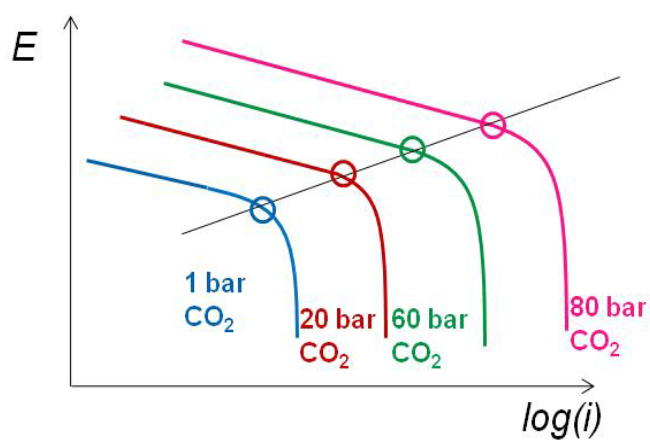


Figure 9: Illustration of cathodic behavior if direct reduction of carbonic acid were dominant at the surface, with points indicating the intersection between the anodic line and the cathodic line.

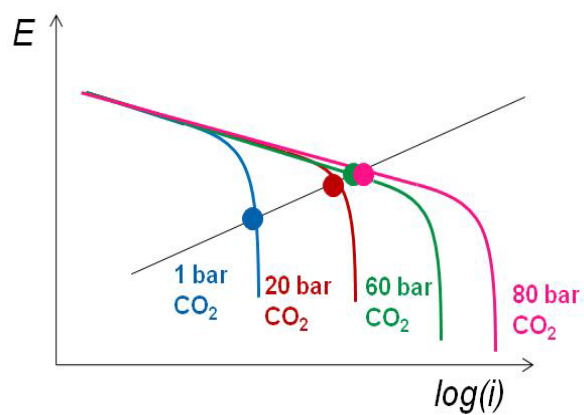


Figure 10: Illustration of cathodic behavior if buffering effect mechanism is dominant, with points indicating the intersection between the anodic line and the cathodic line.

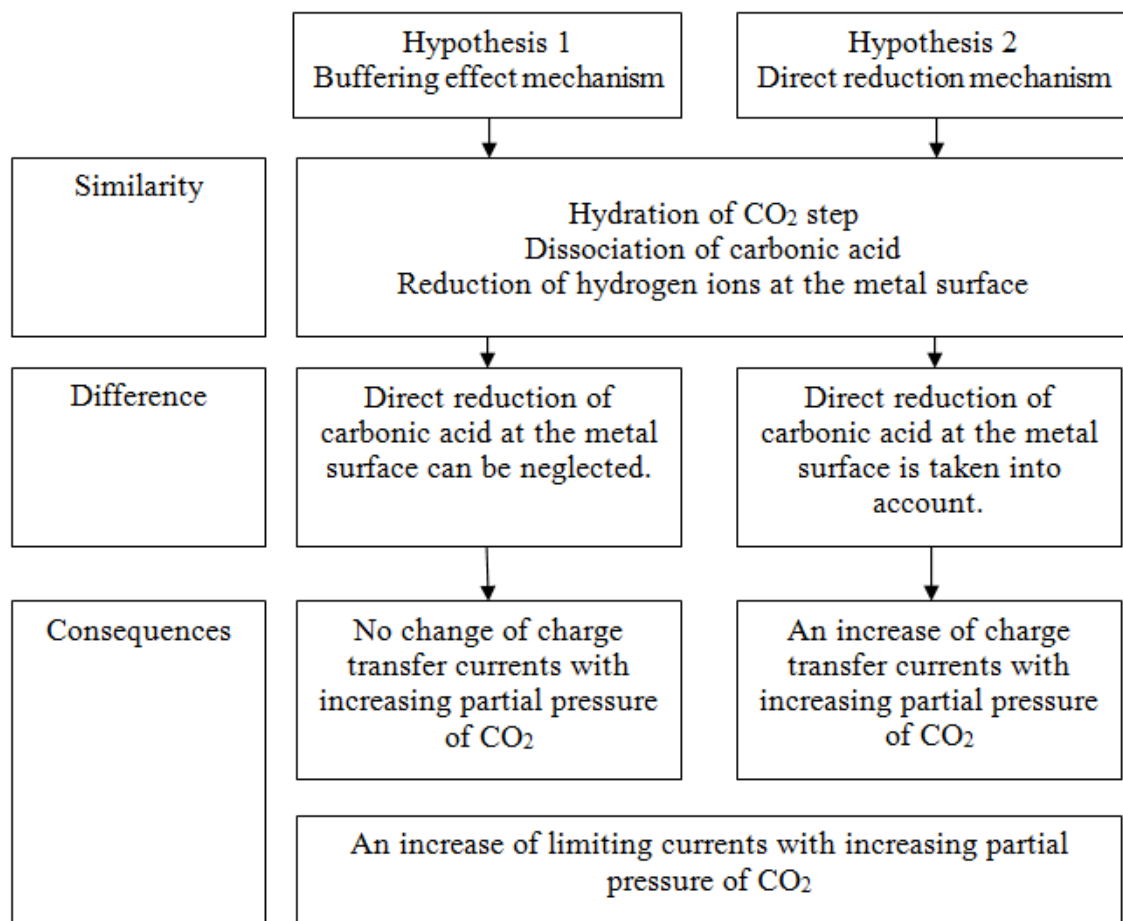


Figure 11: Similarities and differences between buffering effect and direct reduction mechanism, and expected consequences from each mechanism.

CHAPTER 4: METHODOLOGY AND EXPERIMENTAL DESIGN

4.1 Methodology

As discussed in the previous chapter, the main difference between the buffering effect and direct reduction mechanisms is the nature of the cathodic reaction. In the former case, the reduction of hydrogen ions is solely considered. In the latter, both reduction of hydrogen ions and carbonic acid or HAc is taken into account. So, an increase of charge transfer current should be observed when HAc concentration or CO₂ partial pressure increases if the rate of the direct reduction of HAc or carbonic acid is important at the steel surface. However, in previous corrosion studies it has been difficult to resolve this issue as the charge transfer region for the hydrogen ion reduction overlaps with the region where the dominant reaction is anodic dissolution of iron (for example, studies conducted by George on X65 mild (pipeline) steel) [18]. This led to a choice of different substrates in the current work studying HAc and H₂CO₃ reduction mechanisms. After testing noble metals (platinum and gold), the best and most consistent results were achieved using a passive metal—a stainless steel SS304 electrode. The charge transfer current produced by the reduction of hydrogen ions on SS304 could be examined without interference from the iron dissolution reaction. An additional benefit of using a stainless steel electrode is its “similarity” to mild steel, where the strong catalytic effects of hydrogen reduction seen on noble metals were avoided. As Figure 12 shows, the cathodic reactions (where they overlapped) on the two steels (SS304 and X65) under the same environmental conditions were similar. Because of the similar reaction, it was assumed that the mechanisms of HAc and H₂CO₃ cathodic reactions on mild steel could be

ascertained by examining the behavior of the same reaction on stainless steel at comparable conditions. Nickel alloy (Ni200) was also used in order to verify that the cathodic reaction is similar as it is on both stainless and mild steels. The chemical compositions of the X65 mild steel, 304 stainless steel, and 200 nickel alloy used in the research are shown in Table 2, Table 3, and Table 4. In a separate study, instead of using a different substrate, experiments done on mild steel in the presence of an anodic inhibitor were also shown to strengthen the validity of the proposed mechanism.

Electrochemical techniques such as polarization sweeps and electrochemical impedance spectroscopy (EIS) were used to measure the cathodic current and the solution resistance, respectively. All sweeps were then corrected using solution resistance. By using these electrochemical measurements, the charge transfer current on stainless steel could be observed. As discussed in chapter 3, by changing HAc concentration or partial pressure of CO₂, if the charge transfer current remains the same, the direct reduction of HAc or carbonic acid is irrelevant (Figure 7 and Figure 10). On the contrary, if the charge transfer current changes with increasing HAc concentration, or partial pressure of CO₂, the direct reduction of HAc or carbonic acid becomes important (Figure 6 and Figure 9). Linear polarization resistance (LPR) was used to measure the corrosion rates on mild steel to confirm the mechanism. Weight loss was also used for comparisons to the corrosion rates determined by LPR measurements. The corrosion rate calculation from LPR and weight loss method is shown in Appendix A.

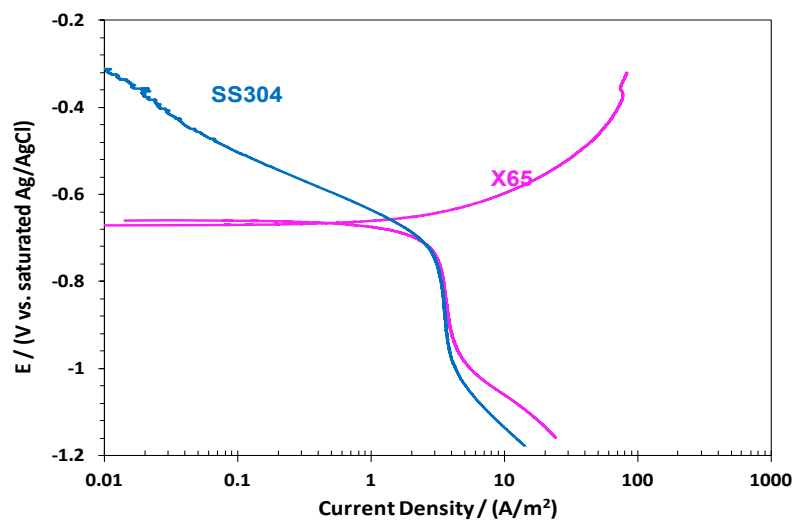


Figure 12: Comparison of cathodic sweeps of SS304 and X65, at 25°C, pH4.0, 1 bar pCO₂, 3 wt. percent NaCl, 1000 rpm.

Table 2: Chemical composition of carbon steel X65 (mass percent).

Fe	C	Mn	Si	P	S	Cr	Mo	Ni	Al	Cu
97.373	0.14	1.18	0.24	0.01	0.24	0.14	0.14	0.38	0.037	0.12

Table 3: Chemical composition of stainless steel SS304 (mass percent).

Fe	Ni	Cr	C	Mn	Si	P	S
66.6	10.5	20	0.08	2	0.75	0.04	0.03

Table 4: Chemical composition of stainless steel Ni200 (mass percent).

Ni	Fe	C	Mn	Si
99.67	0.03	0.03	0.24	0.03

4.2 Experimental setup

The experiments were conducted in a 2 L glass cell at atmospheric pressure and a 7.5 L autoclave at high pressure (Figure 13 and Figure 14). The autoclave is made of SS316 and is designed for a maximum working pressure of 350 bars and working temperature of 300°C. A rotating cylinder electrode (RCE) was used as the working electrode in the glass cell. A stationary electrode was used as the working electrode in the autoclave, where the solution was stirred by an impeller. Saturated Ag/AgCl reference electrodes and platinum counter-electrodes were used in both setups. The pH was monitored and the temperature controlled during the experiments.

Part of the HAc study was performed at the University of Pierre and Marie Curie (France), using a rotating disk electrode (RDE) with a slightly different experimental arrangement to further validate the results. The RDE operates under a well-defined laminar flow regime and is a common setup used to examine electrochemical reaction mechanisms [17,73]. The RCE typically operates under turbulent flow conditions, and is a standard tool to investigate flow sensitive corrosion [10,41]. In both cases, well defined mass transfer correlations exist [73,74]. The schematic for the specimens used in the glass cell for a RCE and a RDE, and in the autoclave, is shown in Figure 15.

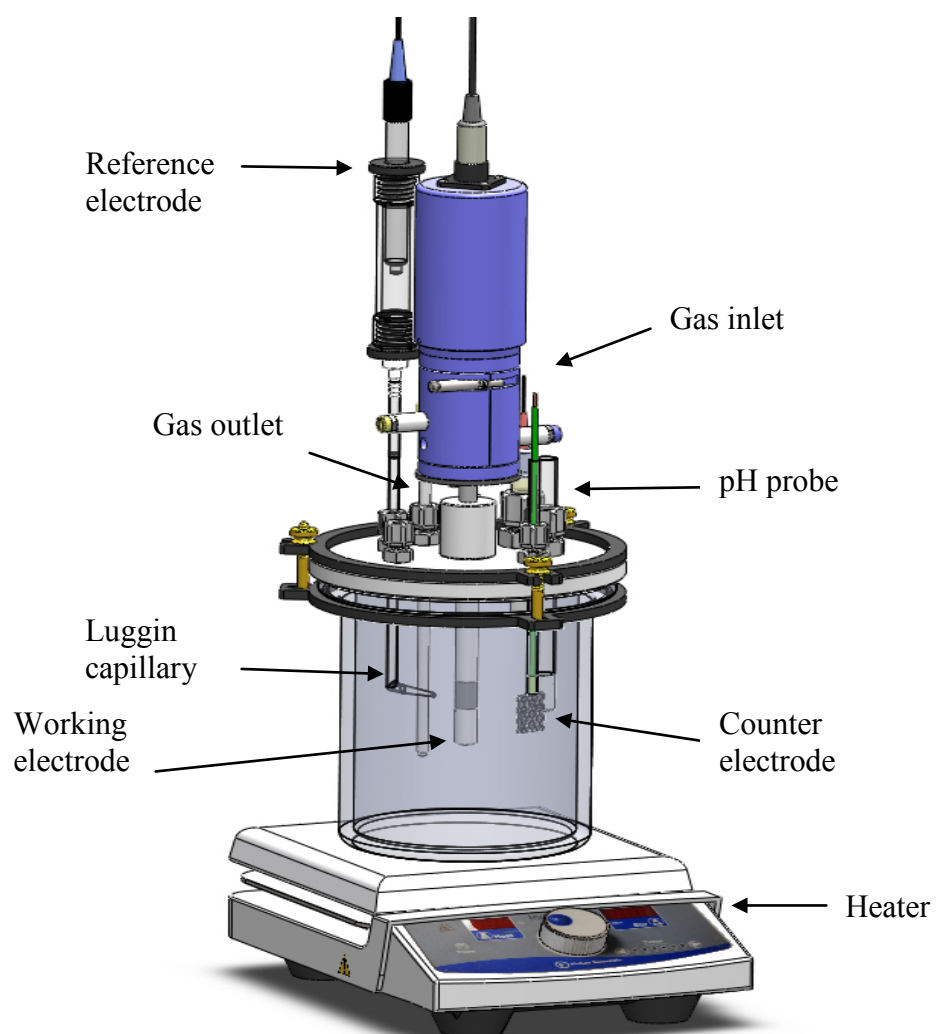


Figure 13: Schematic of a 2 L glass cell. Images courtesy of Cody Shafer, ICMT.

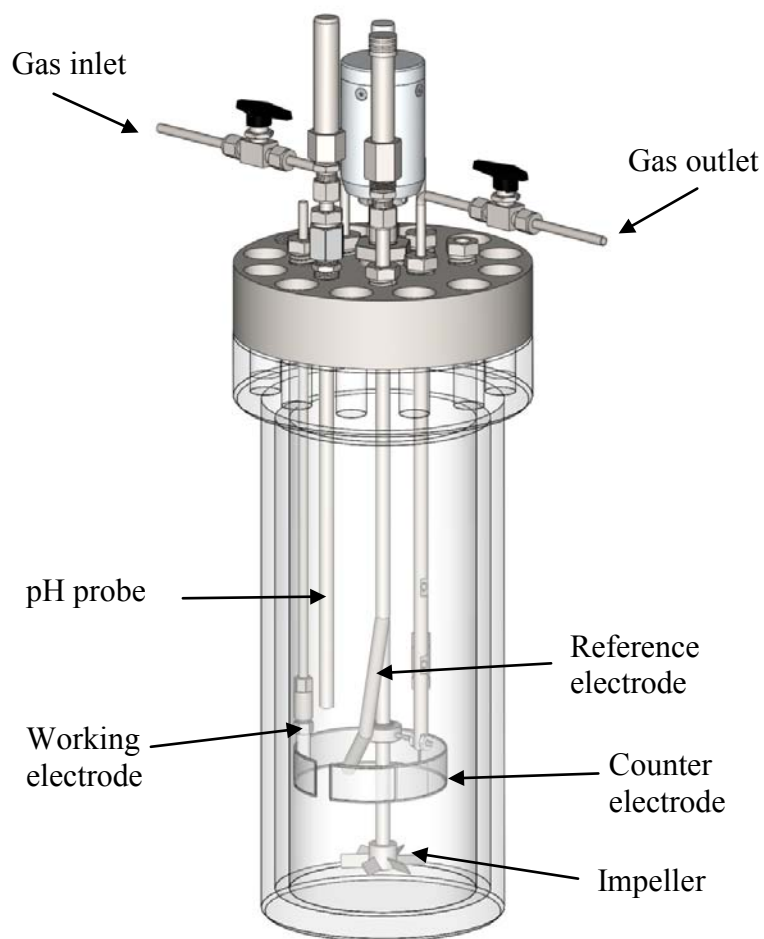


Figure 14: Schematic of a 7.5 L autoclave. Images courtesy of Cody Shafer, ICMT).

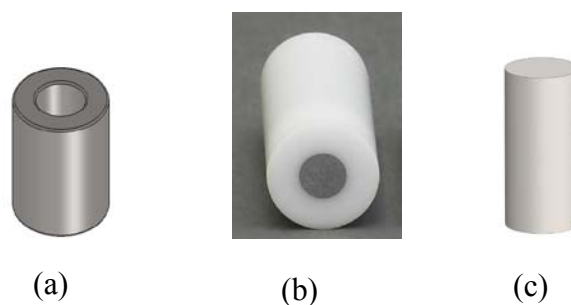


Figure 15: Schematic of the sample used for working electrode: a) RCE specimen used for glass cell experiment (area of 5.4 cm^2); b) RDE specimen used for glass cell experiment (area of 0.2 cm^2); c) Specimen used for autoclave experiment (area of 6.0 cm^2).

4.3 Test matrix and experimental procedures

4.3.1 HAc corrosion

As proposed in the methodology section, the key point that can distinguish the direct reduction from the buffering effect is whether the charge transfer current is sensitive to the change in HAc concentration. The plan in the experiments was to fix the pH, and then observe whether HAc concentration influenced the charge transfer current. For comparison, the known effect of pH on the charge transfer current was also confirmed. The test matrix is shown in Table 5 - Table 9.

Table 5: Test matrix to test the effect of HAc concentration on the charge transfer current at pH4.

Parameters	Conditions
Equipment	Glass cell
Material	SS304
Temperature (°C)	25 ± 1
Total pressure (bar)	1
CO ₂ partial pressure (bar)	0
pH	4.0 ± 0.1
Acetic acid concentration (ppm)	0, 100, 1000 (±0.6%)
Electrolyte	3 wt. % NaCl
RCE Rotating Speed (rpm)	1000

Table 6: Test matrix to test the effect of HAc concentration on the charge transfer current at pH3.

Parameters	Conditions
Equipment	Glass cell
Material	SS304
Temperature (°C)	25 ± 1
Total pressure (bar)	1
CO ₂ partial pressure (bar)	0
pH	3.0 ± 0.1
Acetic acid concentration (ppm)	0, 100, 1000 (±0.6%)
Electrolyte	3 wt. % NaCl
RCE Rotating Speed (rpm)	1000

Table 7: Test matrix to test the effect of HAc concentration on the charge transfer current at 80°C.

Parameters	Conditions
Equipment	Glass cell
Material	SS304
Temperature (°C)	80 ± 1
Total pressure (bar)	1
CO ₂ partial pressure (bar)	0
pH	4.0 ± 0.1
Acetic acid concentration (ppm)	0, 100, 1000 (±0.6%)
Electrolyte	3 wt. % NaCl
RCE Rotating Speed (rpm)	1000

Table 8: Test matrix to test the effect of pH on the charge transfer current without the presence of HAc.

Parameters	Conditions
Equipment	Glass cell
Material	SS304
Temperature (°C)	25 ± 1
Total pressure (bar)	1
CO ₂ partial pressure (bar)	0
pH	2.0, 3.0, 4.0 (± 0.1)
Acetic acid concentration (ppm)	0
Electrolyte	3 wt. % NaCl
RCE Rotating Speed (rpm)	1000

Table 9: Test matrix to test the effect of pH on the charge transfer current in the presence of HAc.

Parameters	Conditions
Equipment	Glass cell
Material	SS304
Temperature (°C)	25 ± 1
Total pressure (bar)	1
CO ₂ partial pressure (bar)	0
pH	2.0, 3.0, 4.0 (± 0.1)
Acetic acid concentration (ppm)	100 ± 0.6%
Electrolyte	3 wt. % NaCl
RCE Rotating Speed (rpm)	1000

4.3.1.1 Experimental procedure

All experiments with HAc were conducted in the glass cell at atmospheric pressure. The glass cell was filled with 3 wt. percent NaCl aqueous electrolyte. Before each experiment, the solution was purged with nitrogen for at least one hour to achieve electrolyte deoxygenation.

Due to dissociation the added acid is present as either undissociated HAc, or acetate ion (reaction 17). Therefore, the total amount of HAc added to the glass cell, $[HAc_{tot}]$, can be calculated from the desired undissociated HAc concentration $[HAc]$ using the equilibrium expression (equation 18), constant K_a , and the desired pH (hydrogen ion concentration $[H^+]$):

$$[HAc_{tot}] = [HAc] \left(1 + \frac{K_a}{[H^+]} \right) \quad (22)$$

Where K_a is a function of temperature T_K (in Kelvin): [75]

$$K_a = 10^{-(6.66104 - 0.001349 \times T_K + 2.37856 \times 10^{-5} \times T_K^2)} \quad (23)$$

In this work the HAc concentration refers to the undissociated HAc concentration $[HAc]$, unless otherwise stated.

To achieve the desired pH at a given HAc concentration, the pH was adjusted by adding deoxygenated hydrochloric acid or sodium hydroxide. Before immersion into the test solution, the stainless steel electrodes were polished using 400 and 600 grit silicon carbide paper, washed with isopropyl alcohol and air dried.

The electrochemical tests started when the measured open circuit potential (OCP) stabilized to within ± 1 mV over at least two minutes. The electrochemical impedance spectroscopy (EIS) measurements were conducted by applying an oscillating potential of ± 10 mV around the OCP using a frequency range from 10,000 Hz to 0.01 Hz to determine the solution resistance. For the cathodic sweeps, the working electrode was polarized from the open circuit potential in the negative direction using a scan rate of 0.2 mV/s. The cathodic sweeps were corrected with the measured solution resistance from EIS.

4.3.2 *CO₂ corrosion*

The goal of the experiments in aqueous CO₂ environments is also to determine whether changing the concentration of carbonic acid (and consequently CO₂ partial pressure) at a fixed pH will affect the charge transfer current. For comparison, the effect of pH on the charge transfer current is also confirmed. A test matrix for each set of studied condition is shown in Table 10-Table 16.

Table 10: Test matrix to test the effect of H_2CO_3 concentration on the charge transfer current at pH4.

Parameters	Conditions
Equipment	Autoclave
Material	SS304, Ni200
Temperature ($^{\circ}\text{C}$)	25 ± 1
Total pressure (bar)	1, 10 ± 0.5
CO_2 partial pressure (bar)	0.97, 9.97
pH	4.0 ± 0.1
Electrolyte	3 wt. % NaCl
Stirring Speed (rpm)	800

Table 11: Test matrix to test the effect of H_2CO_3 concentration on the charge transfer current at pH5.

Parameters	Conditions
Equipment	Autoclave
Material	SS304
Temperature ($^{\circ}\text{C}$)	25 ± 1
Total pressure (bar)	1, 10 ± 0.5
CO_2 partial pressure (bar)	0.97, 9.97
pH	5.0 ± 0.1
Electrolyte	3 wt. % NaCl
Stirring Speed (rpm)	800

Table 12: Test matrix to test the effect of H_2CO_3 concentration on the charge transfer current at pH6.

Parameters	Conditions
Equipment	Autoclave
Material	SS304
Temperature ($^{\circ}\text{C}$)	25 ± 1
Total pressure (bar)	1, 10 ± 0.5
CO_2 partial pressure (bar)	0.97, 9.97
pH	6.0 ± 0.1
Electrolyte	3 wt. % NaCl
Stirring Speed (rpm)	800

Table 13: Test matrix to test the effect of H_2CO_3 concentration on the charge transfer current at 80°C .

Parameters	Conditions
Equipment	Autoclave
Material	SS304
Temperature ($^\circ\text{C}$)	80 ± 1
Total pressure (bar)	1, 10 ± 0.5
CO_2 partial pressure (bar)	0.97, 9.97
pH	6.0 ± 0.1
Electrolyte	3 wt. % NaCl
Stirring Speed (rpm)	800

Table 14: Test matrix to test the effect of pH on the charge transfer current without CO_2 .

Parameters	Conditions
Equipment	Glass cell
Material	SS304
Temperature ($^\circ\text{C}$)	25
Total pressure (bar)	1
CO_2 partial pressure (bar)	0
pH	4.0, 5.0 ± 0.1
Electrolyte	3 wt. % NaCl
RCE Rotating Speed (rpm)	1000

Table 15: Test matrix to test the effect of pH on the charge transfer current at 0.97 bar pCO_2 .

Parameters	Conditions
Equipment	Glass cell
Material	SS304
Temperature ($^\circ\text{C}$)	25
Total pressure (bar)	1
CO_2 partial pressure (bar)	0.97
pH	4.0, 5.0, 6.0 ± 0.1
Electrolyte	3 wt. % NaCl
RCE Rotating Speed (rpm)	1000

Table 16: Test matrix to test the effect of pH on the charge transfer current at 9.97 bar $p\text{CO}_2$.

Parameters	Conditions
Equipment	Autoclave
Material	SS304
Temperature ($^{\circ}\text{C}$)	25
Total pressure (bar)	10 ± 0.5
CO_2 partial pressure (bar)	9.97
pH	4.0, 5.0, 6.0 ± 0.1
Electrolyte	3 wt. % NaCl
Stirring Speed (rpm)	800

4.3.2.1 Experimental procedure - Glass cell experiment

The glass cell was filled with 2 L of deionized water and 3 wt. percent NaCl. The solution was bubbled with N_2 or CO_2 gas for at least one hour to facilitate deoxygenation and saturation with N_2 or CO_2 . In the case of CO_2 , the pH was measured and verified at 3.9 ± 0.1 (the autogenous pH for a saturated CO_2 solution at atmospheric pressure). Hydrochloric acid (HCl) or sodium bicarbonate (NaHCO_3) was added to the solution to achieve the desired pH. Before immersion into the test solution, the X65 specimen was polished with 150, 400, and 600 grit silicon carbide paper using isopropyl alcohol, and then cleaned with isopropyl alcohol in an ultrasonic bath for five minutes. The SS304 specimen was polished with 400 and 600 grit silicon carbide paper using water, and was also cleaned with isopropyl alcohol in an ultrasonic bath for five minutes.

Following immersion, electrochemical tests were initiated after the measured corrosion potential (OCP) stabilized within ± 1 mV over at least two minutes. The EIS measurements were conducted by applying an oscillating potential of ± 10 mV around the OCP using a frequency range from 10,000 Hz to 0.01 Hz to determine solution

resistance. For the X65 specimens, LPR was then measured by polarizing the specimen from -5 mV vs. OCP to +5 mV vs. OCP. Cathodic sweeps were then performed from the OCP in the negative direction with a scan rate of 0.2 mV/s. After waiting 30 minutes for the OCP to stabilize at its original value before the cathodic sweep, an anodic sweep was conducted from the OCP in the positive direction with the same scan rate. For the SS304 specimens, after measuring the solution resistance from EIS, only the cathodic sweep was performed.

4.3.2.2 Autoclave experiment

The 7.5 L autoclave was filled with 5 L of deionized water and 3 wt. percent NaCl. The solution was bubbled with CO₂ gas for at least two hours to facilitate deoxygenation and saturation with CO₂ at atmospheric pressure. The pH was measured and verified to be 3.9 ± 0.1 (the autogenous pH for a saturated CO₂ solution at atmospheric pressure). Sodium bicarbonate was added to the solution to achieve the pH desired at high pressure. The X65 specimens were polished sequentially with 150, 400, and 600 grit silicon carbide paper using isopropyl alcohol, and cleaned with isopropyl alcohol in an ultrasonic bath for five minutes. The SS304 and Ni200 specimens were polished sequentially with 400 and 600 grit silicon carbide paper using water, and cleaned with isopropyl alcohol in an ultrasonic bath for five minutes. After being dried with cold air, the specimen was mounted on the shaft of an autoclave lid. The autoclave lid was then installed with continuous CO₂ purging of the electrolyte at one atmosphere.

The partial pressure of CO₂ was then increased to the desired conditions. After several hours, the solution was CO₂ saturated, confirmed by measuring the pH.

For the SS304 and Ni200 specimens, the electrochemical tests started when the OCP stabilized within ± 1 mV over at least two minutes. The EIS measurements were conducted by applying an oscillating potential of ± 10 mV around the OCP using a frequency range from 10,000 Hz to 0.01 Hz to get the solution resistance. The cathodic sweeps were performed from the OCP in the negative direction with a scan rate of 0.2 mV/s. For the X65 specimens, the electrochemical tests started when the measured OCP stabilized within ± 1 mV over at least two minutes. The EIS measurements were conducted by applying an oscillating potential of ± 10 mV around the OCP using a frequency range from 10,000 Hz to 0.01 Hz to obtain the solution resistance. After two hours, LPR was measured every 30 minutes for three hours to make sure that the corrosion rate was constant before performing the cathodic sweeps from the OCP in the negative direction with a scan rate of 0.2 mV/s. After the cathodic sweeps and another 30 minutes, the OCP stabilized to the initial value, and the anodic sweeps were performed from the OCP in the positive direction with the same scan rate. All sweeps were corrected using the measured solution resistance from EIS results.

It is also important to note that the flow in the autoclave was produced by an impeller while a rotating cylinder electrode was used in the glass cell. With this setup and positioning of the electrodes, it was proven that an 800rpm stirring speed in the autoclave, using the impeller, provides similar mass transfer compared to a glass cell

RCE at 1000 rpm (see Appendix B). Therefore, the 800 rpm stirring speed was chosen for all experiments conducted in the autoclave.

CHAPTER 5: RESULTS AND DISCUSSIONS

Portions of this chapter have been previously published at NACE (National Association of Corrosion Engineers) International conferences and in the Corrosion Journal [29,30].

5.1 Acetic acid corrosion mechanism

5.1.1 Introduction

HAc is recognized as an important factor in mild steel corrosion. According to many studies, HAc enhances the corrosion rate of mild steel by accelerating the cathodic reaction. However, the mechanism of HAc reduction at the steel surface is still debated. If the role of HAc is to dissociate near the metal surface and to provide additional hydrogen ions, and the dominant cathodic reduction is reduction of hydrogen ions, the mechanism is the buffering effect. If the reduction of adsorbed HAc is considered, the mechanism is direct reduction.

In this chapter, electrochemical techniques such as EIS and polarization sweeps are used to investigate the corrosion mechanism in the presence of HAc.

5.1.2 Results and Discussion

As hypothesized above, if the buffering effect mechanism is correct, the following processes occur:

- Dissociation of HAc to form hydrogen ions and acetate ions in the bulk (reaction 19).

- Transport of hydrogen ions (reactions 13) from the bulk to the metal surface.
- Reduction of adsorbed hydrogen ions at the metal surface (reaction 14).
- Dissolution of iron to release ferrous ions (reaction 8).

In this mechanism, the role of HAc is to act as a reservoir of hydrogen ions. HAc provides hydrogen ions via dissociation as they are consumed at the metal surface. As a result, the ability of HAc to provide more hydrogen ions increases with HAc concentration, leading to an increase of the observed limiting currents. The buffering effect mechanism does not account for the direct reduction of HAc at the metal surface. Therefore, HAc should have a negligible effect on the charge transfer current, which is a consequence of electrochemical reactions occurring at the metal surface. On the other hand, if HAc is directly reduced at the steel surface, the charge transfer current will increase with increasing HAc concentration. The limiting current will also increase when more HAc is present due to its ability to dissociate and provide hydrogen ions.

The key difference between the buffering effect and direct reduction mechanism is how the charge transfer current responds to a change of HAc concentration. Cathodic polarization was performed at a fixed pH (constant hydrogen ion concentration) at different HAc concentrations to determine if the presence of HAc affects the charge transfer current. If the charge transfer current responds to the change of HAc concentration, the direct reduction of HAc has to be considered (Figure 6). Conversely, if the charge transfer current remains the same despite the change of HAc concentration, the buffering effect mechanism is dominant (Figure 7).

5.1.2.1 Polarization sweep results

Potentiodynamic sweeps were performed at a constant pH in order to investigate the effect of HAc concentration on the charge transfer current. Figure 16 and Figure 17 show the cathodic reaction rate on stainless steel at different concentrations of HAc at pH4 by using rotating cylinder electrode (RCE) and rotating disk electrode (RDE) experimental configurations, respectively. At pH4, an increase of HAc concentration only affects the limiting current arising from mass transfer, but has no influence on the charge transfer current (Figure 16 and Figure 17). The same results were obtained in laminar and turbulent flow regime (using the RDE and RCE, respectively). This indicates that, other than the reduction of hydrogen ions, there are no significant cathodic reactions at the metal surface. Similar results were observed at pH3 (Figure 18), where again the HAc concentration had no effect on the charge transfer current. Even at 80°C (Figure 19), where the condition is favorable for the direct reduction of HAc, the charge transfer current is still unaffected by HAc concentration. In other words, under all these conditions, HAc acts primarily as a source of hydrogen ions, thus only causes an increase in the mass transfer controlled limiting current for hydrogen evolution.

Most of experiments were repeated at least once to evaluate the reproducibility (see Appendix B). For example, when the concentration of HAc was increased from 0 to 100 and 1000 ppm at a fixed pH, the repeated experiments show an overlap of the charge transfer currents within the measurement uncertainty of the instrument (which is less than 10% of the measured values). On the other hand, when the hydrogen ion concentration was increased tenfold, the repeated experiments show that the charge transfer currents are

significantly different as theoretically expected and the difference is beyond the measurement uncertainty of the instrument, irrespective whether or not HAc is present.

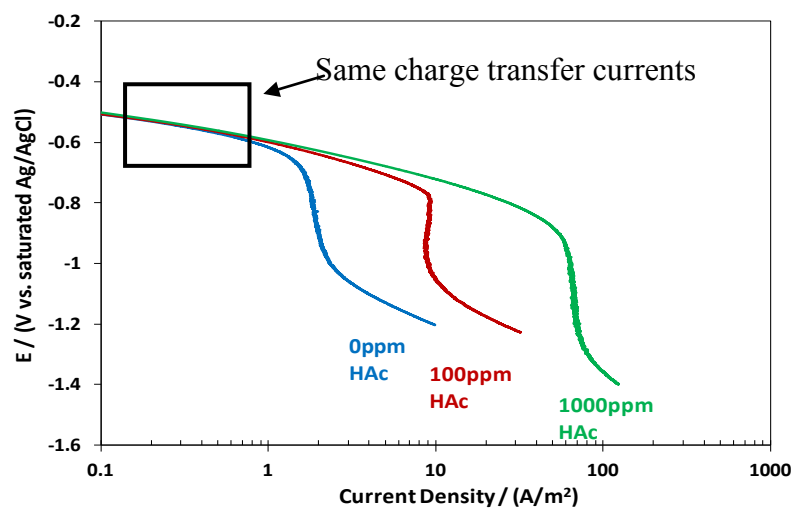


Figure 16: Comparison of potentiodynamic sweeps obtained using a SS304 for different HAc concentrations at 25°C, saturated N₂ solution, pH4.0, 3wt.% NaCl, RCE rotating speed 1000 rpm.

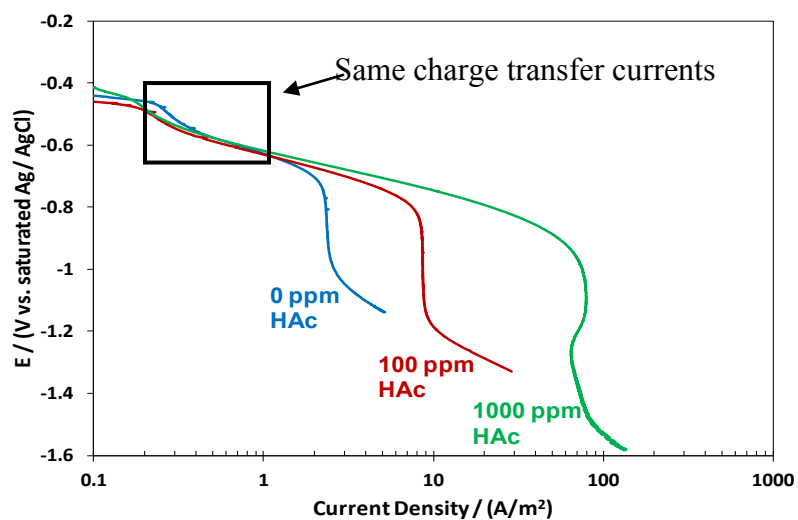


Figure 17: Comparison of potentiodynamic sweeps obtained using a SS304 for different HAc concentrations at 25°C, saturated N₂ solution, pH4.0, 3 wt.% NaCl, RDE rotating speed 1000 rpm.

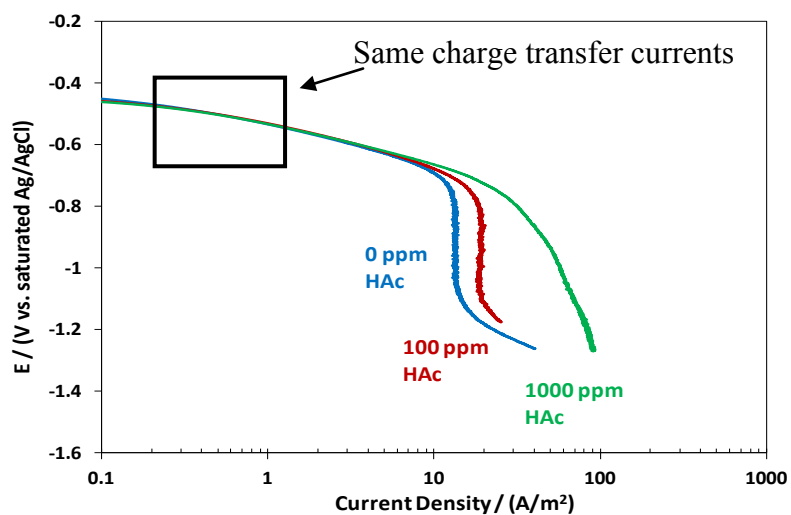


Figure 18: Comparison of potentiodynamic sweeps obtained using a SS304 for different HAc concentrations at 25°C, saturated N₂ solution, pH3.0, 3 wt.% NaCl, RCE rotating speed 1000 rpm.

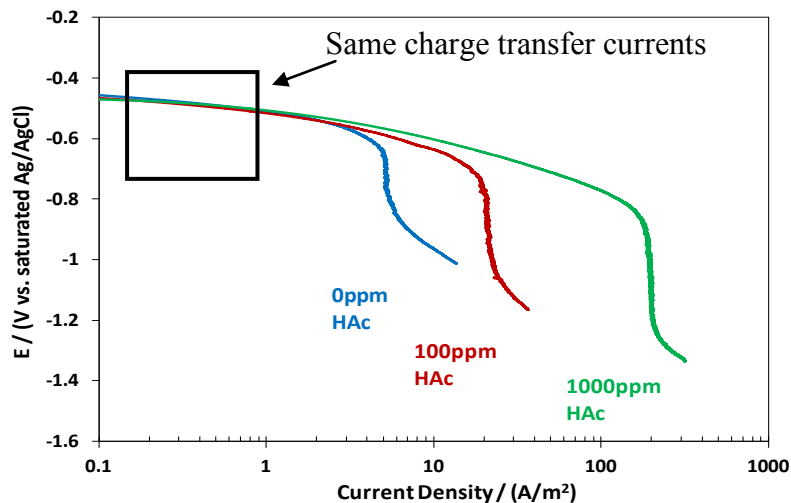


Figure 19: Comparison of potentiodynamic sweeps obtained using a SS304 for different HAc concentrations at 80°C, saturated N_2 solution, pH4.0, 3 wt.% NaCl, RCE rotating speed 1000 rpm.

Since hydrogen ions appear to be the dominant cathodic reactants, the change of hydrogen ion concentration should affect the charge transfer current. Indeed, Figure 20 and Figure 21 show a change of charge transfer current when pH changes. This was observed irrespective of whether HAc was present or not. In both cases, a higher charge transfer current is expected when pH decreases (i.e., the hydrogen ion concentration increases). This result confirms that hydrogen ions are the main cathodic reactant in the systems studied in this work.

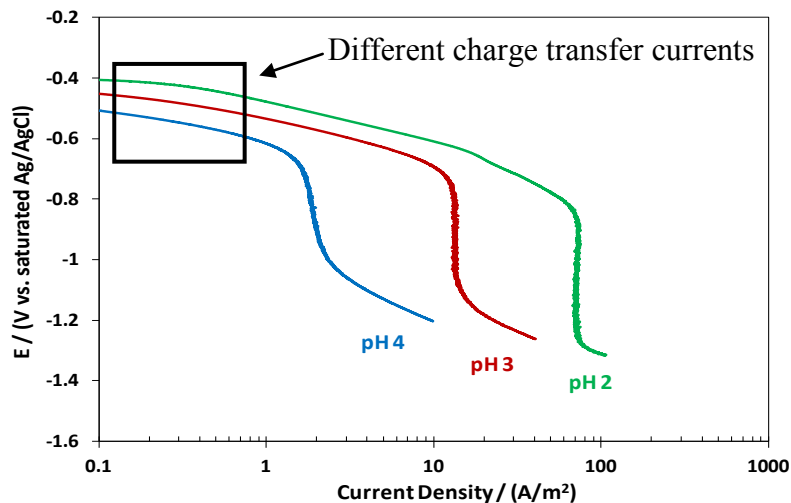


Figure 20: Comparison of potentiodynamic sweeps obtained using a SS304 for different pH at 25°C, saturated N₂ solution, 0 ppm HAc with 3 wt.% NaCl, RCE rotating speed 1000 rpm.

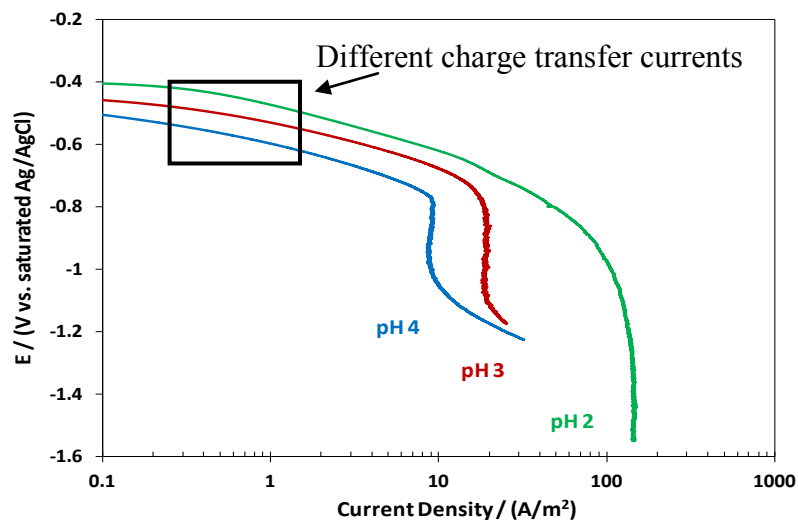


Figure 21: Comparison of potentiodynamic sweeps obtained using a SS304 for different pH at 25°C, saturated N₂ solution, 100 ppm HAc with 3 wt.% NaCl, RCE rotating speed 1000 rpm.

5.1.2.2 EIS results

From the potentiodynamic sweeps, it appeared that the charge transfer rates remain the same with an increase of HAc concentration at the same pH. Hence, the charge transfer resistance as measured by EIS should also be the same. EIS measurements were conducted around the fixed potential of -0.6 V vs. a saturated Ag/AgCl electrode, which is in accordance with the potentiodynamic sweeps in the middle of the charge transfer controlled region for the hydrogen reduction reaction. Figure 22 shows the Nyquist plots for 0, 100 and 1000 ppm of HAc at pH4. The charge transfer resistance is roughly the same (about $2000 \pm 500 \Omega \cdot \text{cm}^2$) when the concentration of HAc changes at a fixed pH. If HAc were reduced at the surface, the charge transfer resistance would be expected to change proportionally to the change of HAc concentration at a fixed pH, which is not supported by these results. In addition, since hydrogen ions are the main species reduced at the surface, a decrease of pH leads to an increase of the charge transfer current and hence a decrease of the charge transfer resistance, as expected (Figure 23 and Figure 24).

The EIS results are therefore consistent with the potentiodynamic sweep data. One can draw the conclusion that the direct reduction of HAc at the steel surface is insignificant. The dominant cathodic reaction is the reduction of hydrogen ions.

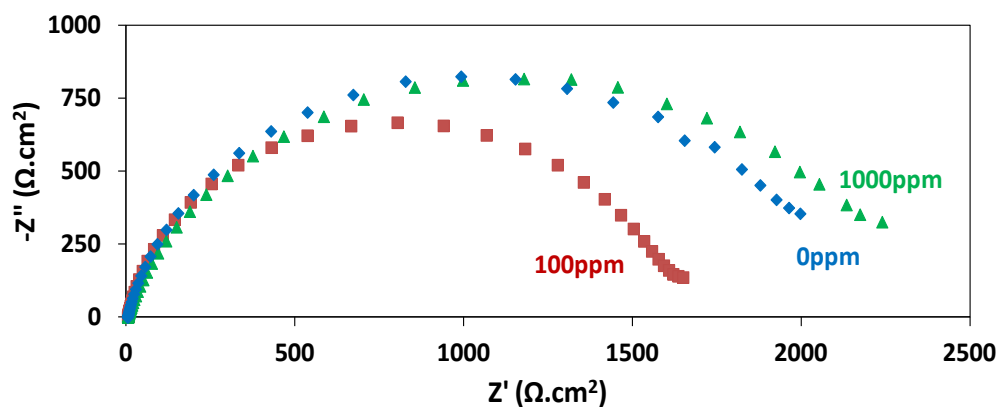


Figure 22: Nyquist plot at -0.6 V vs. a saturated Ag/AgCl electrode for different undissociated HAC concentrations at 25°C, pH4.0, aqueous solution saturated with N_2 , 3 wt.% NaCl, RDE rotating speed 1000 rpm.

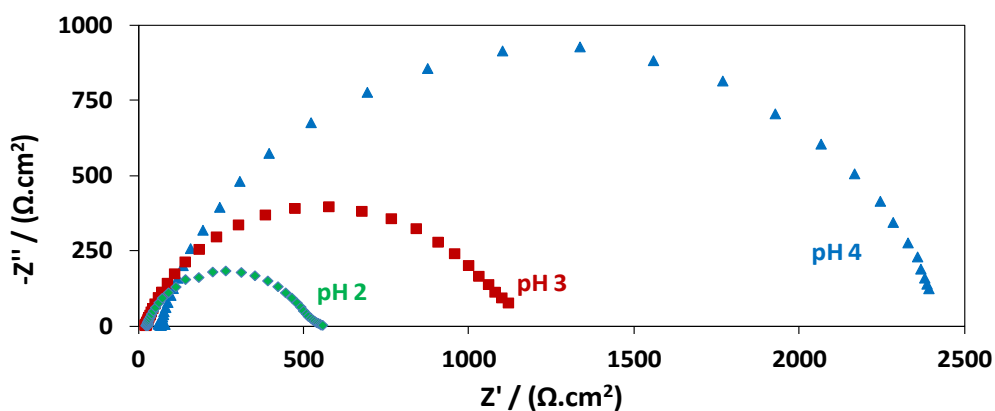


Figure 23: Nyquist plot at -0.6 V vs. a saturated Ag/AgCl electrode obtained by using an SS304 RCE electrode for different pH at 25°C, aqueous solution saturated with N_2 , 0 ppm HAC, 3 wt.% NaCl, RCE rotating speed 1000 rpm.

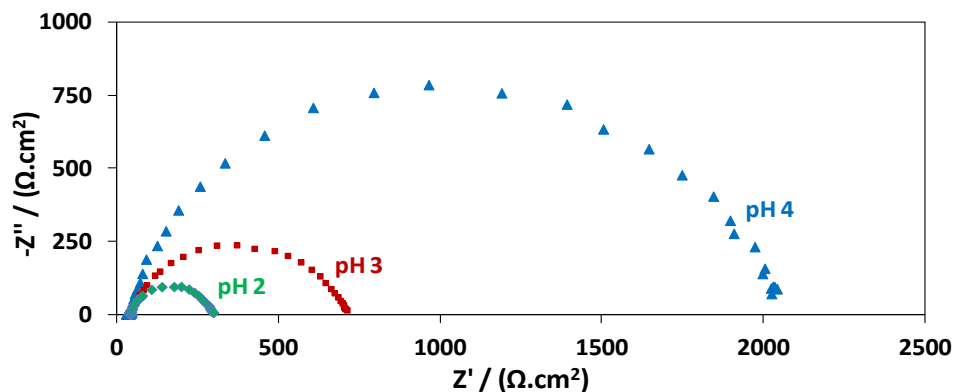


Figure 24: Nyquist plot at -0.6 V vs. a saturated Ag/AgCl electrode obtained by using an SS304 RCE electrode for different pH at 25°C , aqueous solution saturated with N_2 , 100 ppm HAC, 3 wt.% NaCl, RCE rotating speed 1000 rpm.

5.1.3 Conclusions

- The dominant cathodic reaction mechanism related to the reduction of HAC on steel is the buffering effect.
- The presence of HAC only affects the cathodic limiting current due to the ability of HAC to provide the hydrogen ions by dissociation when they are consumed at the metal surface.
- Since no direct reduction of HAC can be detected, HAC appears to have no influence on the charge transfer cathodic current. Hydrogen ions are the dominant cathodic reactants reduced at the metal surface. A change of pH leads to a change of the cathodic charge transfer current, as expected.

5.2 CO₂ corrosion mechanism

5.2.1 Introduction

In the previous section, increasing HAc concentration at atmospheric pressure showed that direct reduction of HAc at the steel surface is negligible, and the dominant cathodic reaction is the reduction of hydrogen ions. Hence, the buffering effect mechanism is dominant. In this section, the same methodology is applied to carbonic acid, a weak acid present in CO₂ corrosion.

Electrochemical techniques such as EIS and potentiodynamic sweeps were used to investigate the effect of carbonic acid on the cathodic reaction. While all previous experimental measurements in the presence of HAc were conducted in the glass cell at atmospheric pressure, part of the experimental measurements in the presence of carbonic acid or CO₂ were conducted in the autoclave with the partial pressure of CO₂ increased to higher than atmospheric pressure. Appendix B shows the difficulty of conducting experiments in the autoclave and improvements made to ensure the repeatability of measurements, as well as to ensure that the experiments at one bar CO₂ conducted in the glass cell are reproducible in the autoclave.

5.2.2 Results and discussion

5.2.2.1 Effect of pH and partial pressure of CO₂ on the cathodic reaction

The purpose of the research described in this section was to confirm the known effect of pH on the cathodic reaction at a fixed partial pressure of CO₂, and then to determine whether direct reduction of carbonic acid at the metal surface needs to be

accounted for in corrosion modeling. The effect of carbonic acid concentration on the cathodic reaction was investigated at a fixed pH.

A decrease of pH, i.e., an increase of hydrogen ion concentration, leads to an increase of charge transfer current whether CO₂ is present or not. Figure 25 shows that in the absence of CO₂ the charge transfer current increases when pH decreases from pH5 to pH4. A similar trend was observed in the presence of CO₂ (at 1 bar and 10 bars) (Figure 26 and Figure 27). These results confirm that hydrogen ions were reduced at the metal surface.

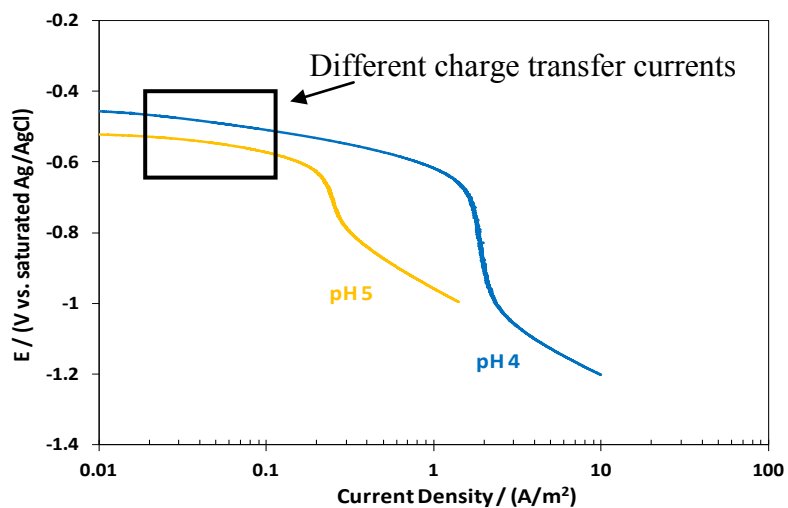


Figure 25: Comparison of charge transfer current on SS304 at different pH, without CO₂, 25°C, 3 wt.% NaCl, RCE rotating speed 1000 rpm.

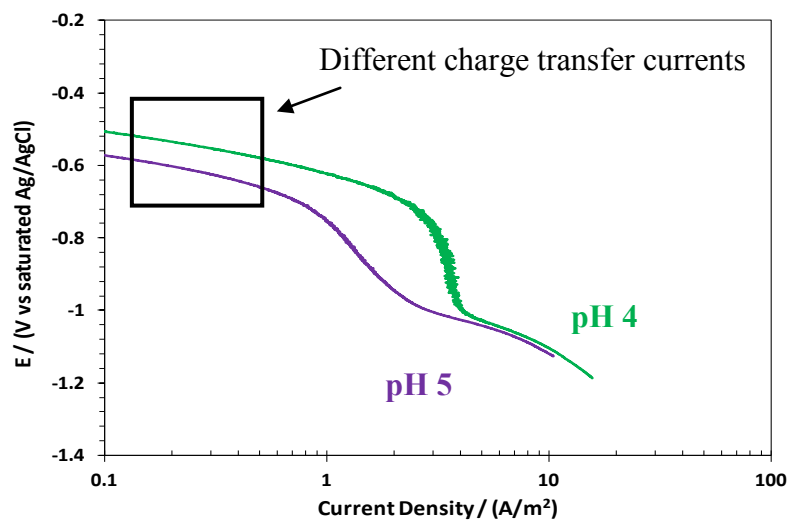


Figure 26: Comparison of charge transfer current on SS304 at different pH, 1 bar $p\text{CO}_2$, 25°C, 3 wt.% NaCl, impeller stirring speed 800 rpm.

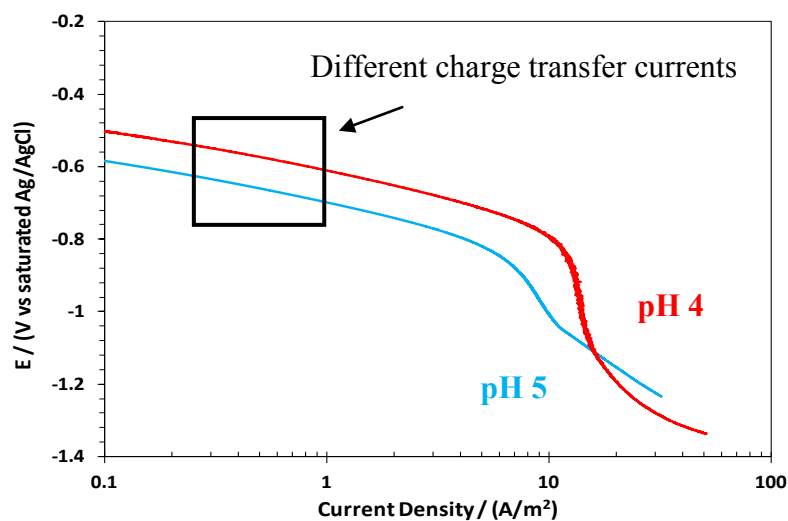


Figure 27: Comparison of charge transfer current on SS304 at different pH, 10 bar $p\text{CO}_2$, 25°C, 3 wt.% NaCl, impeller stirring speed 800 rpm.

Conversely, Figure 28 and Figure 29 show that at a fixed pH, increasing the partial pressure of CO_2 does not affect the charge transfer current. In both cases, although

carbonic acid was the dominant species (H_2CO_3 concentration at 10 bar pCO_2 is equal to 7×10^{-4} M), the direct reduction of carbonic acid cannot be detected. While the charge transfer currents remain the same, the limiting currents increase when CO_2 partial pressure increases due to the ability of carbonic acid to provide additional hydrogen ions when they are consumed by the corrosion reaction at the metal surface.

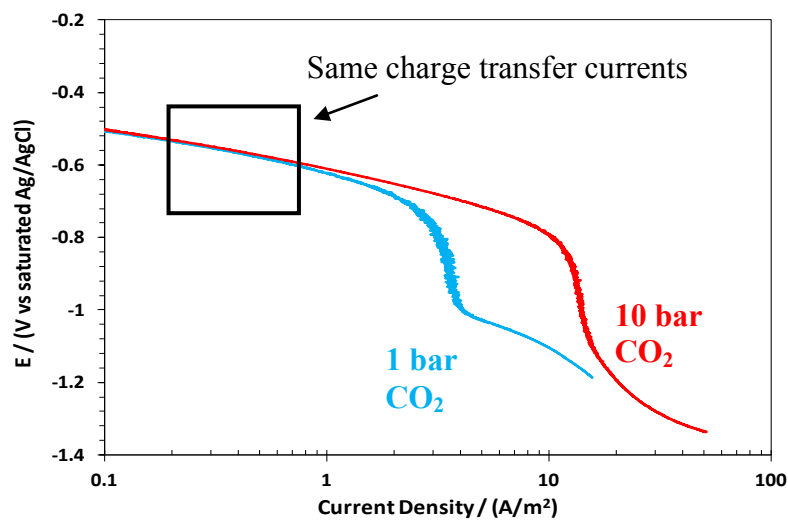


Figure 28: Comparison of charge transfer current on SS304 at different pCO_2 , pH4.0, 25°C, 3 wt.% NaCl, impeller stirring speed 800 rpm.

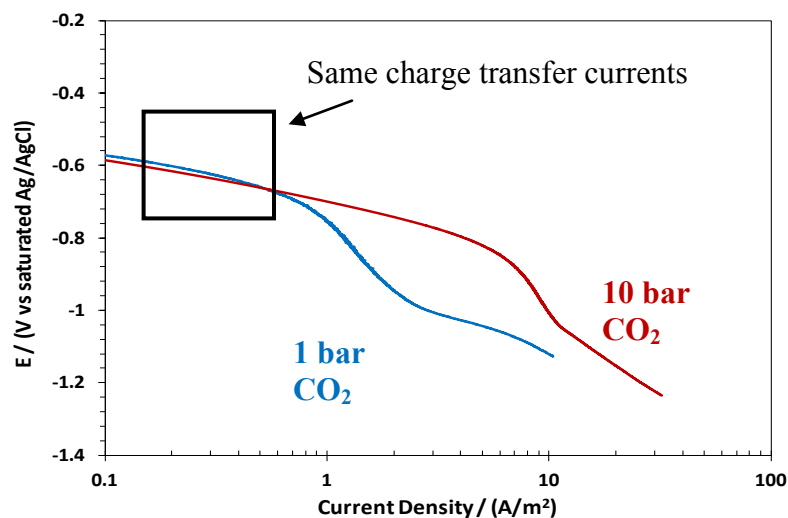


Figure 29: Comparison of charge transfer current on SS304 at different $p\text{CO}_2$, pH5.0, 25°C, 3 wt.% NaCl, impeller stirring speed 800 rpm.

Experiments were also performed at pH6 to minimize the effect of hydrogen ions. First, at 25°C and pH6, the concentration of carbonic acid in the solution is 7×10^{-4} M: about 700 times more than the hydrogen ion concentration (10^{-6} M). Yet, increasing the partial pressure of CO_2 does not influence the charge transfer current (Figure 30). Any direct reduction of carbonic acid would be insignificant at 25°C, pH6.

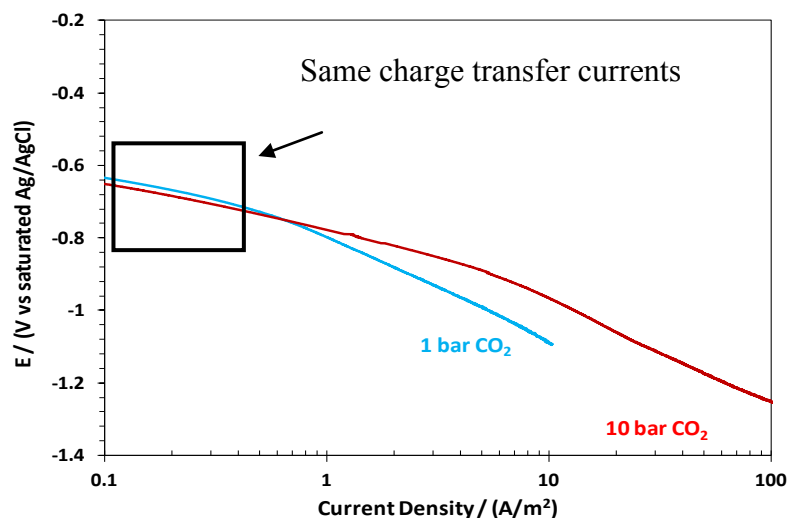


Figure 30: Comparison of charge transfer current on SS304 at different $p\text{CO}_2$, pH6.0, 25°C, 3 wt.% NaCl, impeller stirring speed 800 rpm.

However, the argument here is not only about species that are present in solution at particular concentrations; it is also how fast reactions proceed. Since an increase in temperature accelerates all reactions, the direct reduction of carbonic acid which was possibly slow could be revealed at the higher temperature. Therefore, the temperature was raised to 80°C with the aim of accelerating the direct reduction of carbonic acid so that it could be observed. Of course, the hydrogen ion reduction was also accelerated at 80°C. However, if the hydrogen ion reduction is dominant at 25°C, increasing temperature would have a more pronounced effect on the acceleration of the slower reaction, i.e., the direct reduction of carbonic acid. Figure 31 shows that even at 80°C, the charge transfer current only increases by a factor of two, while the CO₂ partial pressure is increased by a factor of 10. When compared to the overall current that increased by approximately a factor of 10 this suggests that any contribution from the direct reduction

of carbonic acid is still very small. All experiments were repeated and these results are reproducible (see Appendix B for repeated tests).

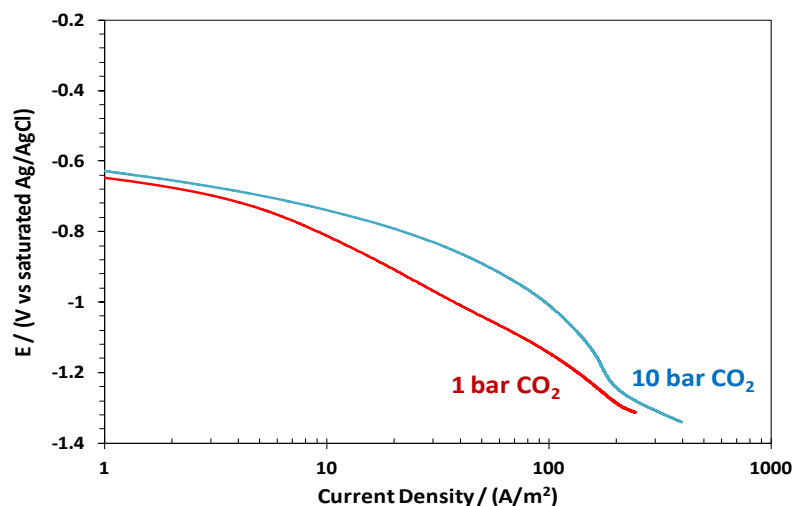


Figure 31: Comparison of charge transfer current on SS304 at different $p\text{CO}_2$, pH 6.0, 80°C , 3 wt.% NaCl, impeller stirring speed 800 rpm.

5.2.2.2 Effect of substrate

The goal of the following experiments was to strengthen the case that the cathodic reaction on stainless steel and mild steel is similar. Since the anodic reaction interferes with the charge transfer current on mild steel, this kind of substrate cannot be used to investigate the charge transfer controlled cathodic reaction. Therefore, a nickel alloy was chosen for comparison.

Nickel alloy is quite different than stainless steel. Table 3 and Table 4 show that the stainless steel 304 has only 10.5 percent of nickel, compared to 99.67 percent of nickel in nickel alloy 200. Although the chemical composition of SS304 and Ni200 is

very different, the obtained cathodic reactions on these materials are very similar. In fact, Figure 32 shows that increasing CO_2 partial pressure does not affect the charge transfer current on the nickel alloy. This behavior was also previously observed on stainless steel. Furthermore, the fact that the charge transfer current on these two materials is very similar in magnitude (Figure 33) suggests that the cathodic reactions on SS304 and Ni200 are very similar. It is fair to assume that the cathodic reactions on SS304 and X65 are also similar since the chemical compositions of SS304 vs. X65 are more similar than the chemical compositions of SS304 and Ni200 (Table 2 - Table 4).

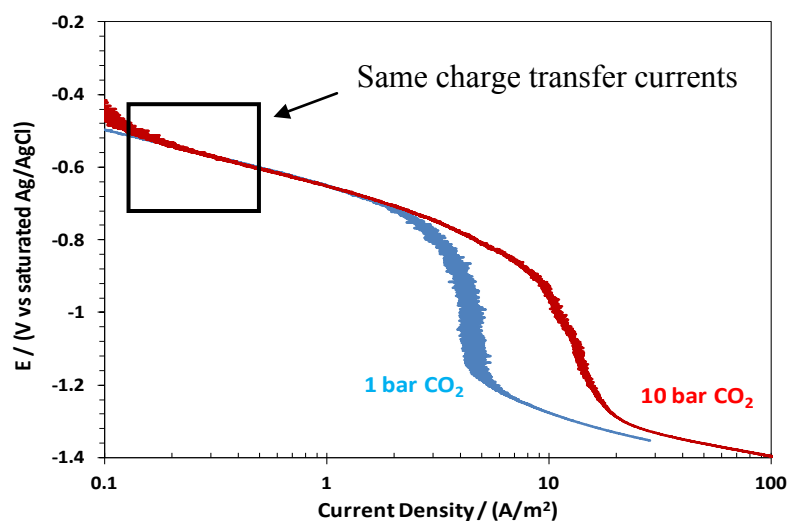


Figure 32: Comparison of charge transfer current on Ni200 at different $p\text{CO}_2$, pH4.0, 25°C, 3 wt.% NaCl, impeller stirring speed 800 rpm.

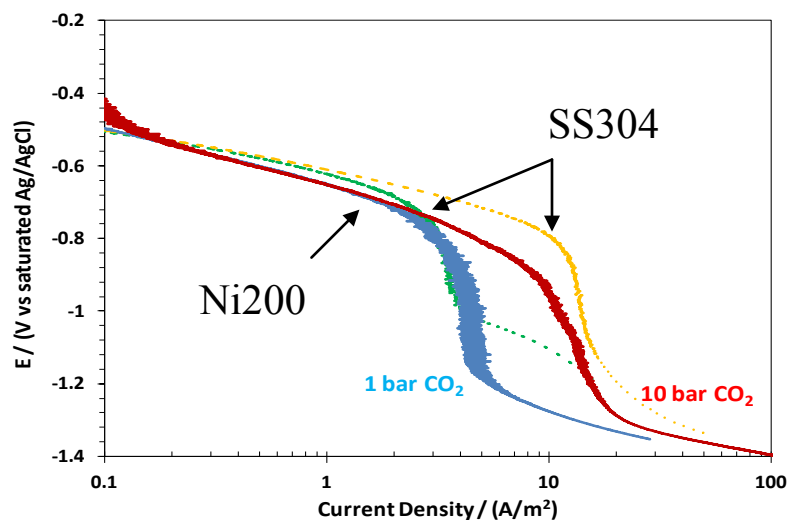


Figure 33: Comparison of charge transfer current on Ni200 vs. SS304, at different $p\text{CO}_2$, pH4.0, 25°C, 3 wt.% NaCl, impeller stirring speed 800 rpm.

5.2.2.3 Use of inhibition

As mentioned, the charge transfer current on mild steel generally could not be observed due to the interference from the anodic reaction. However, when an anodic inhibitor is added to the system, the anodic reaction is retarded more than the cathodic reaction. Therefore, the charge transfer current could be observed on mild steel.

Figure 34 and Figure 35 show the potentiodynamic sweeps on mild steel X65 without CO_2 and with CO_2 . When the inhibitor is not present (Figure 34), the cathodic charge transfer current is “hidden” by the anodic current. In the presence of an anodic inhibitor (Figure 35), at the critical micelle concentration of the chosen alkylbenzyl dimethyl ammonium chloride, both anodic and cathodic reactions were retarded and the cathodic charge transfer current can be observed. From Figure 35, the charge transfer

current is unaffected by the presence of CO_2 . This further implies that the effect of direct reduction of carbonic acid is negligible on mild steel.

By adding an anodic inhibitor, the charge transfer current on mild steel could be observed. Again, the charge transfer current is insensitive to the presence of CO_2 , which supports the buffering effect mechanism.

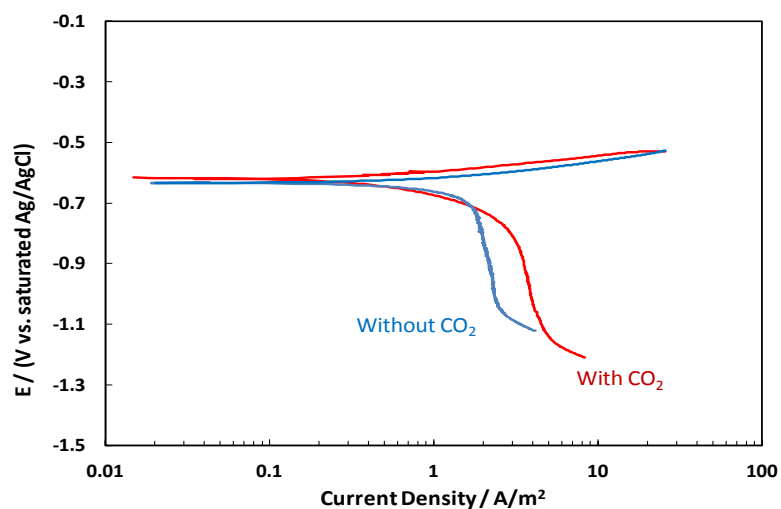


Figure 34: Comparison of charge transfer current on X65 without and with CO_2 at 1 bar total pressure, without inhibitor, 100 ppm H_2S , 25°C, pH4.0, 1 wt.% NaCl, RCE 1000 rpm. Experimental data provided by Juan Dominguez, ICMT.[76]

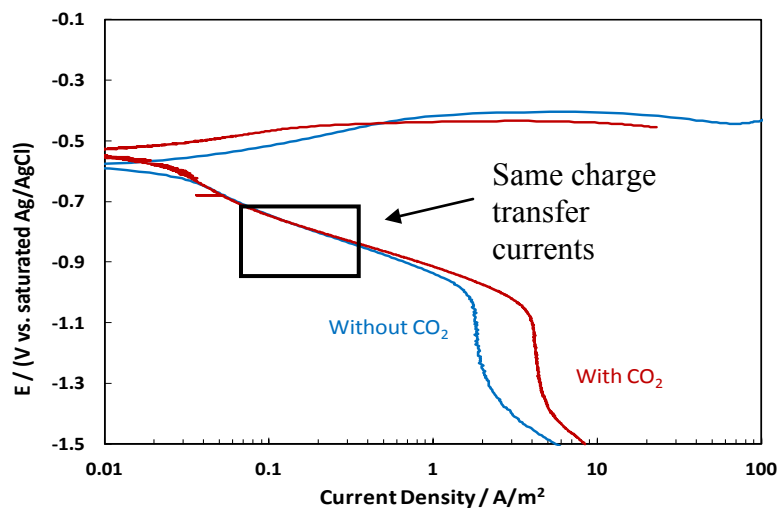


Figure 35: Comparison of charge transfer current on X65 without and with CO₂ at 1 bar total pressure, with inhibitor, 100 ppm H₂S, 25°C, pH4.0, 1 wt.% NaCl, RCE 1000 rpm. Experimental data provided by Juan Dominguez, ICMT.[76]

5.2.3 Conclusions

- The dominant cathodic reaction mechanism related to the reduction of carbonic acid on steel is the buffering effect.
- The presence of carbonic acid only affects the cathodic limiting current due to the ability of carbonic acid to provide hydrogen ions by dissociation, when they are consumed at the metal surface.
- Carbonic acid has no influence on the charge transfer cathodic current since no direct reduction of carbonic acid can be detected. Hydrogen ions are the dominant cathodic reactants reduced at the metal surface. A change of pH leads to a change of the cathodic charge transfer current, as expected.

5.3 Corrosion mechanism of mild steel in other weak acids

The experimental results show that the dominant corrosion mechanism of mild steel in carbonic acid and HAc is the buffering effect. Direct reduction of carbonic acid and HAc do not need to be taken into account in order to describe the cathodic side of the corrosion mechanism of mild steel in solutions of these weak acids. The next question is whether the buffering effect can be applied to all weak acids. The discussion will be based on three other weak acids: formic acid, hydrogen sulfide and water.

5.3.1 Formic acid

Additional experiments were performed on stainless steel in the presence of formic acid (HCOOH) to determine whether the buffering effect still holds for this lower molecular weight weak acid (pKa=3.75 at 25°C). If the direct reduction of HCOOH is insignificant, the buffering effect mechanism for HCOOH, which consists of the dissociation of HCOOH in the bulk (reaction 24), followed by the reduction of adsorbed H⁺ at the steel surface (reactions 13 and 14), is sufficient to explain the corrosion mechanism:



If the direct reduction of HCOOH is important, the following reactions need to be considered in addition to reactions 10, 11, and 21:





The same approach used for HAc and carbonic acid was also used to investigate the corrosion mechanism of mild steel in the presence of formic acid. The experimental procedure is the same as in the HAc work. The test matrix is shown in Table 17.

Table 17: Test matrix to test the effect of HCOOH concentration on the charge transfer current at pH3.

Parameters	Conditions
Equipment	Glass cell
Material	SS304
Temperature (°C)	25 ± 1
Total pressure (bar)	1
CO ₂ partial pressure (bar)	0
pH	3.0 ± 0.1
Formic acid concentration (ppm)	0, 73.6, 736 (±0.6%)
Electrolyte	3 wt. % NaCl
RCE Rotating Speed (rpm)	1000

The results show that increasing free HCOOH concentration does not affect the charge transfer current at pH3 (Figure 36). Only the limiting current is sensitive to the change of HCOOH concentration because HCOOH acts as a reservoir of hydrogen ions via dissociation. Thus, the buffering effect mechanism still holds for formic acid.

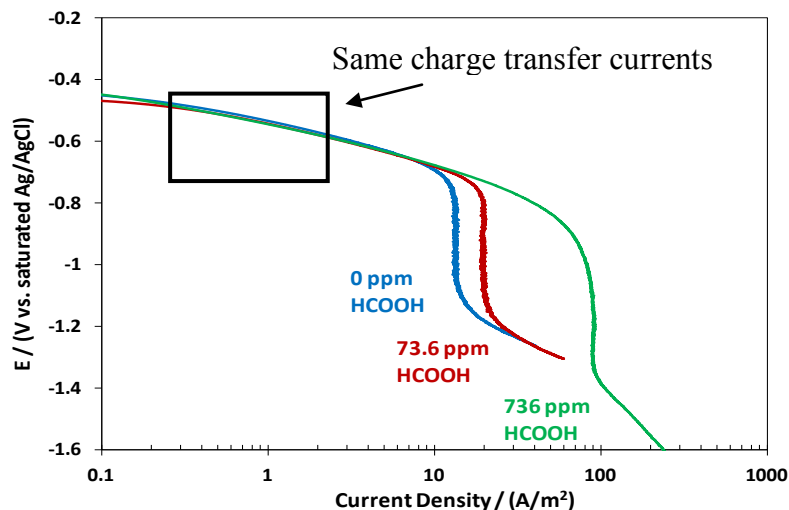


Figure 36: Comparison of charge transfer current on SS304 with different formic acid concentrations, at 1 bar saturated N_2 , $25^\circ C$, pH3.0, 3 wt.% NaCl, 1000 rpm.

5.3.2 Hydrogen sulfide

The corrosion mechanism of mild steel in the presence of hydrogen sulfide (H_2S), which is also a weak acid, has been studied extensively [77-79]. Surprisingly, the H_2S corrosion mechanism is not the same as other weak acids. Zheng et al., observed two waves on the cathodic sweeps, which implied that the direct reduction of H_2S was important [77]. Kittel et al., wrote that the buffering effect was insufficient to explain the cathodic polarization sweeps measured on a 316L rotating disc electrode in the presence of dissolved H_2S [78]. As a result, the authors concluded that the direct reduction of H_2S must be considered.

By using the same method proposed in this research, Zheng's results show an increase of charge transfer current in the presence of 10 percent H_2S in the gas phase

(Figure 37) [80]. This implies that the direct reduction of H_2S needs to be considered.

The H_2S corrosion mechanism in film free condition is proposed as follows:

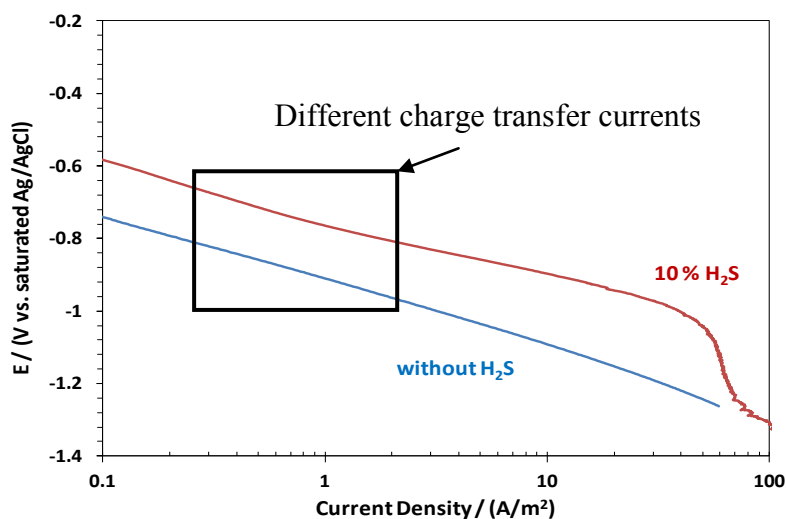


Figure 37: Comparison of charge transfer current on SS316L with different concentration of H_2S , at $30^\circ C$, $pH 6.0$, $1 \text{ wt.}\% \text{ NaCl}$, RCE rotating speed 1000 rpm . Experimental data provided by Yougui Zheng, ICMT. [80]

It is important to note that the results obtained on stainless steel (Figure 37) were consistent with the results obtained on mild steel (Figure 38). An increase of the charge transfer current observed on stainless steel manifests itself as two “waves” in the cathodic polarization curve observed on mild steel in the presence of H_2S . This indicates that the

direct reduction of H_2S is significant on stainless steel as well as mild steel, which further strengthens the concept used here that the same reaction mechanism should be obtained on both steels.

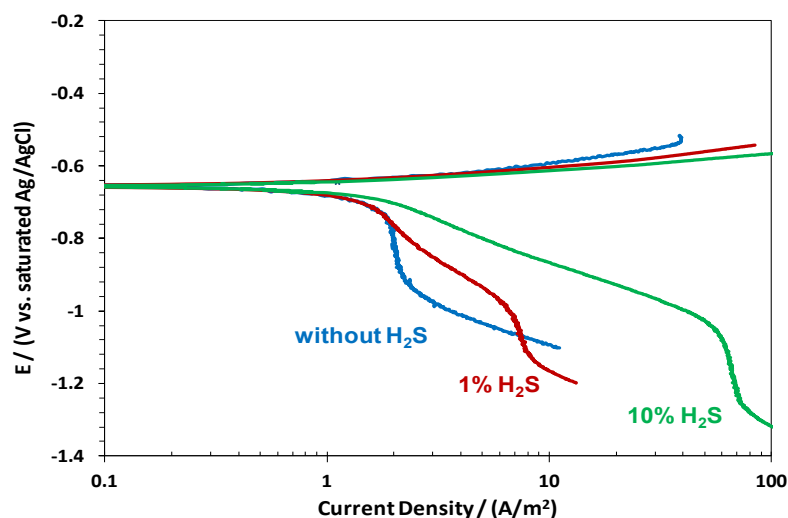


Figure 38: Effect of H_2S on polarization curves on mild steel X65, at $30^\circ C$, pH4.0, RCE rotating speed 1000 rpm, 1 wt.% NaCl. Experimental data taken from Zheng's publication. [77]

The next question that needed an answer is why H_2S behaves differently compared to acetic acid, carbonic acid and formic acid.

The key hypothesis proposed here is that H_2S can be directly reduced at the surface due to its ability to be integrated into the iron lattice without iron dissolution. Figure 39 shows the lattice structure of iron atoms in ferrite in the [100] plane and Figure 40 shows the lattice structure of mackinawite in the [001] plane. The atomic arrangements of Fe atoms in ferrite and in mackinawite have the same geometric alignment as shown in the planes.

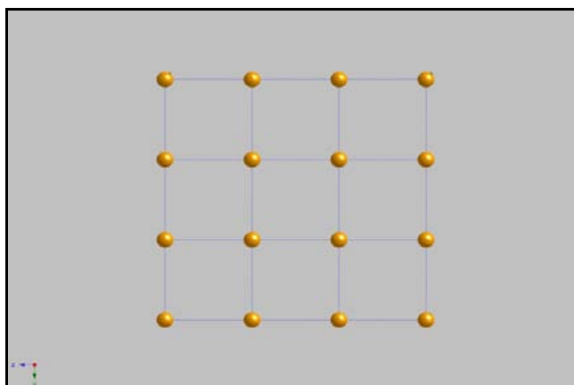


Figure 39: Lattice structure of the Fe atoms in ferrite on the [100] plane. Figure was made by David Young, ICMT, using Crystal Maker™.

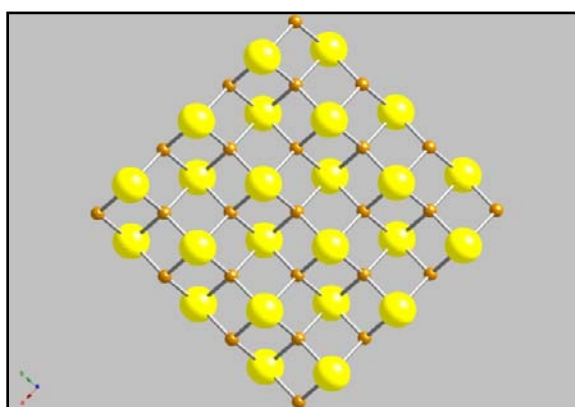


Figure 40: Lattice structure of mackinawite on the [001] plane. S atoms are in yellow. Fe atoms are in orange. Figure was made by David Young, ICMT, using Crystal Maker™.

Indeed, the closest distance between two Fe atoms, parallel to each of xy -, yz -, and xz - planes, in iron is 2.866 Å [81]. In mackinawite, this distance is 2.598 Å [82]. The angles between adjacent Fe atoms within the planes are either 90° or 180°. The significance of this similarity is that the lattice positions of the Fe atoms in ferrite provide an excellent nucleation site for mackinawite growth. In other words, mackinawite can

form when H_2S is adsorbed onto surfaces that correspond to the [100] plane; direct reduction occurs without the need to reorganize the Fe atoms.

Research conducted by Jiang and Carter describes H_2S adsorption and dissociation on the Fe [100] surface [83]. Figure 41 shows the predicted adsorption of H_2S on hollow, bridge and on-top sites. H_2S then breaks one H-S bond by rotating down one H atom toward the Fe surface and dissociates over the Fe atom (Figure 42). As a result, when H_2S is adsorbed to the Fe [100] plane, its direct reaction with the surface forms a single mackinawite layer, with minimal rearrangement of iron atoms. This can also explain the fact that in H_2S corrosion, a very thin layer of mackinawite rapidly forms, which leads to a rapid decrease of corrosion rate. On the other hand, in CO_2 corrosion, the crystalline structure of siderite (Figure 43) with a hexagonal symmetry of Fe atoms has no such topotactic behavior. This may explain why it takes longer to nucleate and grow iron carbonate on an iron surface compared to mackinawite.

In summary, it can be hypothesized that the main reason H_2S can be directly reduced at the surface while the direct reduction of other weak acids is insignificant, is that similarities between the lattice structure of iron atoms in ferrite and in mackinawite facilitate the ability of H_2S to be adsorbed onto the surface, undergoing reduction with subsequent structural integration.

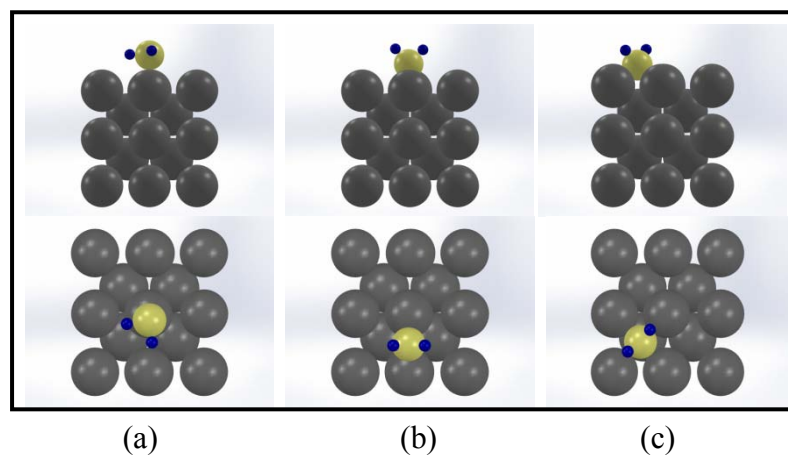


Figure 41: Adsorption sites of H_2S on Fe [100] from side view and top view: (a) on top; (b) bridge; (c) hollow. Fe atoms are in gray. S atoms are in yellow, H atoms are in blue. Images courtesy of Cody Shafer, ICMT. Adapted from [83].

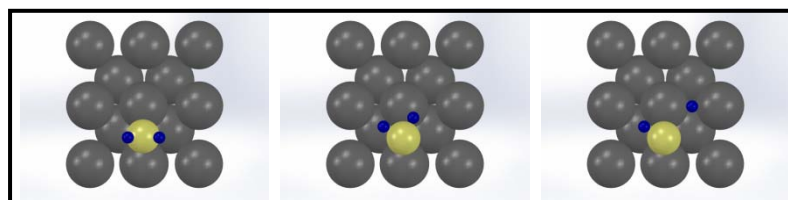


Figure 42: H_2S dissociation on Fe [100] from top view. Fe atoms are in gray. S atoms are in yellow, H atoms are in blue. Images courtesy of Cody Shafer, ICMT. Adapted from [83].

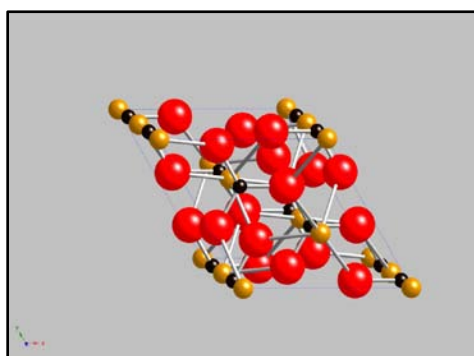


Figure 43: Crystal structure of siderite. Fe atoms are in orange. C atoms are in black, O atoms are in red. Figure was made by David Young, ICMT, using Crystal MakerTM.

Moreover, weak acids such as carbonic acid, acetic acid, and formic acid have a more complicated molecular structure (Figure 44). It is harder for these molecules to integrate to the iron lattice without iron dissolution. As a result, the question is not one of weak acids, but of how complicated the acid's molecular structure is. An acid with simple structure like H_2S is expected to have a direct reaction. Carbonic acid, acetic acid, and formic acid all belong to the aqueous carboxylic acid group. Hence, the buffering effect mechanism applies generally to aqueous carboxylic acids.

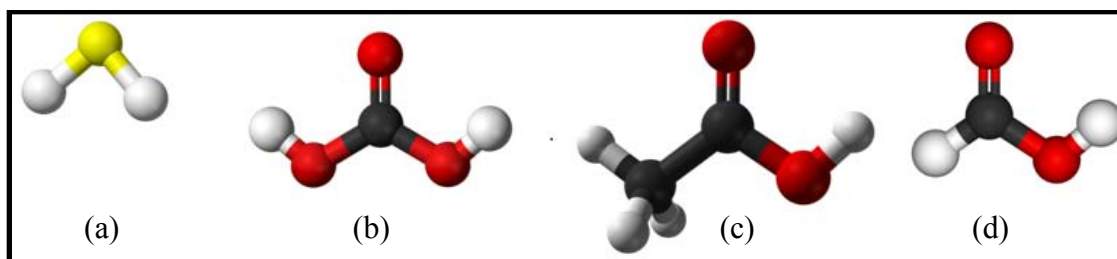
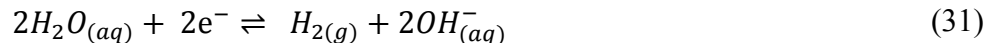


Figure 44: Molecular structure of (a) hydrogen sulfide (H_2S); (b) carbonic acid (H_2CO_3); (c) acetic acid (CH_3COOH); (d) formic acid ($HCOOH$). H atom is in white. S atom is in yellow. C atom is in black. O atom is in red. Picture sources: <http://commons.wikimedia.org/wiki>

5.3.3 Water

If the hydrogen ion reduction reaction (5) is combined with the water dissociation reaction (30), the direct water reduction reaction (31) is obtained, which is thermodynamically equivalent to reaction (5).





In all experiments presented in this work, the direct reduction of H₂O appears at a very negative potential (about -1.1 V vs. saturated Ag/AgCl) and occurs at a much slower rate compared to the reduction of H⁺.

Water is another example of a weak acid for which the buffering effect is not sufficient to describe the corrosion mechanism. The explanation proposed above for the H₂S direct reduction is based on the simplicity of the H₂S molecular structure. It can also be used to explain the direct reduction of H₂O based on similar structural simplicity. It is easier for weak acids with simpler molecular configurations such as H₂S or H₂O, to be directly reduced at the steel surface. The direct reduction of weak acids that have more complicated molecular configurations, such as acetic acid, carbonic acid, and formic acid (i.e., aqueous carboxylic acids) can be ignored.

CHAPTER 6: ELECTROCHEMICAL CORROSION MODEL PREDICTION

6.1 Introduction

Based on the prevailing understanding of corrosion mechanisms at the time, a large number of well done models have been developed to predict the corrosion rates of mild steel in aqueous environments containing aggressive species such as CO_2 and HAc. Important factors such as temperature, pressure, flow velocity, etc., have been studied and included in the corrosion models. In a large number of publications, direct reduction processes for carbonic acid and HAc have been commonly assumed in model theories. Some models are inaccessible to the public, while others, such as FREECORP, developed by the Institute for Corrosion and Multiphase Technology at the Ohio University, is an open literature source. This mechanistic model provides internal uniform corrosion prediction of mild steel pipelines for a wide range of conditions. Theoretical potentiodynamic sweeps can also be generated, which helps to understand the corrosion mechanisms. Like other models, the direct reductions of carbonic acid and HAc have been assumed to hold in FREECORP. However, the present work proves that these reactions are insignificant, at least up to 10 bar CO_2 . As a result, modifications to the FREECORP model are needed to account for the buffering effect mechanism.

In the following section, the theory used in FREECORP is reviewed with the focus on carbonic acid and HAc in film-free condition. Details relating to other cathodic species such as oxygen (O_2) and hydrogen sulfide (H_2S) are provided in the original publication by Netic et al., relating to development of this mechanistic model [20]. The FREECORP model is also called, in this chapter, the *direct reduction model*, and needs to

be distinguished from the *buffering effect model* that is a part of the new modified version of FREECORP, where direct reductions of carbonic acid and acetic acid are disabled. Both models are then compared with experimental results, obtained not only by the author of this work, but also with data from other researchers.

6.2 Theory of FREECORP – direct reduction model

6.2.1 Chemical reactions

Chemical reactions related to CO₂ and HAc corrosion are shown in Table 18. Other species that also are accounted for in FREECORP such as hydrogen sulfide, and oxygen are outside the scope of this work.

Table 18: Chemical reactions related to CO₂ and HAc corrosion.

Process	Reactions	
Dissolution of carbon dioxide	$CO_{2(g)} \rightleftharpoons CO_{2(aq)}$	(1)
Hydration of carbon dioxide	$CO_{2(aq)} + H_2O_{(l)} \rightleftharpoons H_2CO_{3(aq)}$	(2)
Dissociation of carbonic acid	$H_2CO_{3(aq)} \rightleftharpoons H^+_{(aq)} + HCO_3^-_{(aq)}$	(3)
Dissociation of bicarbonate	$HCO_3^-_{(aq)} \rightleftharpoons H^+_{(aq)} + CO_3^{2-}_{(aq)}$	(4)
Dissociation of acetic acid	$HAC_{(aq)} \rightleftharpoons H^+_{(aq)} + Ac^-_{(aq)}$	(17)
Dissociation of water	$H_2O_{(aq)} \rightleftharpoons H^+_{(aq)} + OH^-_{(aq)}$	(30)

In CO₂ corrosion, the corrosion process is controlled by the CO₂ hydration reaction rate (reaction 2), which proceeds at a slower rate than the dissociation reaction of

H₂CO₃ and HCO₃⁻ as well as other pertinent processes. Stronger than carbonic acid (pKa 4.76 vs. 6.35 at 25°C), HAc is the main source of hydrogen ions when the concentration of each acid is the same. The dissociation of HAc is also very fast as compared to other processes.

6.2.2 Electrochemical reactions

6.2.2.1 Anodic reaction

The dominant anodic reaction is iron dissolution (reaction 8).



Due to the participation of hydrogen ions in the multi-step mechanism proposed by Bockris, the total reaction (8) is affected by pH [35]. However, the dependency on pH usually diminishes when pH > 4. For practical purposes, the effect of pH on the iron dissolution was ignored in the FREECORP direct reduction model. At the corrosion potential, the anodic dissolution of iron is charge transfer controlled and can be calculated as follows [20]:

$$i_a = i_{0(Fe)} \times 10^{\frac{E_{corr} - E_{rev,Fe}}{b_a}} \quad (32)$$

Where:

i_a : current density of iron oxidation or anodic current density (A/m²);

$i_{0(Fe)}$: exchange current density of iron oxidation (A/m²);

E_{corr} : corrosion potential (V);

$E_{rev,Fe}$: reversible potential of iron oxidation (V);

b_a : Tafel slope of iron oxidation (V/dec).

6.2.2.2 Cathodic reactions

While the only dominant anodic reaction is the iron dissolution, several cathodic reactions can occur in the corrosion process, depending on the number of cathodic species present in the environment. In the direct reduction model, the following cathodic reactions related to CO₂ and HAc corrosion are considered:

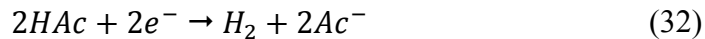
Reduction of hydrogen ions:



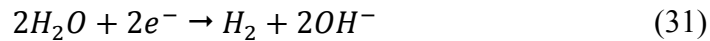
Reduction of carbonic acid:



Reduction of acetic acid:



Reduction of water:



For each of these cathodic reactions, the cathodic current density i_c is obtained based on the charge transfer current density i_{ct} and the limiting current density i_{lim} (with the exception of water reduction which is always under charge transfer control due to an unlimited quantity of water molecules in the solution) [20]:

$$\frac{1}{i_c} = \frac{1}{i_{ct}} + \frac{1}{i_{lim}} \quad (33)$$

The charge transfer current density of cathodic reactions is a function of potential:

$$i_{ct} = i_0 \times 10^{-\frac{E_{corr} - E_{rev}}{b_c}} \quad (34)$$

Where:

i_{ct} : current density of cathodic reactions (A/m^2);

i_0 : exchange current density of cathodic reactions (A/m^2);

E_{corr} : corrosion potential (V);

E_{rev} : reversible potential of cathodic reactions (V);

b_c : Tafel slope of cathodic reactions (V/dec).

The limiting current arising from the diffusion of hydrogen ions to the metal surface, $i_{lim(H^+)}^d$, can be written as:

$$i_{lim(H^+)}^d = k_m F [H^+]_b \quad (35)$$

Where:

F : Faraday constant (C/mol);

$[H^+]_b$: concentration of hydrogen ions in the bulk (mol/l);

k_m : mass transfer coefficient (m/s).

The mass transfer coefficient k_m for an RCE can be determined from the correlation outlined by Eisenberg et al. [74]:

$$Sh = \frac{k_m d}{D_{H^+}} = 0.0791 \times Re^{0.7} \times Sc^{0.356} \quad (36)$$

Where:

D_{H^+} : diffusion coefficient for H^+ ions (m^2/s);

d : specimen diameter (m);

Re : Reynolds number;

Sc : Schmitt number.

In the presence of HAc, the limiting current arising from diffusion of HAc to the metal surface, can be calculated in a similar fashion, from the HAc bulk concentration, $[\text{HAc}]_b$, and the mass transfer coefficient, k_m :

$$i_{lim(\text{HAc})}^d = k_m F [\text{HAc}]_b \quad (37)$$

On the other hand, the chemical reaction limiting current, occurring due to the slow hydration of CO_2 , can be obtained as shown in equation (38):

$$i_{lim(\text{H}_2\text{CO}_3)}^r = F \times [\text{CO}_2]_b \times (D_{\text{H}_2\text{CO}_3} K_{hyd} k_{hyd}^f)^{0.5} f \quad (38)$$

Where:

F : Faraday constant (C/mol);

$[\text{CO}_2]_b$: bulk concentration of dissolved CO_2 (mol/l);

$D_{\text{H}_2\text{CO}_3}$: diffusion coefficient for carbonic acid (m^2/s);

K_{hyd} : equilibrium constant for the CO_2 hydration reaction;

k_{hyd}^f : forward reaction rate constant for the CO_2 hydration reaction (s^{-1});

f : flow factor.

This equation was first derived by Vetter for a slow chemical reaction followed by a fast electrochemical reaction in stagnant condition [84]. An additional factor was then added to include the effect of flow [20]. This factor can be estimated based on δ_m and δ_r , which are the mass transfer and reaction layer thickness, respectively:

$$f = \frac{1 + e^{-2\delta_m/\delta_r}}{1 - e^{-2\delta_m/\delta_r}} \quad (39)$$

Where:

$$\delta_m = \frac{D_{H_2CO_3}}{k_{m,H_2CO_3}} \quad (40)$$

$$\delta_r = \sqrt{\frac{D_{H_2CO_3} \times K_{hyd}}{k_{hyd}^f}} \quad (41)$$

The corrosion potential E_{corr} can be calculated based on the charge balance at the steel surface:

$$\sum_1^{n_a} i_a = \sum_1^{n_c} i_c \quad (42)$$

Where:

i_a, i_c : anodic and cathodic current density, respectively (A/m^2);

n_a, n_c : number of anodic and cathodic reactions, respectively (A/m^2);

In this case $n_a = 1$, as the dominant anodic reaction is the iron dissolution. Once the corrosion potential is computed, the anodic current density can be found by equation (32), and the corrosion rate can finally be calculated:

$$CR = \frac{i_a \times M_{w,Fe}}{\rho_{Fe} \times n \times F} \quad (43)$$

Where:

CR : corrosion rate (mm/y);

i_a : anodic current density (A/m^2);

$M_{w,Fe}$: molecular weight of iron (g/mol);

ρ_{Fe} : density of iron (kg/m^3);

n : number of electrons involved in iron oxidation.

6.3 Theory of modified FREECORP–buffering effect model

6.3.1 Cathodic reaction

The main difference between the old FREECORP–direct reduction model and the new modified FREECORP–buffering effect model is that, in the latter, the direct reduction processes of carbonic acid and HAc are not taken into account.

By removing the direct reduction of carbonic acid and HAc, the total cathodic current density is the sum of the current density arising from the reduction of hydrogen ions and from water reduction:

$$i_c = i_{c(H^+)} + i_{c(H_2O)} \quad (44)$$

The cathodic current density for water reduction, $i_{c(H_2O)}$, which is under charge transfer control, is calculated in the same way as in the direct reduction model.

The cathodic current density for hydrogen ion reduction, $i_{c(H^+)}$, is calculated with the charge transfer current and the limiting current, as shown in equation (33). While the charge transfer current is a function of pH, the limiting current changes according to pH, HAc and H_2CO_3 concentration:

$$\frac{1}{i_{c(H^+)}} = \frac{1}{i_{ct(H^+)}} + \frac{1}{i_{lim(H^+)}^d + i_{lim(HAc)}^d + i_{lim(H_2CO_3)}^r} \quad (45)$$

Where $i_{ct(H^+)}$ and $i_{lim(H^+)}^d$ are determined by equations 34 - 35, respectively.

In determining the equation to calculate the limiting currents in the presence of HAc related to the buffering effect mechanism, the increase of available H^+ at the steel surface from the HAc dissociation must be accounted for. However, since H^+ is the dominant reduced species, its concentration at the steel surface equals to zero. At the

same time, the dissociation of HAc to provide H^+ is very fast [19]. As a result, the concentrations of HAc will also be zero at the steel surface, which is essentially the same as if HAc were directly reduced. However, it should be reiterated that HAc concentration at the steel surface is zero because of the buffering effect, and not direct reduction; a similar argument can be made for H_2CO_3 . Therefore, the equations 37 and 38, which were used to calculate the limiting current for HAc and H_2CO_3 for the direct reduction model, can also be used in the case of the buffering effect.

6.3.2 Anodic reaction

For the anodic reaction, the current density can be obtained as:

$$i_a = i_{0(Fe)} \times 10^{\frac{E_{corr} - E_{rev,Fe}}{b_a}} \quad (32)$$

Where:

i_a : current density of iron oxidation or anodic current density (A/m^2);

$i_{0(Fe)}$: exchange current density of iron oxidation (A/m^2);

E_{corr} : corrosion potential (V);

$E_{rev,Fe}$: reversible potential of iron oxidation (V);

b_a : Tafel slope of iron oxidation (V/dec).

While the effect of pH on the anodic reaction rate was ignored in the direct reduction model, it was included in the buffering effect model to improve the predictions.

The values for the constants used in the buffering effect model to calculate the exchange current densities are summarized in Table 19.

Table 19: Exchange current density calculation $i_0 = i_{oref} \left(\frac{c_{H^+}}{c_{H^+ref}} \right)^{a_1} \exp \left(\frac{-\Delta H}{R} \left(\frac{1}{T} - \frac{1}{T_{ref}} \right) \right)$

Reactions	i_{oref} (A/m ²)	a_1	C_{H^+ref} (mol/l)	ΔH (kJ/mol)	Tafel slope (V/dec)
$2H^+ + 2e^- \rightarrow H_2$	0.2	0	10^{-4}	30	$\frac{2.303RT}{0.5F}$
$2H_2O + 2e^- \rightarrow H_2 + 2OH^-$	0.0001 if $pCO_2 > 0$, 0.00003 if $pCO_2 = 0$	-0.5	10^{-4}	30	$\frac{2.303RT}{0.5F}$
$Fe \rightarrow Fe^{2+} + 2e^-$	1.5×10^{-4}	-0.5	10^{-4}	50	$\frac{2.303RT}{0.74F}$

6.4 Comparison between the models and experimental data

Figure 45 - Figure 48 compares experimental and predicted sweeps at different bulk pH, first without CO₂ (Figure 45 and Figure 46), and then in the presence of one bar pCO₂ (Figure 47 and Figure 48). In the direct reduction model, the anodic reaction does not depend on pH, resulting in a discrepancy of experimental and predicted anodic curves, especially at low pH. The effect of pH on the anodic reaction was included in the buffering effect model, resulting in a better agreement of the anodic sweeps. Both models are able to predict an increase of limiting current when pH decreases.

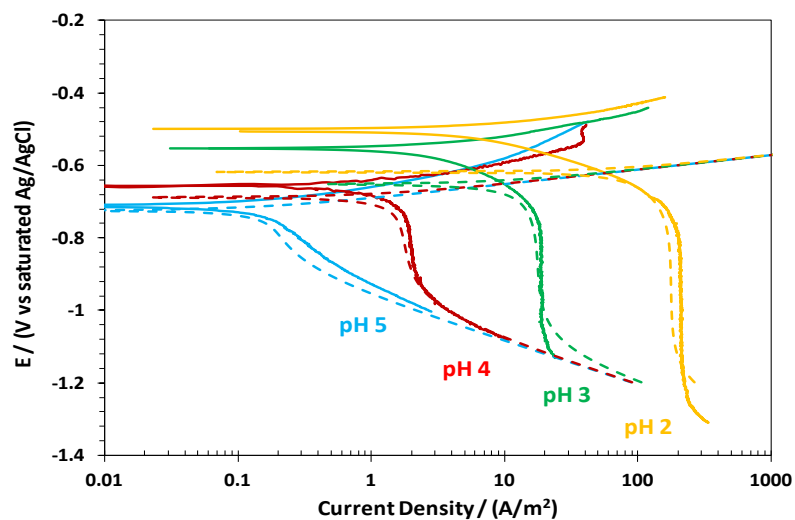


Figure 45: Comparison between experimental (solid lines) and predicted sweeps (dashed lines) at 30°C, 1 bar total pressure, saturated N₂ solution, RCE 1000 rpm, X65. FREECORP-direct reduction model was used. Experimental data provided by Yougui Zheng, ICMT. [77]

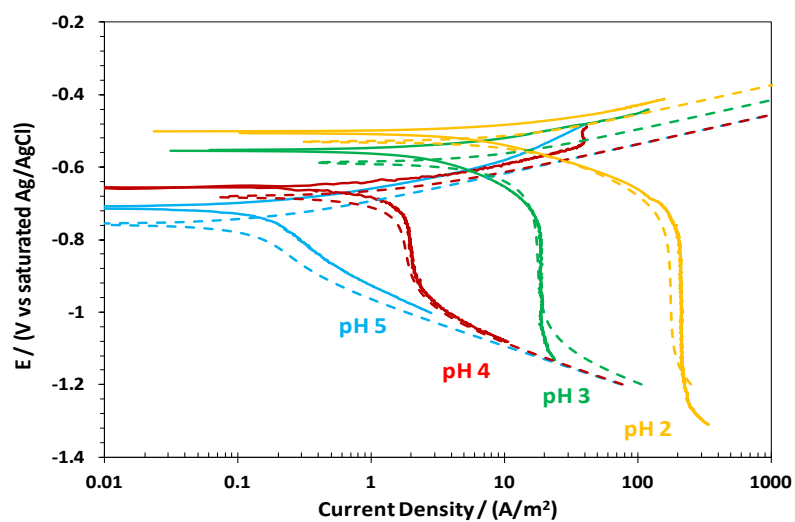


Figure 46: Comparison between experimental (solid lines) and predicted sweeps (dashed lines) at 30°C, 1 bar total pressure, saturated N₂ solution, RCE 1000 rpm, X65. FREECORP-buffering effect model was used. Experimental data provided by Yougui Zheng, ICMT. [77]

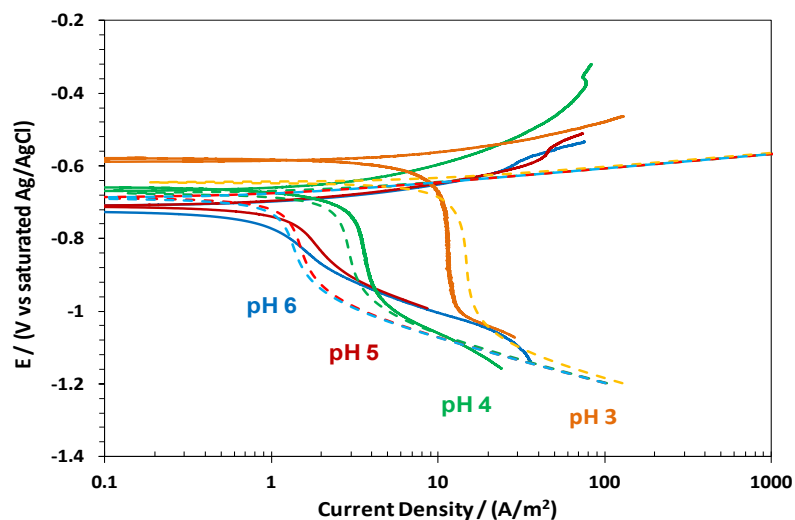


Figure 47: Comparison between experimental (solid lines) and predicted sweeps (dashed lines) at 25°C, 1 bar pCO₂, RCE 1000 rpm, 3 wt.% NaCl, X65. FREECORP-direct reduction model was used.

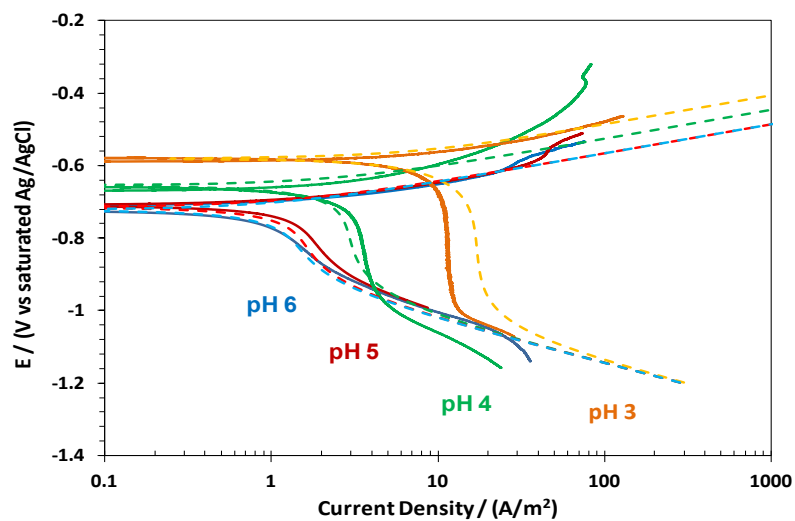


Figure 48: Comparison between experimental (solid lines) and predicted sweeps (dashed lines) at 25°C, 1 bar pCO₂, RCE 1000 rpm, 3 wt.% NaCl, X65. FREECORP-buffering effect model was used.

Figure 49 - Figure 54 compares experimental and predicted sweeps at different partial pressures of CO₂ at pH4 (Figure 49 and Figure 50), pH5 (Figure 51 and Figure 52), and pH6 (Figure 53 and Figure 54). From the experiments, the anodic reactions seemed unaffected when CO₂ partial pressure increased from 1 bar to 10 bars. Both models agree with the experimental data at these conditions, except at pH6 in the direct reduction model, where the cathodic reaction is overpredicted at 10 bar CO₂.

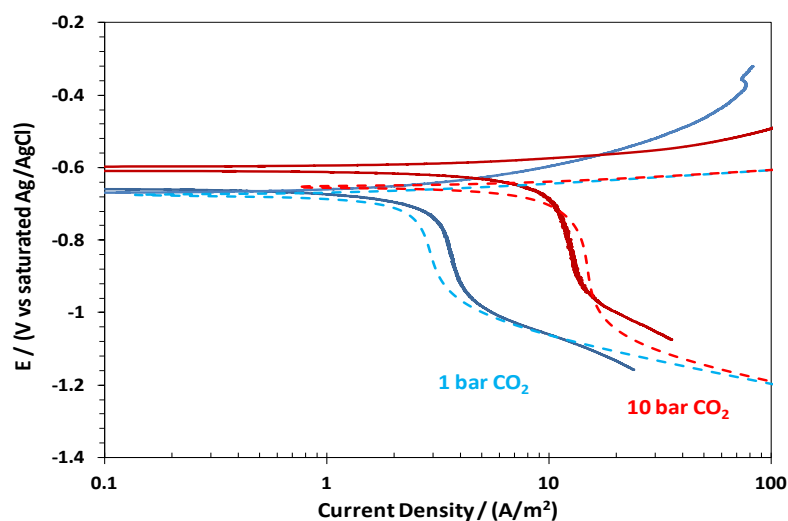


Figure 49: Comparison between experimental (solid lines) and predicted sweeps (dashed lines) at 25°C, pH4.0, 0.5 m/s, 3 wt.% NaCl, X65. FREECORP-direct reduction model was used.

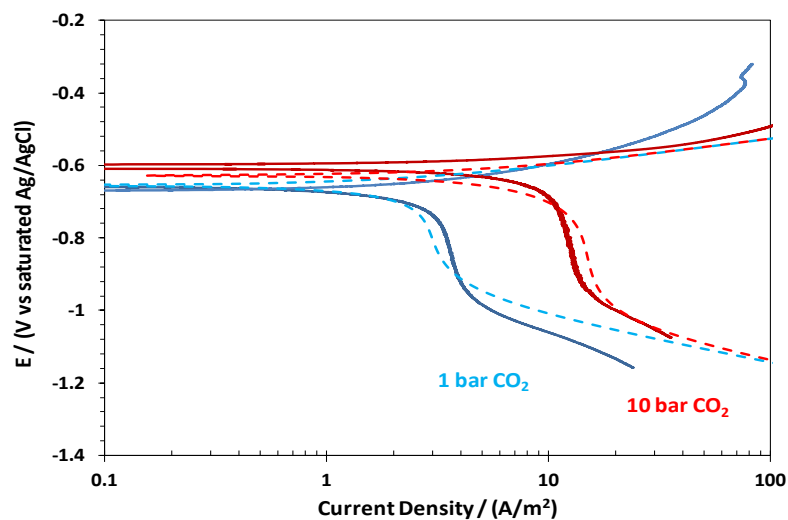


Figure 50: Comparison between experimental (solid lines) and predicted sweeps (dashed lines) at 25°C, pH4.0, 0.5 m/s, 3 wt.% NaCl, X65. FREECORP-buffering effect model was used.

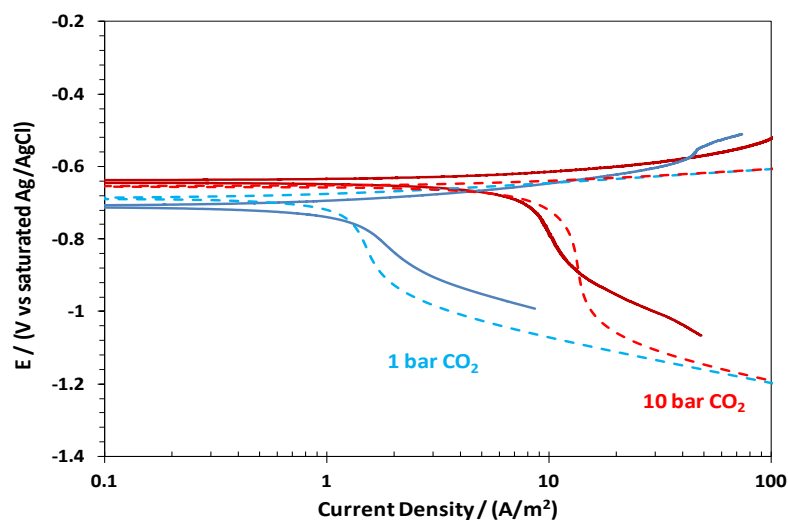


Figure 51: Comparison between experimental (solid lines) and predicted sweeps (dashed lines) at 25°C, pH5.0, 0.5 m/s, 3 wt.% NaCl, X65. FREECORP-direct reduction model was used.

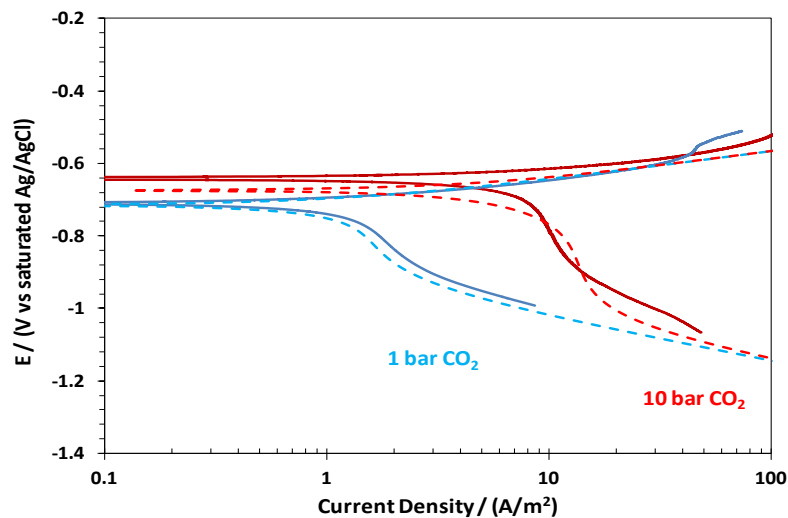


Figure 52: Comparison between experimental (solid lines) and predicted sweeps (dashed lines) at 25°C, pH5.0, 0.5 m/s, 3 wt.% NaCl, X65. FREECORP-buffering effect model was used.

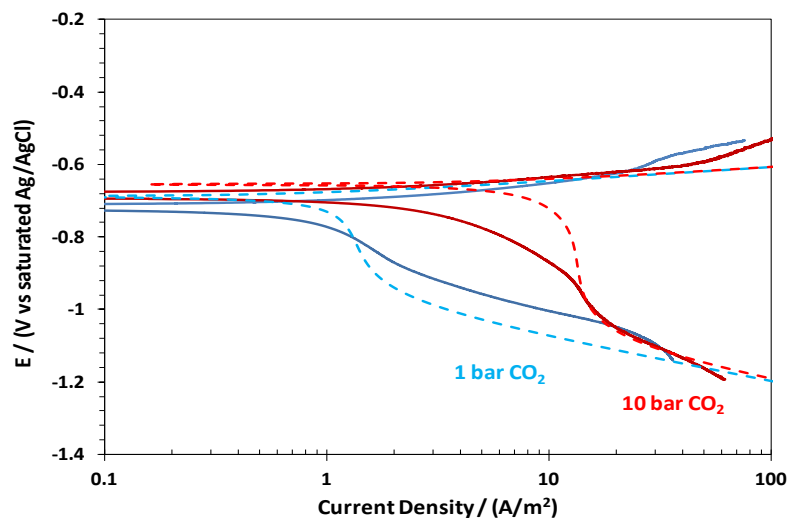


Figure 53: Comparison between experimental (solid lines) and predicted sweeps (dashed lines) at 25°C, pH6.0, 0.5 m/s, 3 wt.% NaCl, X65. FREECORP-direct reduction model was used.

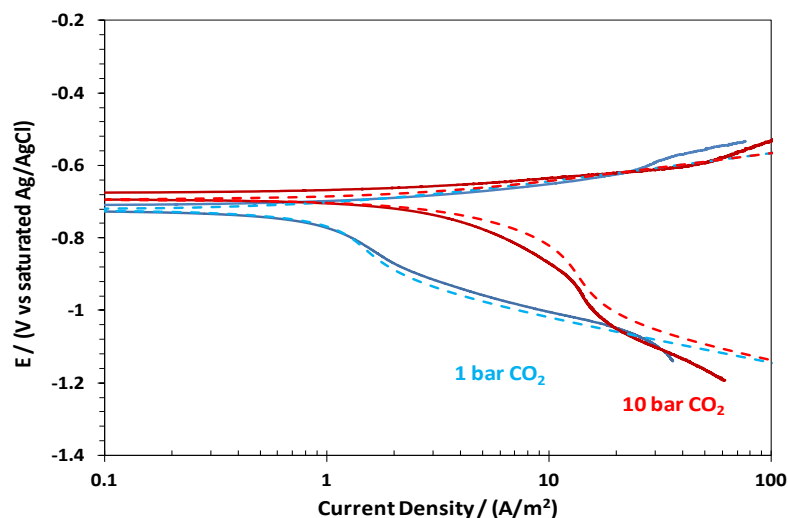


Figure 54: Comparison between experimental (solid lines) and predicted sweeps (dashed lines) at 25°C, pH6.0, 0.5 m/s, 3 wt.% NaCl, X65. FREECORP-buffering effect model was used.

Agreement between the predicted cathodic sweeps and the experiments was found in the presence of HAc (Figure 55 and Figure 56). The buffering effect model provides a better match for the anodic curves. Table 20 – Table 22 compare the calculated and measured limiting currents as a function of HAc concentration at pH4, and pH3 at 25°C, and pH4 at 80°C in the case of a RCE. The calculated limiting currents matched the measured limiting currents, which is consistent with George’s work [58].

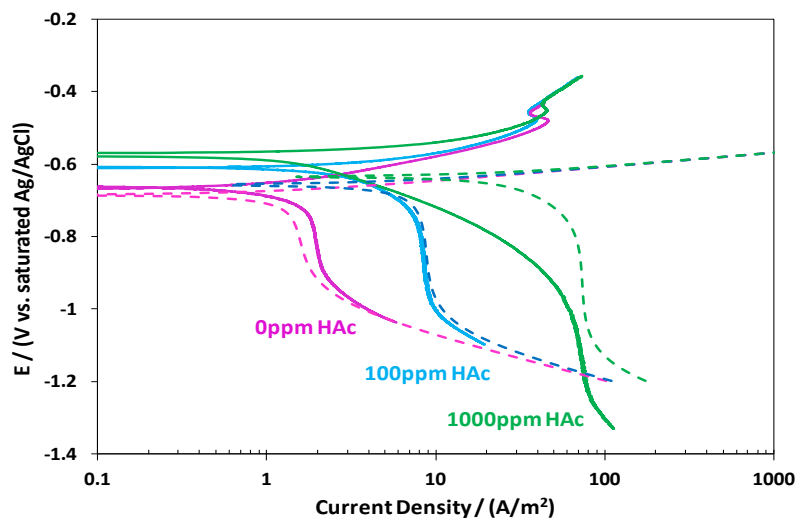


Figure 55: Comparison between experimental (solid lines) and predicted sweeps (dashed lines) at 25°C, pH4.0, 1 bar total pressure, saturated N₂ solution, 3 wt.% NaCl, RCE 1000 rpm, X65. FREECORP-direct reduction model was used.

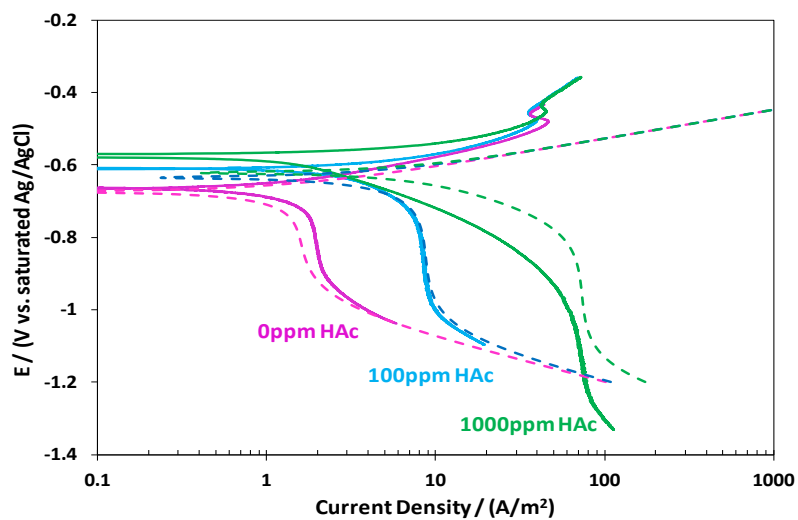


Figure 56: Comparison between experimental (solid lines) and predicted sweeps (dashed lines) at 25°C, pH4.0, 1 bar total pressure, saturated N₂ solution, 3 wt.% NaCl, RCE 1000rpm, X65. FREECORP-buffering effect model was used.

Table 20: Comparison between calculated and measured limiting currents at pH4.0, 25°C, 3 wt.% NaCl, RCE 1000 rpm.

HAc concentration (ppm)	i_{lim} calculated (A/m ²)	i_{lim} measured (A/m ²)
0	1.7	2 ± 10%
100	8.9	8.4 ± 10%
1000	73	71 ± 10%

Table 21: Comparison between calculated and measured limiting currents at pH3.0, 25°C, 3 wt.% NaCl, RCE 1000 rpm.

HAc concentration (ppm)	i_{lim} calculated (A/m ²)	i_{lim} measured (A/m ²)
0	17	14 ± 10%
100	22	19 ± 10%
1000	90	80 ± 10%

Table 22: Comparison between calculated and measured limiting currents at pH4.0, 80°C, 3 wt.% NaCl, RCE 1000 rpm.

HAc concentration (ppm)	i_{lim} calculated (A/m ²)	i_{lim} measured (A/m ²)
0	4.2	5.4 ± 10%
100	23	22 ± 10%
1000	200	194

The predicted corrosion rates were compared with the experimental data from many different sources. Without CO₂, the buffering effect model provides better corrosion rate prediction at low pH (Figure 57), because in the direct reduction model, the effect of pH on the anodic reaction was not included. At one bar pCO₂, both models provide accurate predictions (Figure 58). At 10 bar pCO₂, the buffering effect model is

still able to predict high corrosion rates (Figure 59 – Figure 61) without assuming the direct reduction of carbonic acid. At higher CO_2 partial pressure and higher temperatures, the direct reduction model over-predicts the corrosion rates (Figure 62 – Figure 64). At these conditions, the buffering effect model was able to provide a reasonable corrosion rate prediction.

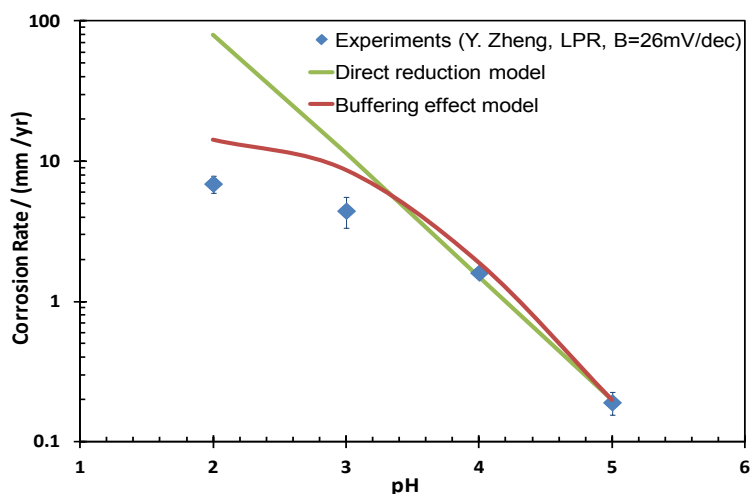


Figure 57: Comparison between experimental and predicted corrosion rates at 30°C, 1 bar total pressure, saturated N_2 solution, RCE 1000 rpm, 1 wt.% NaCl X65. Error bars represent standard deviation of the experimental values. Experimental data provided by Yougui Zheng, ICMT. [77]

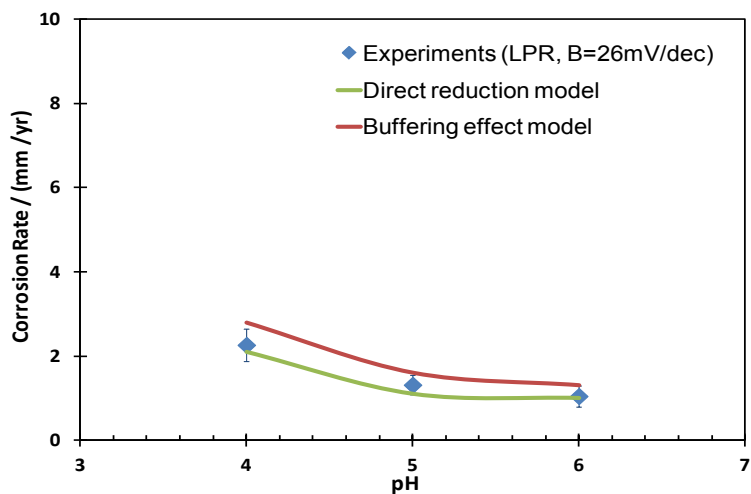


Figure 58: Comparison between experimental and predicted corrosion rates at 25°C, 1 bar pCO₂, RCE 1000 rpm, 3 wt.% NaCl, X65. Error bars represent standard deviation of the experimental values.

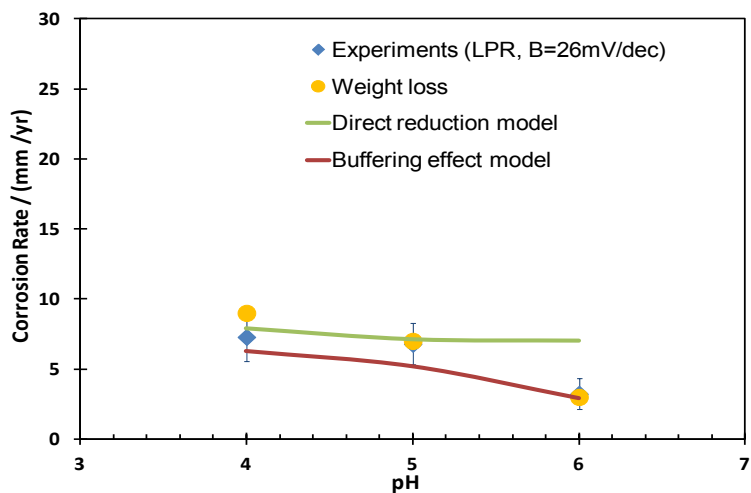


Figure 59: Comparison between experimental and predicted corrosion rates at 25°C, 10 bar pCO₂, 0.5 m/s, 3 wt.% NaCl, X65. Error bars represent standard deviation of the experimental values.

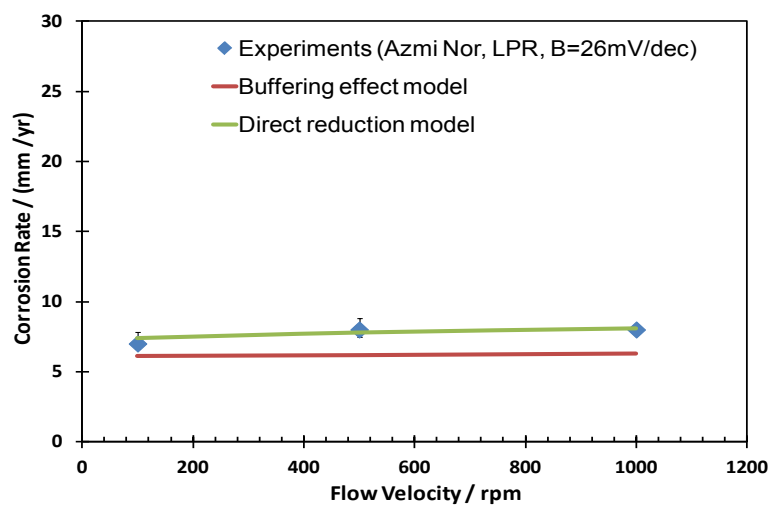


Figure 60: Comparison between experimental and predicted corrosion rates at 25°C, pH4.2, 10 bar pCO₂, 1 wt.% NaCl, X65. Experimental data taken from Nor's publication. [42]

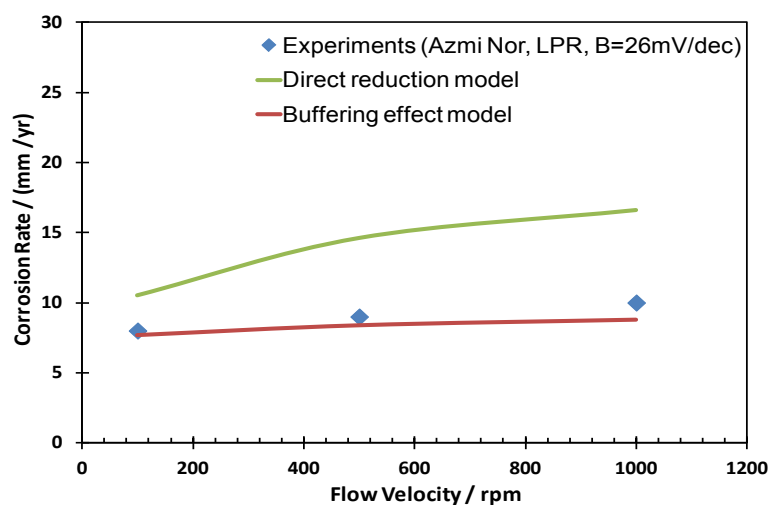


Figure 61: Comparison between experimental and predicted corrosion rates at 25°C, pH3.0, 10 bar pCO₂, 1 wt.% NaCl, X65. Experimental data taken from Nor's publication. [42]

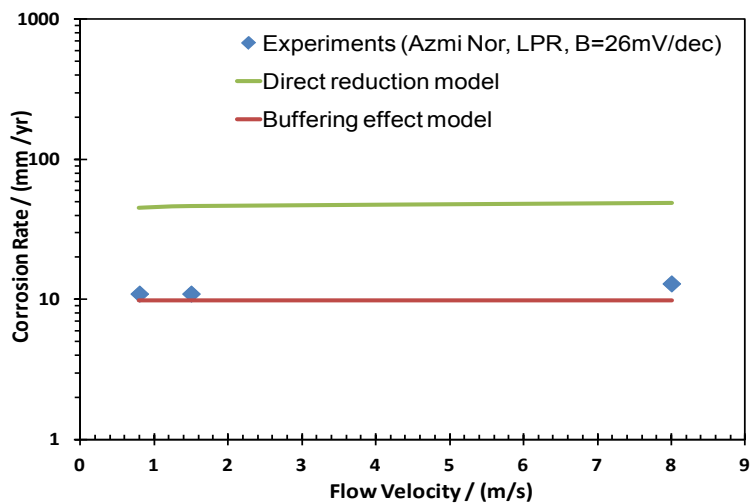


Figure 62: Comparison between experimental and predicted corrosion rates at 25°C, pH3.0, 80 bar pCO₂, 1 wt.% NaCl, X65. Experimental data taken from ICMT database.

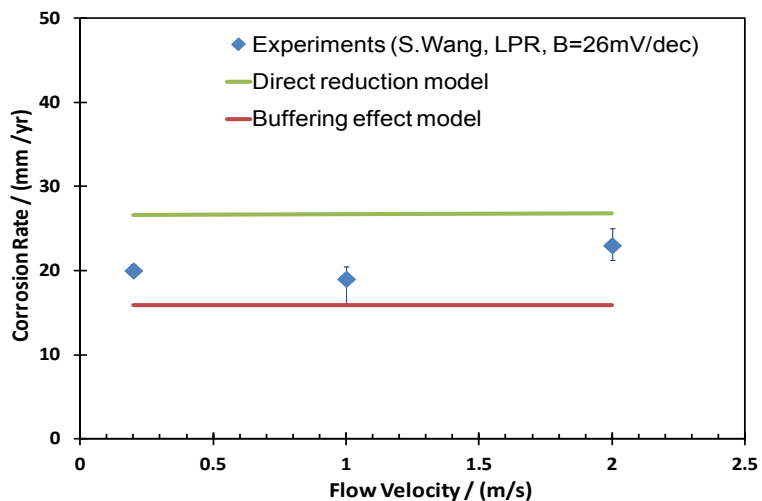


Figure 63: Comparison between experimental and predicted corrosion rates at 60°C, 10 bar pCO₂, pH 5.0, 1 wt.% NaCl, AISI 1018. Error bars represent maximum and minimum experimental values. Experimental data taken from Wang's publication. [52]

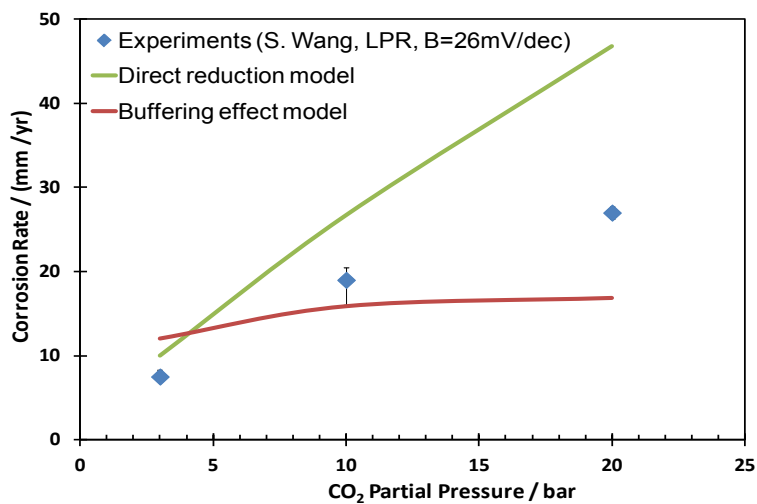


Figure 64: Comparison between experimental and predicted corrosion rates at 60°C, pH5.0, 1 m/s, 1 wt.% NaCl, AISI 1018. Error bars represent maximum and minimum experimental values. Experimental data taken from Wang's publication. [52]

Similarity was also achieved between both model predictions and the experimental data at low concentration HAc for a range of temperatures from 22°C to 60°C (Figure 65 – Figure 67). Clearly, the presence of HAc promotes the corrosion rates, especially at elevated temperature. At higher concentrations of HAc, the direct reduction model overpredicts the corrosion rates while the buffering effect model provides a reasonable match of corrosion rate as compared to experimental data (Figure 68).

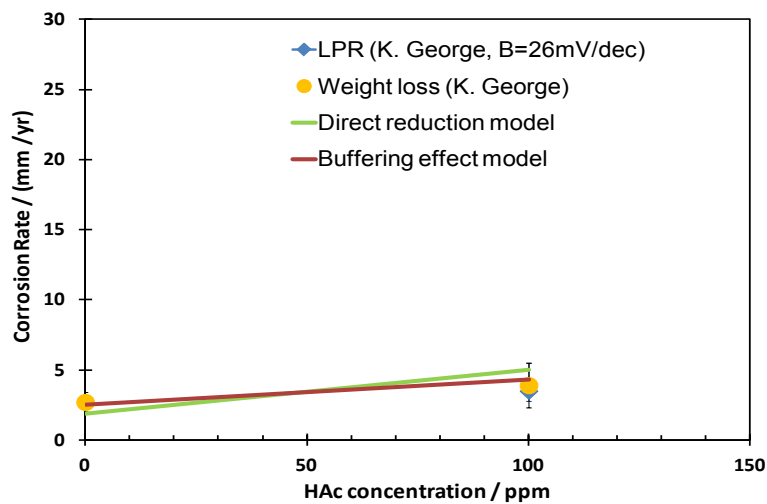


Figure 65: Comparison between experimental and predicted corrosion rates at 22°C, 1 bar pCO₂, pH4.0, 3 wt.% NaCl, 1000 rpm, X65. Error bars represent maximum and minimum experimental values. Experimental data taken from George's publication). [58]

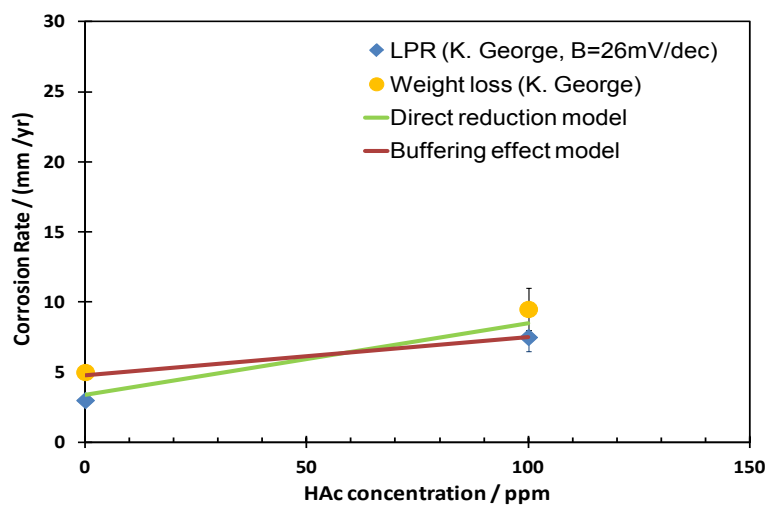


Figure 66: Comparison between experimental and predicted corrosion rates at 40°C, 1 bar pCO₂, pH4.0, 3 wt.% NaCl, 1000 rpm, X65. Error bars represent maximum and minimum experimental values. Experimental data taken from George's publication). [58]

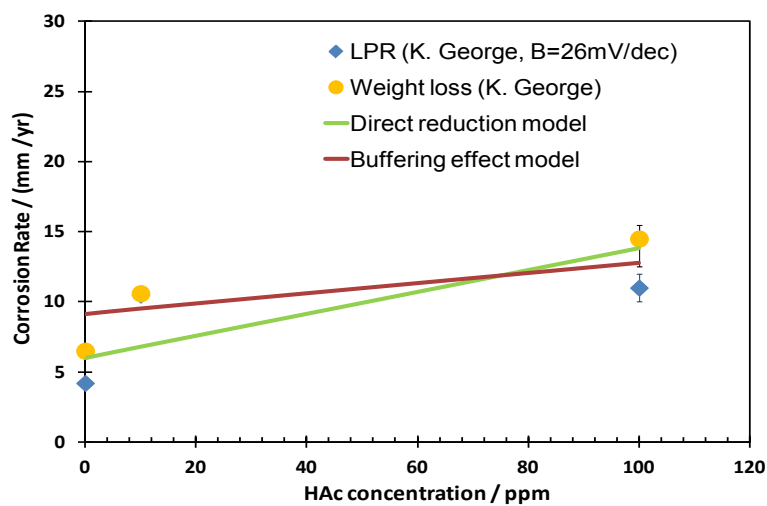


Figure 67: Comparison between experimental and predicted corrosion rates at 60°C, 1 bar pCO₂, pH4.0, 3 wt.% NaCl, 1000 rpm, X65. Error bars represent maximum and minimum experimental values. Experimental data taken from George's publication). [58]

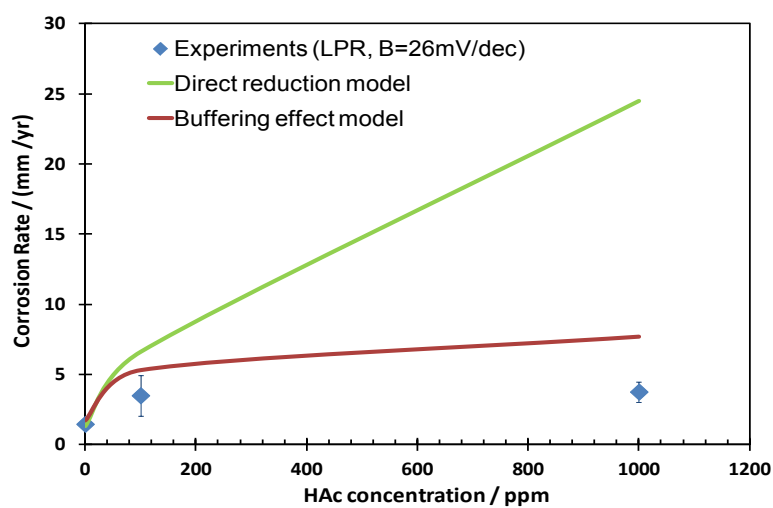


Figure 68: Comparison between experimental and predicted corrosion rates at 25°C, 1 bar total pressure, saturated N₂ solution, pH4.0, 3 wt.% NaCl, 1000 rpm, X65. Error bars represent standard deviation of the experimental values.

Table 23 shows a summary of the comparisons between experimental and predicted corrosion rates. In most of cases, the buffering effect model provides better corrosion rate predictions compared to the direct reduction model.

Table 23: Summary of the comparison between experimental and predicted corrosion rates.

Conditions	Direct reduction model	Buffering effect model
1 bar total pressure, 25°C	Overpredicted at pH2 and pH3 Well predicted at pH4 to pH6	Better predicted at pH2 and pH3 Well predicted at pH4 to pH6
10 bar total pressure, 25°C	Well predicted at pH4 to pH5 Overpredicted at pH3 to pH6	Well predicted at pH3 to pH6
80 bar total pressure, 25°C	Overpredicted at different flow velocities	Well predicted at different flow velocities
10 bar total pressure, pH5, 60°C	Overpredicted at different flow velocities	Slightly underpredicted at different flow velocities
60°C, pH5	Overpredicted at 10 and 20 bar pCO ₂	Well predicted at 10 bar pCO ₂ Underpredicted at 20 bar pCO ₂
22°C, pH4, 1 bar pCO ₂	Well predicted up to 100 ppm of HAc	Well predicted up to 100 ppm of HAc
40°C, pH4, 1 bar pCO ₂	Well predicted up to 100 ppm of HAc	Well predicted up to 100 ppm of HAc
60°C, pH4, 1 bar pCO ₂	Well predicted up to 100 ppm of HAc	Well predicted up to 100 ppm of HAc
25°C, pH4, Without CO ₂	Well predicted up to 100 ppm of HAc Overpredicted at 1000 ppm of HAc	Well predicted up to 100 ppm of HAc Better predicted at 1000 ppm of HAc

6.5 Conclusions

- The buffering effect model was developed based on the buffering effect mechanism, using FREECORP, a theoretical platform developed by the Institute for Corrosion and Multiphase Technology.
- The new buffering effect model is much simpler compared to the direct reduction model.
- By removing the direct reduction of HAc and carbonic acid, the new buffering effect model is able to provide a reasonable corrosion rate prediction for a broad range of environmental conditions, at least as good as the old direct reduction model.

CHAPTER 7: CONCLUSIONS AND RECOMMENDATIONS

7.1 Conclusions*7.1.1 Corrosion mechanism of mild steel in aqueous HAc environment*

- The dominant cathodic reaction mechanism related to the reduction of HAc on steel is the so called buffering effect.
- The presence of HAc only affects the cathodic limiting current due to the ability of HAc to provide hydrogen ions by its dissociation, when they are consumed at the metal surface.
- HAc concentration has no influence on the charge transfer cathodic current since no direct reduction of acetic acid can be detected. Hydrogen ions are the dominant cathodic reactants reduced at the metal surface. A change of pH leads to a change of the cathodic charge transfer current, irrespective of whether acetic acid is present.

7.1.2 Corrosion mechanism of mild steel in aqueous CO₂ environment.

- The dominant cathodic reaction mechanism related to the reduction of carbonic acid on steel is the buffering effect.
- The presence of carbonic acid only affects the cathodic limiting current due to the ability of carbonic acid to provide the hydrogen ions by dissociation, when they are consumed at the metal surface.
- Carbonic acid concentration has a negligible effect on the charge transfer cathodic current since the direct reduction of carbonic acid is insignificant. Hydrogen ions

are the dominant cathodic reactants reduced at the metal surface, irrespective of whether carbonic acid is present.

7.1.3 Corrosion mechanism of mild steel in weak acid environment.

- The buffering effect mechanism could be generally applied to aqueous weak carboxylic acids.
- Other weak acids that have a simple molecular configuration, such as H₂S, and H₂O can be directly reduced at the steel surface. The direct reduction of weak acids that have more complicated molecular configurations such as acetic acid, carbonic acid and formic acid can be disregarded.

7.1.4 Corrosion prediction model

- An electrochemical corrosion model based on the theory of the buffering effect mechanism was developed in this project, in order to predict the corrosion rates of mild steel in aqueous CO₂ and HAc environments.
- By assuming only the reduction of hydrogen ions at the steel surface and the “buffering effect” coming from carbonic acid and HAc via their dissociation, the buffering effect model is able to provide satisfactory predictions for a broad range of environmental conditions.

7.2 Recommendations for future research

Suggestions for further research are provided below:

- The present experimental work is limited to 10 bars pCO₂ and mostly done at 25°C. The buffering effect hypothesis could be tested at higher temperatures and pressures.
- Other material such as titanium could also be used to investigate the mechanism. The charge transfer current produced by the reduction of hydrogen ions on titanium could be examined without interference from the dissolution reaction.
- Compare with additional corrosion data to validate and calibrate the buffering effect model, particularly at higher temperatures and pressures.
- The calibrating parameters could be optimized by using a parameter-fitting algorithm such as a non-linear Simplex method to improve the prediction.
- Implement the buffering effect mechanism in FREECORP and MULTICORP (a more elaborate corrosion prediction model developed by ICMT).
- The “buffering effect” mechanism hypothesis could be further tested with other weak acids such as: hydrogen selenide (H₂Se), phenol (C₆H₅OH) and benzene thiol (C₆H₅SH). Very similar to H₂S in terms of molecular structure and chemistry, it can be hypothesized that the ability of H₂Se to form isostructural iron chalcogenides facilitates its direct reaction with iron. On the other hand, non-carboxylic acid such as phenol and benzene thiol will provide a broad range of structural complexity - with the presence of -OH or -SH group attached to a

hydrocarbon - and thus would be good candidates for further corrosion mechanism studies.

- Molecular modeling methods could be employed to model the behavior of different species when adsorbed on the steel surface. For example, atomic scale adsorption mechanism of weak acids on the iron surface could be characterized by using the density functional theory [83].

REFERENCES

- [1] M. Kermani and A. Morshed, "Carbon dioxide corrosion in oil and gas production - A compendium," *Corrosion*, vol. 59, no. 8, pp. 659-683, 2003.
- [2] S. N. Smith and M. W. Joosten, "Corrosion of carbon steel by H₂S in CO₂ containing oilfield environments," in *Proc. Corrosion*, San Diego, CA, 2006, paper no. 06115.
- [3] B. Hedges, K. Sprague, T. Bieri and H. Chen, "A review of monitoring and inspection techniques for CO₂ & H₂S corrosion in oil & gas production facilities: Location, location, location!," in *Proc. Corrosion*, San Diego, CA, 2006, paper no. 06120.
- [4] T. Barth, "Organic acids and inorganic ions in waters from petroleum reservoirs, Norwegian continental shelf: a multivariate statistical analysis and comparison with American reservoir formation waters," *Applied Geochemistry*, vol. 6, pp. 1-15, 1991.
- [5] T. I. Utvik, "Chemical characterization of produced water from four offshore oil production platforms in the North Sea," *Chemosphere*, vol. 39, no. 15, pp. 2593-2606, 1999.
- [6] P. Menaul, "Causative agents of corrosion in distillate field," *The oil and gas journal*, vol. 43, no. 27, pp. 80-81, 1944.
- [7] Y. Gunaltun and D. Larrey, "Correlation of cases of top of the line corrosion with calculated water condensation rates," in *Proc. Corrosion*, Houston, TX, 2000, paper no. 71.
- [8] P. Okafor and S. Nescic, "Effect of acetic acid on CO₂ corrosion of carbon steel in

- vapor-water two-phase horizontal flow," *Chem. Eng. Comm.*, vol. 194, pp. 141-157, 2007.
- [9] S. Nesic, "Key issues related to modelling of internal corrosion of oil and gas pipelines - A review," *Corrosion Science*, vol. 49, pp. 4308-4338, 2007.
- [10] S. Nesic, J. Postlethwaite and S. Olsen, "An electrochemical model for prediction of corrosion of mild steel in aqueous carbon dioxide solutions," *Corrosion*, vol. 52, no. 4, pp. 280-294, 1996.
- [11] B.F.M. Pots, "Mechanistic models for the prediction of CO₂ corrosion rates under multi-phase flow conditions," in *Proc. Corrosion*, New Orleans, LA, 1995, paper no. 137.
- [12] J. O. Bockris and E. Potter, "The mechanism of the cathodic hydrogen evolution reaction," *Journal of the Electrochemical Society*, vol. 99, no. 4, pp. 169-186, 1952.
- [13] M. Stern, "The electrochemical behavior, including hydrogen overvoltage, of iron in acid environments," *Journal of the Electrochemical Society*, vol. 102, no. 11, pp. 609-616, 1955.
- [14] B. Ateya and F. Elnizamy, "Kinetics of the hydrogen evolution reaction on mild steel electrodes in sulfuric acid," *Corrosion Science*, vol. 20, pp. 46-464, 1980.
- [15] S. Trasatti, "Work function, electronegativity, and electrochemical behaviour of metals III. Electrolytic hydrogen evolution in acid solutions," *Electroanalytical Chemistry and Interfacial Electrochemistry*, vol. 39, pp. 163-184, 1972.
- [16] C. de Waard and D. Milliams, "Carbonic acid corrosion of steel," *Corrosion*, vol. 31,

- no. 5, pp. 177-181, 1975.
- [17] E. Remita, B. Tribollet, E. Sutter, V. Vivier, F. Ropital and J. Kittel, "Hydrogen evolution in aqueous solutions containing dissolved CO₂: Quantitative contribution of the buffering effect," *Corrosion Science*, vol. 50, pp. 1433-1440, 2008.
- [18] K. George, "Electrochemical investigation of carbon dioxide corrosion of mild steel in the presence of acetic acid," M.S. thesis, Department of Chemical and Biomolecular Engineering, Ohio University, Athens, OH, 2003.
- [19] Y. Garsany, D. Pletcher, D. Sidorin and W. Hedges, "Quantifying the acetate-enhanced corrosion of carbon steel in oilfield brines," *Corrosion*, vol. 60, no. 12, pp. 1155-1167, 2004.
- [20] S. Nestic, H. Li, J. Huang and D. Sormaz, "An open source mechanistic model for CO₂ / H₂S corrosion of carbon steel," in *Proc. Corrosion*, Atlanta, GA, 2009, paper no. 09572.
- [21] T. Tran, "Revisiting the CO₂ corrosion mechanism," Institute for Corrosion and Multiphase Technology, Ohio Univ., Athens, OH, CCJIP Advisory Board Meeting, Nov. 2010.
- [22] T. Tran, "Investigating acetic acid corrosion mechanism," Institute for Corrosion and Multiphase Technology, Ohio Univ., Athens, OH, CCJIP Advisory Board Meeting, Mar. 2011.
- [23] T. Tran, "Acetic acid corrosion mechanism," Institute for Corrosion and Multiphase Technology, Ohio Univ., Athens, OH, CCJIP Advisory Board Meeting, Oct. 2011.

- [24] T. Tran, "Investigating the corrosion mechanisms in an aqueous CO₂ environment," Institute for Corrosion and Multiphase Technology , Ohio Univ., Athens, OH, CCJIP Advisory Board Meeting, Mar. 2012.
- [25] T. Tran, "Corrosion mechanisms of mild steel in weak acids," Institute for Corrosion and Multiphase Technology , Ohio Univ., Athens, OH, CCJIP Advisory Board Meeting, Oct. 2012.
- [26] T. Tran, "Corrosion mechanisms of mild steel in aqueous CO₂ environment," Institute for Corrosion and Multiphase Technology , Ohio Univ., Athens, OH, CCJIP Advisory Board Meeting, Mar. 2013.
- [27] T. Tran, "CO₂ corrosion mechanism - Buffering effect or direct reduction?," Institute for Corrosion and Multiphase Technology , Ohio Univ., Athens, OH, CCJIP Advisory Board Meeting, Oct. 2013.
- [28] T. Tran, "Corrosion mechanisms of mild steel in weak acids," Institute for Corrosion and Multiphase Technology , Ohio Univ., Athens, OH, CCJIP Advisory Board Meeting, Mar. 2014.
- [29] T. Tran, B. Brown, S. Netic and B. Tribollet, "Investigation of the mechanism for acetic acid corrosion of mild steel," in *Proc. Corrosion*, Orlando, FL, 2013, paper no. 2487.
- [30] T. Tran, B. Brown, S. Netic and B. Tribollet, "Investigation of the electrochemical mechanisms for acetic acid corrosion of mild steel," *Corrosion*, vol. 70, no. 3, pp. 223-229, 2014.

- [31] Y. Choi, D. Duan, S. Jiang, and S. Netic, "Mechanistic modeling of carbon steel corrosion in a MDEA-based carbon dioxide capture process," *Corrosion*, vol. 69, no. 6, pp. 551-559, 2013.
- [32] S. Netic, N. Thevenot, J.-L. Crolet and D. Drazic, "Electrochemical properties of iron dissolution in the presence of CO₂ - Basics revisited," in *Proc. Corrosion*, Denver, CO, 1996, paper no. 3.
- [33] L. G. Gray, B. G. Anderson, M. J. Danysh and P. R. Tremaine, "Effect of pH and temperature on the mechanism of carbon steel corrosion by aqueous carbon dioxide," in *Proc. Corrosion*, Las Vegas, NV, 1990, paper no. 40.
- [34] J. Podesta and A. Arvia, "Kinetics of the anodic dissolution of iron in concentrated ionic media: Galvanostatic and potentiostatic measurements," *Electrochimica Acta*, vol. 10, pp. 171-182, 1965.
- [35] J. O. Bockris, D. Drazic and A. Despic, "The electrode kinetics of the deposition and dissolution of iron," *Electrochimica Acta*, vol. 4, pp. 325-361, 1961.
- [36] D. Drazic and C. Hao, "The anodic dissolution process on active iron in alkaline solutions," *Electrochimica Acta*, vol. 27, no. 10, pp. 1409-1415, 1982.
- [37] L. Felloni, "The effect of pH on the electrochemical behaviour of iron in hydrochloric acid," *Corrosion Science*, vol. 8, pp. 133-148, 1968.
- [38] G. Florianovich, L. Sokolova and Y. Kolotykin, "On the mechanism of the anodic dissolution of iron in acid solutions," *Electrochimica Acta*, vol. 12, pp. 879-887, 1967.

- [39] K. Videm, "Fundamental studies aimed at improving models for prediction of CO₂ corrosion of carbon steels," in *Progress in the understanding and prevention of corrosion, Proceedings from 10th European corrosion congress*, London, 1993.
- [40] D. H. Davies and G. T. Burstein, "The effects of bicarbonate on the corrosion and passivation of iron," *Corrosion*, vol. 36, no. 8, pp. 416-422, 1980.
- [41] S. Netic, G. Solvi and J. Enerhaug, "Comparison of the rotating cylinder and pipe flow tests for flow-sensitive carbon dioxide," *Corrosion*, vol. 51, no. 10, pp. 773-, 1995.
- [42] A. M. Nor, M. Suhor, M. Mohamed, M. Singer and S. Netic, "Corrosion of carbon steel in high CO₂ environment: Flow effect," in *Proc. Corrosion*, Houston, TX, 2011, paper no. 11242.
- [43] E. Wright, K. Efirid, J. Boros and T. Hailey, "Rotating cylinder electrode (RCE) simulation of corrosion in sweet production," in *Proc. Corrosion*, New Orleans, LA, 2008, paper no. 08629.
- [44] G. Schmitt and B. Rothmann, "Studies on the corrosion mechanism of unalloyed steel in oxygen-free carbon dioxide solutions. Part I: Kinetics of the liberation of hydrogen," *Werkstoffe und Korrosion*, vol. 28, p. 816, 1977.
- [45] Y. Choi, F. Farelas, S. Netic, A. Magalhaes and C. de Azevedo Andrade, "Corrosion behavior of deep water oil production tubing material under supercritical CO₂ environment: Part 1 - Effect of pressure and temperature," *Corrosion*, vol. 70, no. 1, pp. 38-47, 2014.

- [46] A. Dugstad, L. Lunde and K. Videm, "Parametric study of CO₂ corrosion of carbon steel," in *Proc. Corrosion*, Houston, TX, 1994.
- [47] H. Fang, "Low temperature and high salt concentration effects on general CO₂ corrosion for carbon steel," M.S. thesis, Department of Chemical and Biomolecular Engineering, Ohio University, Athens, OH, 2006.
- [48] M. H. Nazari, S. R. Allahkaram and M. Kermani, "The effects of temperature and pH on the characteristics of corrosion product in CO₂ corrosion of grade 70 steel," *Materials and Design*, vol. 31, pp. 3559-3563, 2010.
- [49] W. Sun and S. Netic, "Kinetics of corrosion layer formation: Part 1 - Iron carbonate layers in carbon dioxide corrosion," *Corrosion*, vol. 64, no. 4, pp. 334-346, 2008.
- [50] G. Lin, M. Zheng, Z. Bai and X. Zhao, "Effect of temperature and pressure on the morphology of carbon dioxide corrosion scales," *Corrosion*, vol. 62, no. 6, pp. 501-507, 2006.
- [51] S. Hesjevik, S. Olsen and M. Seiersten, "Corrosion at high CO₂ pressure," in *Proc. Corrosion*, Houston, TX, 2003, paper no. 03345.
- [52] S. Wang, K. George and S. Netic, "High pressure CO₂ corrosion electrochemistry and the effect of acetic acid," in *Proc. Corrosion*, New Orleans, LA, 2004, paper no. 04375.
- [53] M. Nordsveen, S. Netic, R. Nyborg and A. Stangeland, "A mechanistic model for carbon dioxide corrosion of mild steel in the presence of protective iron carbonate films - Part 1: Theory and verification," *Corrosion*, vol. 59, no. 5, pp. 443-456,

2003.

- [54] C. de Waard, U. Lotz and D. E. Milliams, "Predictive model for CO₂ corrosion engineering in wet natural gas pipelines," *Corrosion*, vol. 47, no. 12, pp. 976-985, 1991.
- [55] L. G. Gray, B. G. Anderson, M. J. Danysh and P. R. Tremaine, "Mechanisms of carbon steel corrosion in brines containing dissolved carbon dioxide at pH4," in *Proc. Corrosion*, New Orleans, LA, 1989, paper no. 464.
- [56] T. Hurlen, S. Gunvaldsen, R. Tunold, F. Blaker and P. Lunde, "Effects of carbon dioxide on reactions at iron electrodes in aqueous salt solutions," *J. Electroanal. Chem.*, vol. 180, pp. 511-526, 1984.
- [57] B. Linter and G. Burstein, "Reactions of pipeline steels in carbon dioxide solutions," *Corrosion Science*, vol. 41, pp. 117-139, 1999.
- [58] K. George, S. Netic and C. de Waard, "Electrochemical investigation and modeling of carbon dioxide corrosion of carbon steel in the presence of acetic acid," in *Proc. Corrosion*, New Orleans, LA, 2004, paper no. 04379.
- [59] K. George and S. Netic, "Investigation of carbon dioxide corrosion of mild steel in the presence of acetic acid - Part 1: Basic mechanisms," *Corrosion*, vol. 63, no. 2, pp. 178-186, 2007.
- [60] M. Singh and A. Gupta, "Corrosion behavior of mild steel in acetic acid solutions," *Corrosion*, vol. 56, no. 4, pp. 371-379, 2000.
- [61] V. Fajardo, C. Canto, B. Brown, D. Young and S. Netic, "The effect of acetic acid

- on the integrity of protective iron carbonate layers in CO₂ corrosion of mild steel," in *Proc. Corrosion*, New Orleans, LA, 2008, paper no. 08333.
- [62] B. Hedges and L. McVeigh, "The role of acetate in CO₂ corrosion: The double whammy," in *Proc. Corrosion*, San Antonio, TX, 1999, paper no. 21.
- [63] Z. Yin, W. Zhao, W. Lai, C. Yin and S. Zhu, "Film characteristics of carbon steel in simulant solution with the effect of acetic acid and CO₂," *Journal of Materials Engineering and Performance*, vol. 19, no. 5, pp. 693-699, 2010.
- [64] J. Dougherty, "A review of the effect of organic acids on CO₂ corrosion," in *Proc. Corrosion*, New Orleans, LA, 2004, paper no. 04376.
- [65] E. Gulbrandsen and K. Bilkova, "Solution chemistry effects on corrosion of carbon steels in presence of CO₂ and acetic acid," in *Proc. Corrosion*, San Diego, CA, 2006, paper no. 06364.
- [66] Y. Garsany, D. Pletcher, D. Sidorin and W. Hedges, "Quantifying the acetate-enhanced corrosion of carbon steel in oilfield brines," *Corrosion*, vol. 60, no. 12, pp. 1155-1167, 2004.
- [67] J. Crolet, N. Thevenot and A. Dugstad, "Role of free acetic acid on the CO₂ corrosion of steels in *Proc. Corrosion*, San Antonio, TX, 1999, paper no. 24.
- [68] T. Hurlen, S. Gunvaldsen and T. Blaker, "Effects of buffers on hydrogen evolution at iron electrodes," *Electrochimica Acta*, vol. 29, no. 8, pp. 1163-1164, 1984.
- [69] M. Matos, C. Canhoto, M. Bento and M. Geraldo, "Simultaneous evaluation of the dissociated and undissociated acid concentrations by square wave voltammetry using

- microelectrodes," *Journal of Electroanalytical Chemistry*, vol. 647, pp. 144-149, 2010.
- [70] G. Zhang and Y. Cheng, "On the fundamentals of electrochemical corrosion of X65 steel in CO₂-containing formation water in the presence of acetic acid in petroleum production," *Corrosion Science*, vol. 51, pp. 87-94, 2009.
- [71] M. Singer, B. Brown, A. Camacho and S. Netic, "Combined effect of carbon dioxide, hydrogen sulfide, and acetic acid on bottom-of-the-line corrosion," *Corrosion*, vol. 67, no. 1, 2011.
- [72] M. Singer, D. Hinkson, Z. Zhang, H. Wang and S. Netic, "CO₂ top-of-the-line corrosion in presence of acetic acid: A parametric study," *Corrosion*, vol. 69, no. 7, pp. 719-735, 2013.
- [73] V. Levich, *Physicochemical hydrodynamics*, Englewood Cliffs, NJ: Prentice Hall, 1962.
- [74] M. Eisenberg, C. Tobias and C. Wilke, "Ionic mass transfer and concentration polarization at rotating electrodes," *Journal of the Electrochemical Society*, vol. 101, no. 6, pp. 306-320, 1954.
- [75] Y. Kharaka, E. Perkins, W. Gunter, J. Debral and C. Bamford, *Solmineq 88: A computer program for geochemical modeling of water rock interactions*, Menlo Park, CA: Alberta Research Council: U.S. Geological Survey, 1989, pp. 117-127.
- [76] J. Dominguez, "Corrosion inhibition in sour environments," Institute for Corrosion and Multiphase Technology, Ohio Univ., Athens, OH, CCJIP Advisory Board

Meeting, Mar. 2014.

- [77] Y. Zheng, B. Brown and S. Nescic, "Electrochemical study and modeling of H₂S corrosion of mild steel," *Corrosion*, vol. 70, no. 4, pp. 351-365, 2014.
- [78] J. Kittel, F. Ropital, F. Grosjean, E. Sutter and B. Tribollet, "Corrosion mechanisms in aqueous solutions containing dissolved H₂S. Part 1: Characterisation of H₂S reduction on a 316L rotating disc electrode," *Corrosion Science*, vol. 66, pp. 324-329, 2013.
- [79] J. Lee, "A mechanistic modeling of CO₂ corrosion of mild steel in the presence of H₂S," Ph.D. dissertation, Department of Chemical and Biomolecular Engineering, Ohio University, Athens, OH, 2004.
- [80] Y. Zheng, "Electrochemistry of aqueous H₂S/ CO₂ corrosion," Institute for Corrosion and Multiphase Technology, Ohio Univ., Athens, OH, CCJIP Advisory Board Meeting, Oct. 2012.
- [81] K. Sattler, Handbook of nanophysics: Principles and methods, CRC Press, 2011.
- [82] A. Lennie, S. Redfern, P. Schofield and D. Vaughan, "Synthesis and Rietveld crystal structure refinement of mackinawite, tetragonal FeS," *Mineralogical Magazine*, vol. 59, pp. 677-683, December.
- [83] D. Jiang and E. Carter, "Adsorption, diffusion, and dissociation of H₂S on Fe (100) from first principles," *J. Phys. Chem. B.*, vol. 108, pp. 19140-19145, 2004.
- [84] K. Vetter, Electrochemical kinetics. Theoretical and experimental aspects, New York: Academic Press, 1967.

APPENDIX A: CORROSION RATE CALCULATION

A.1 Linear polarization resistance (LPR)

The principle of LPR is to polarize the steel surface ± 5 mV vs. the open circuit potential and measure the current. The slope of the potential vs. current plot is the polarization resistance. The corrosion rate can be obtained using the following equation:

$$CR = \frac{0.026 \times 1.16}{(R_p - R_s) \times A} \quad (46)$$

Where:

CR : calculated corrosion rate (mm/y);

R_p : polarization resistance, measured by LPR (Ω);

R_s : solution resistance, measured by EIS (Ω);

A : surface area (m^2).

A.2 Weight loss method

The corrosion rate measured by the weight loss method is calculated by equation 47:

$$CR = \frac{m_{loss} \times conversion_factor}{\rho_{Fe} \times A \times t} \quad (47)$$

Where:

CR : calculated corrosion rate (mm/y);

m_{loss} : mass loss of the sample (measured in grams ± 0.001 g);

ρ_{Fe} : density of iron (equal to 7.85 g/cm³);

A : surface area (measured in cm² $\pm 10\%$);

t : time (± 30 minutes).

APPENDIX B: EQUIPMENT IMPROVEMENT AND TEST REPRODUCIBILITY

The goal of this appendix is to show the difficulty of conducting experiments in the autoclave and improvements made to ensure the reproducibility of the experiments conducted in the stainless steel autoclave using a stationary working electrode and to make sure that the experiment at one bar CO₂ conducted in the glass cell can be reproduced in the autoclave.

The first set of experiments in the autoclave attempted to replicate the ones in the glass cell at one bar CO₂. Figure 69 shows a discrepancy between glass cell and autoclave results at one bar CO₂. The main difference between experiments conducted in the glass cell and the ones conducted in the autoclave was flow velocity. The glass cell experiment was conducted using an RCE at 1000 rpm and the autoclave experiment was conducted using a stationary electrode and a stirring impeller at 100 rpm. Flow velocity was expected to have an effect only on the limiting current, but not the charge transfer current. However, as shown in Figure 69, the charge transfer current was not consistent between experiments.

Experiments were then conducted in the glass cell without rotation (only a magnetic stir bar was used to stir the solution) to replicate the condition in the autoclave and to troubleshoot problems. Similar discrepancies were still present (Figure 70). Fortunately, it was possible to visually observe the experiments carried out in the glass cell (Figure 71a). It was found that at low stirring speed of the magnetic bar, bubbles were able to form on the metal surface (Figure 71b). At higher stirring speed, the formation of bubbles was prevented during electrochemical measurements (Figure 71c).

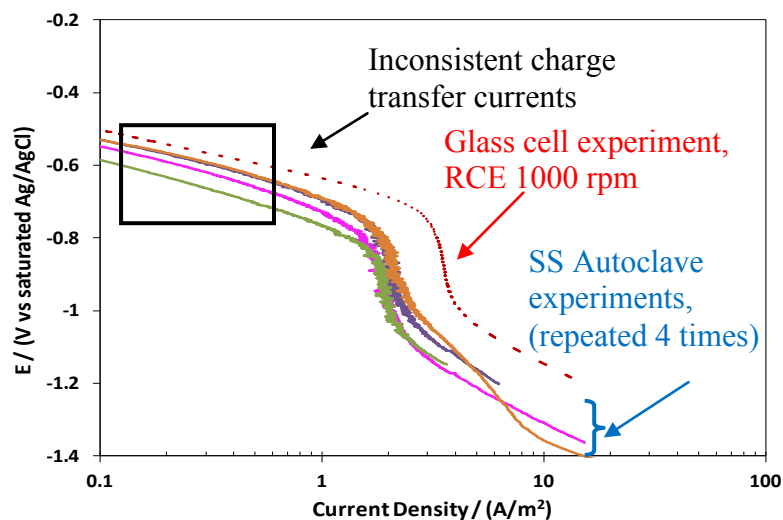


Figure 69: Comparison between glass cell vs. SS autoclave experiment. Inconsistent charge transfer currents at 1 bar $p\text{CO}_2$ experiment, pH4.0, 25°C , 3 wt% NaCl in the SS autoclave using a stationary electrode, impeller stirring speed 100rpm.

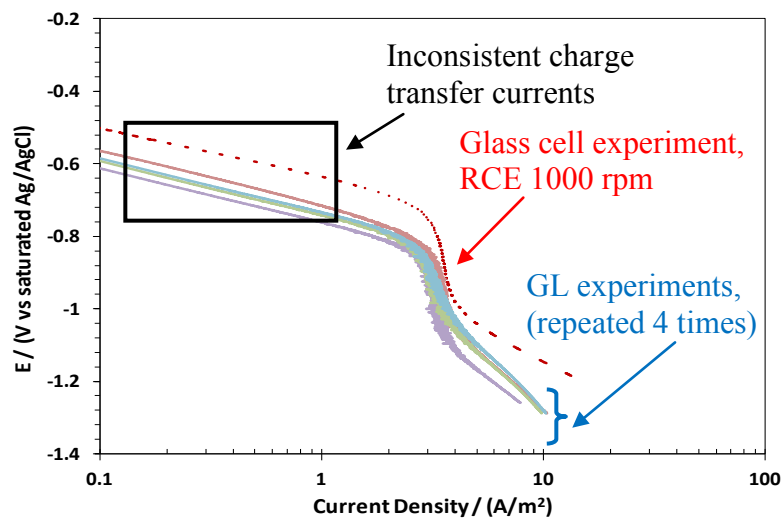


Figure 70: Comparison between using a RCE vs. without rotation. Inconsistent charge transfer currents at 1 bar CO_2 experiment, pH4.0, 25°C , 3 wt% NaCl in the glass cell, without rotation, using magnetic stirring bar.

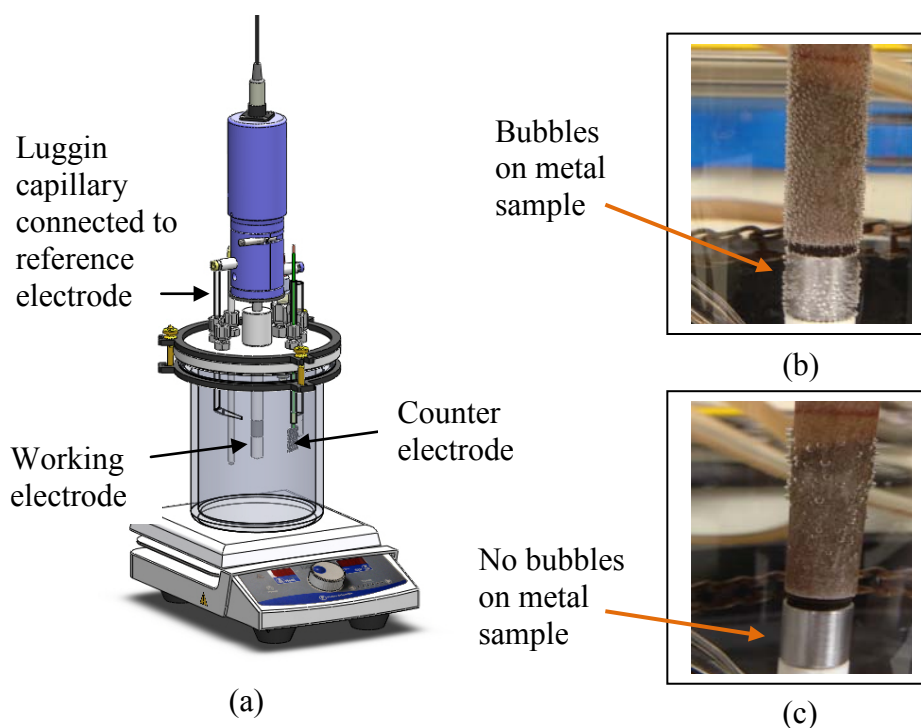


Figure 71: Experiments conducted in the glass cell, without rotation: (a) Schematic of glass cell; (b) Bubble formation on sample at low stirring speed; (c) No bubbles on the sample at high stirring speed.

One of the difficulties associated with conducting an experiment in the autoclave, even at one bar CO_2 , is that it is impossible to visually observe what is happening inside because the autoclave body is made from stainless steel. If the cause of the inconsistency was due to the presence of bubbles, it is necessary to know at what stirring speed bubbles could be prevented.

An “autoclave” body was built from acrylic to solve this problem (Figure 72). The same lid and electrodes used for the stainless steel autoclave were used for the acrylic “autoclave”. It was possible to then visually observe the electrode inside the acrylic autoclave.

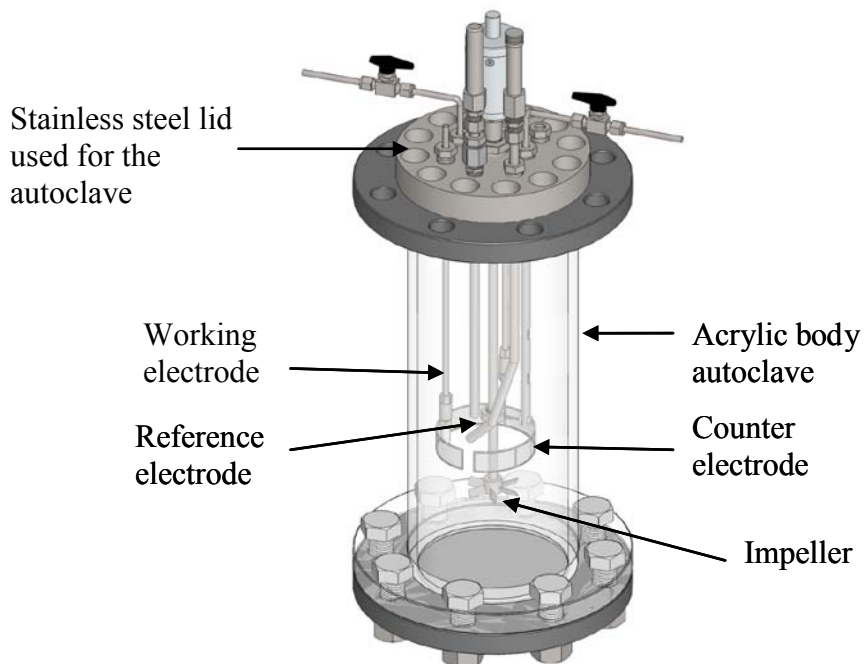


Figure 72: Schematic of the acrylic autoclave

Using the impeller, a stirring speed of 800 rpm was found to not only prevent the formation of bubbles at the metal surface, but also to provide similar mass transfer compared to a glass cell RCE at 1000 rpm. A consistent charge transfer current was reproducible in the acrylic autoclave (Figure 73). Similar results were obtained in the stainless steel autoclave by using the 800 rpm stirring speed. This speed was sufficient to prevent bubble formation at the metal surface, thus improving the reproducibility (Figure 74). This stirring speed was used in the experiments presented in chapter 5 to investigate the effect of pH and carbonic acid concentration on the charge transfer current.

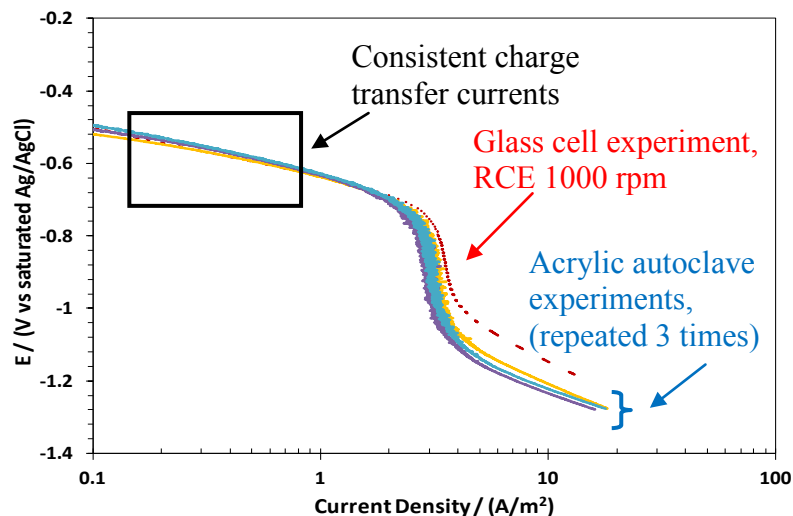


Figure 73: Comparison between glass cell vs. acrylic autoclave experiments. Consistent charge transfer currents at 1 bar CO₂ experiment, pH4.0, 25°C, 3 wt% NaCl, in the acrylic autoclave using a stationary electrode, impeller stirring speed 800rpm.

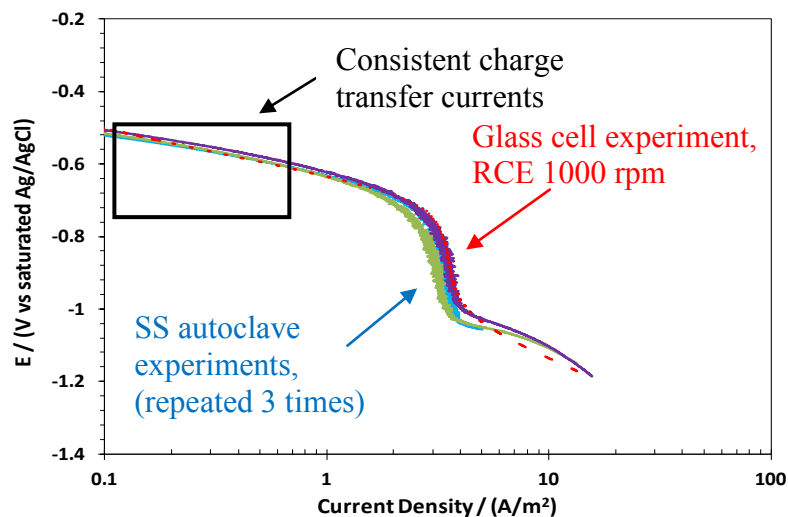


Figure 74: Comparison between glass cell vs. SS autoclave experiments. Consistent charge transfer currents at 1 bar CO₂ experiment, pH4.0, 25°C, 3 wt% NaCl, in the SS autoclave using a stationary electrode, impeller stirring speed 800rpm.

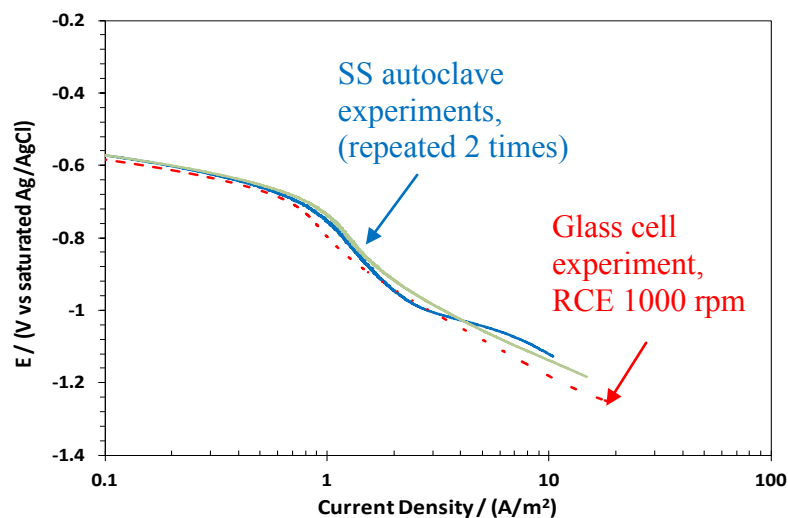


Figure 75: Comparison between glass cell vs. SS autoclave experiments. Consistent charge transfer currents at 1 bar CO_2 experiment, pH5.0, 25°C , 3 wt% NaCl, in the SS autoclave using a stationary electrode, impeller stirring speed 800rpm.

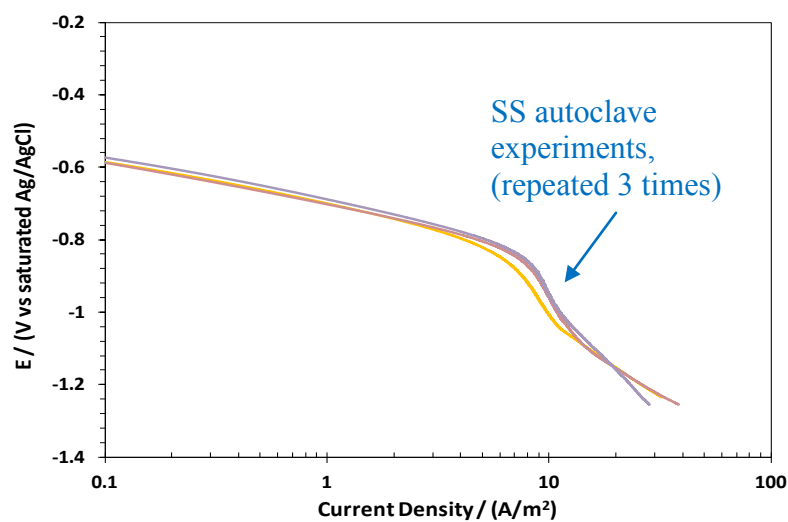


Figure 76: Reproducible charge transfer currents at 10 bar CO_2 experiment, pH5.0, 25°C , 3 wt% NaCl in the SS autoclave using a stationary electrode, impeller stirring speed 800rpm.

In summary, the autoclave procedures have been modified and now provide reproducible results. Experiments at one bar $p\text{CO}_2$ in the glass cell can be replicated in the autoclave with good reproducibility (Figure 74, Figure 75). Consistent charge transfer currents were also found at 10 bar of CO_2 (Figure 76).

Other repeated tests for acetic acid and carbonic acid are shown in Figure 77 - Figure 91.

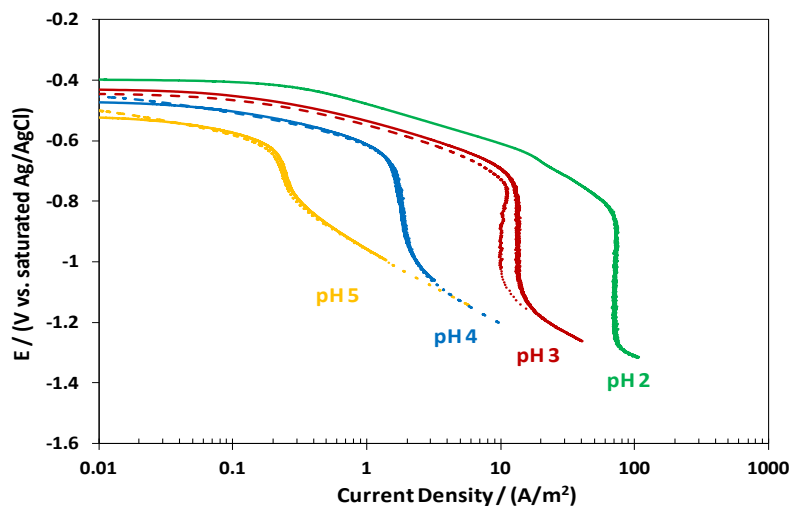


Figure 77: Repeated potentiodynamic sweeps using a SS304 for different pH at 25°C, saturated N_2 solution, 3 wt.% NaCl, RCE rotating speed 1000 rpm.

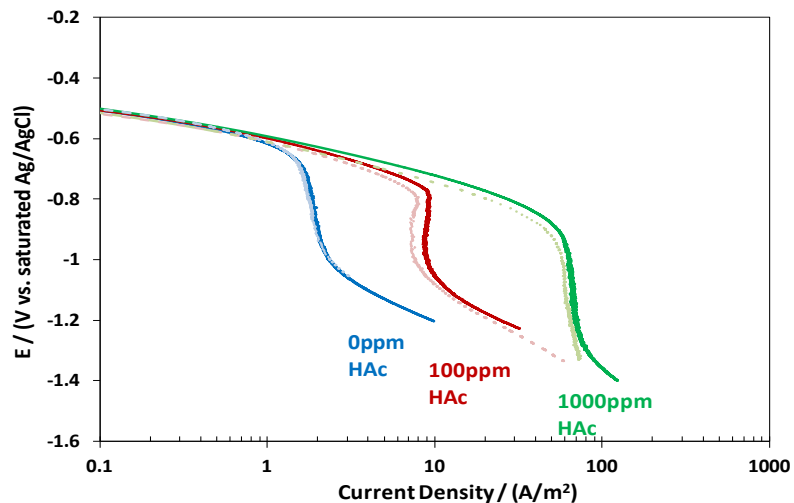


Figure 78: Repeated potentiodynamic sweeps using a SS304 for different HAc concentrations at 25°C, saturated N₂ solution, pH4.0, 3 wt.% NaCl, RCE rotating speed 1000 rpm.

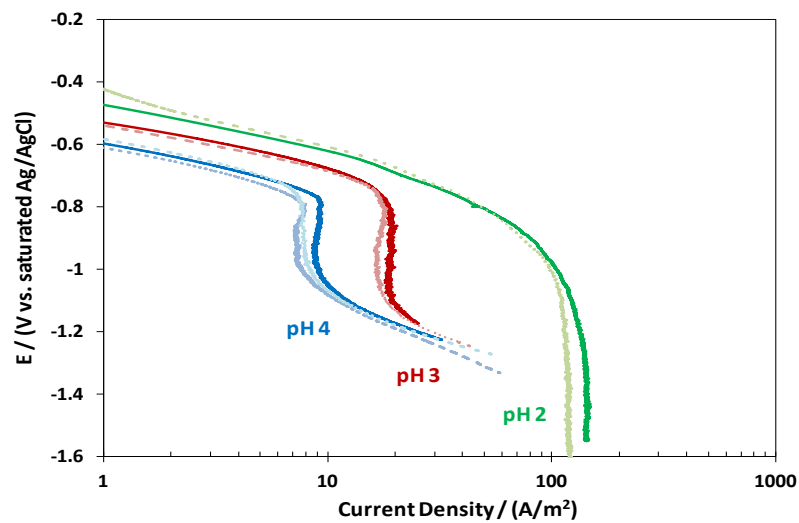


Figure 79: Repeated potentiodynamic sweeps using a SS304 for different pH at 25°C, saturated N₂ solution, 100ppm HAc, 3 wt.% NaCl, RCE rotating speed 1000 rpm.

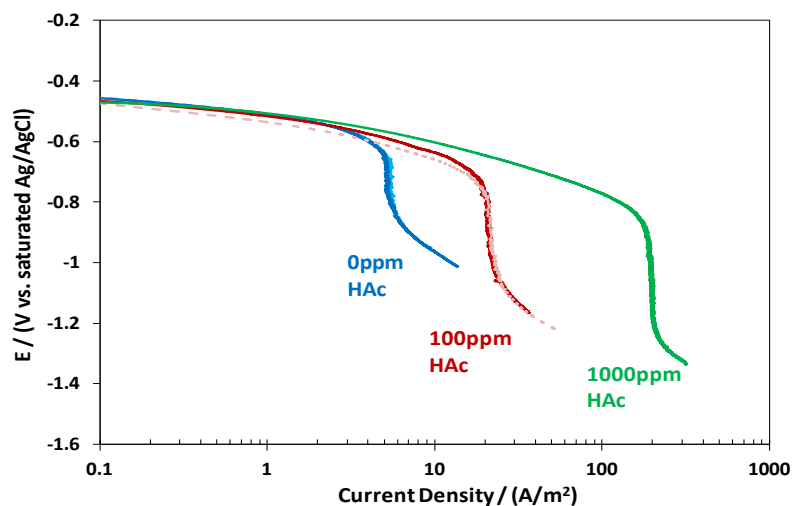


Figure 80: Repeated potentiodynamic sweeps using a SS304 for different HAc concentration at 80°C, saturated N_2 solution, pH4.0, 3 wt.% NaCl, RCE rotating speed 1000 rpm.

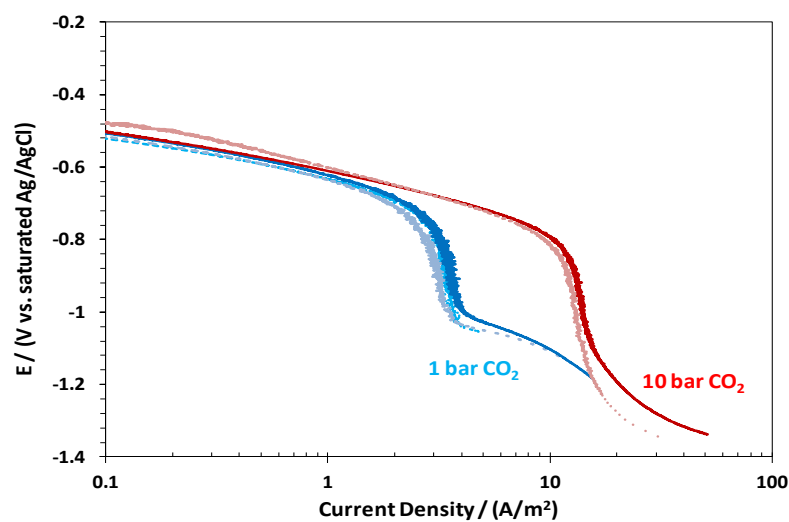


Figure 81: Repeated potentiodynamic sweeps using a SS304 at different pCO_2 , pH4.0, 25°C, 3 wt.% NaCl, impeller stirring speed 800 rpm.

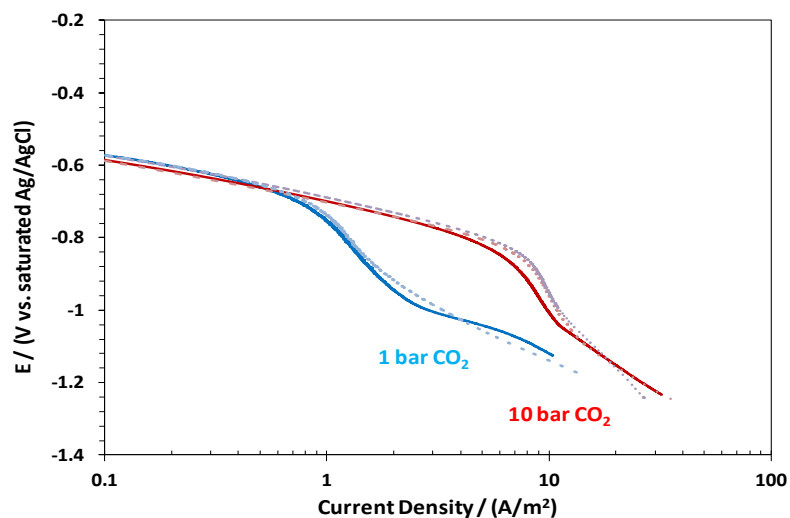


Figure 82: Repeated potentiodynamic sweeps using a SS304 at different pCO₂, pH5.0, 25°C, 3 wt.% NaCl, impeller stirring speed 800 rpm.

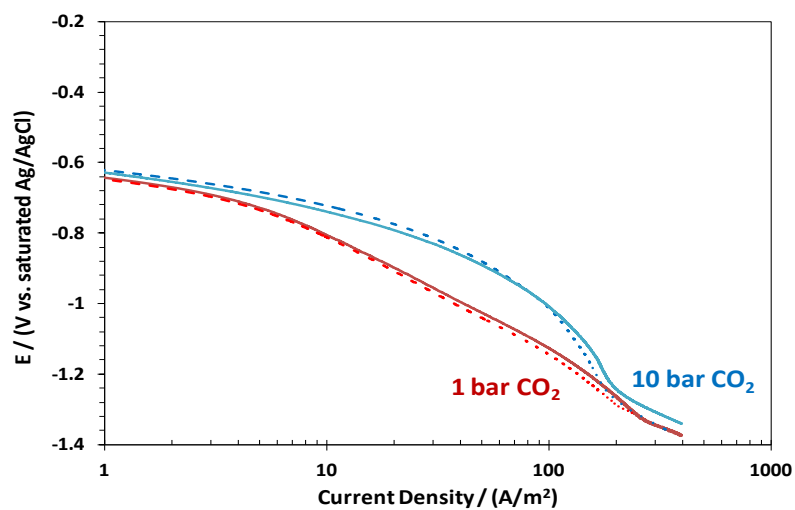


Figure 83: Repeated potentiodynamic sweeps using a SS304 at different pCO₂, pH6.0, 80°C, 3 wt.% NaCl, impeller stirring speed 800 rpm.

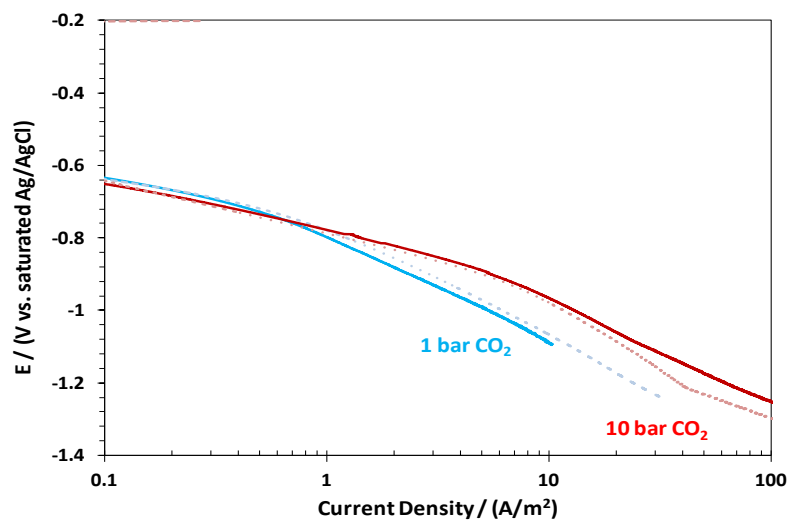


Figure 84: Repeated potentiodynamic sweeps using a SS304 at different pCO_2 , pH6.0, 25°C, 3 wt.% NaCl, impeller stirring speed 800 rpm.

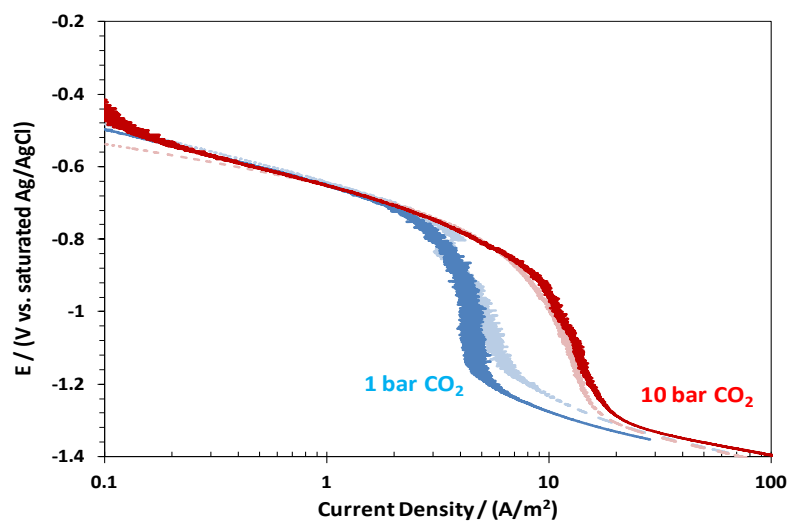


Figure 85: Repeated potentiodynamic sweeps using a Ni200 at different pCO_2 , pH4.0, 25°C, 3 wt.% NaCl, impeller stirring speed 800 rpm.

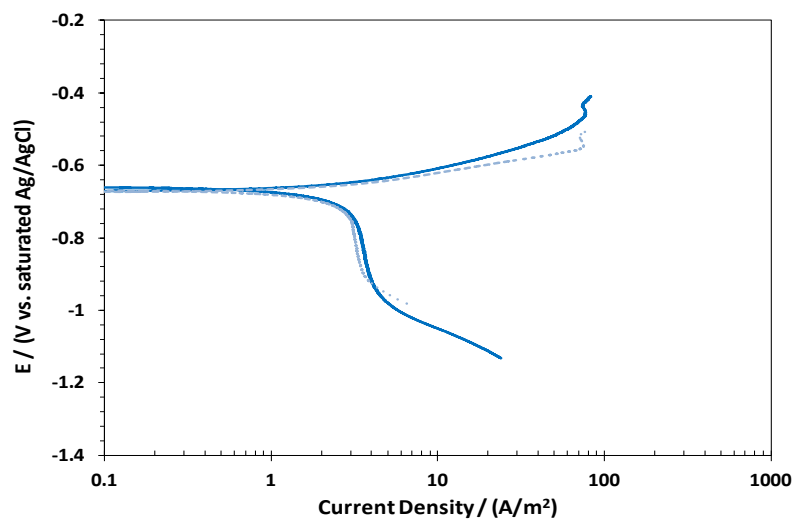


Figure 86: Repeated potentiodynamic sweeps using a X65 at 1 bar pCO₂, pH4.0, 25°C, RCE rotating speed 1000 rpm, 3 wt.% NaCl.

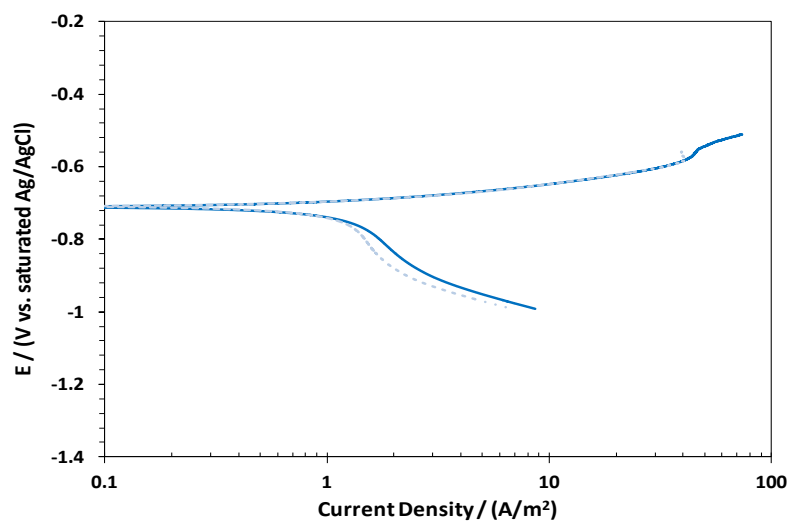


Figure 87: Repeated potentiodynamic sweeps using a X65 at 1 bar pCO₂, pH5.0, 25°C, RCE rotating speed 1000 rpm, 3 wt.% NaCl.

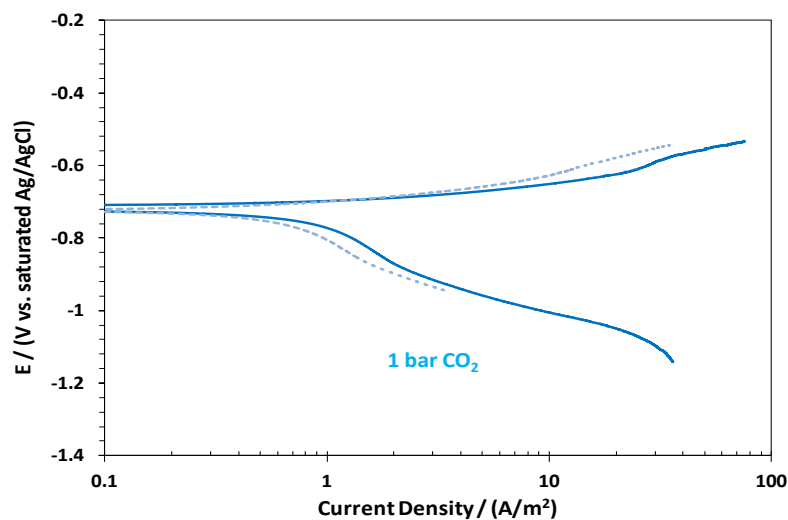


Figure 88: Repeated potentiodynamic sweeps using a X65 at 1 bar pCO₂, pH6.0, 25°C, RCE rotating speed 1000 rpm, 3 wt.% NaCl.

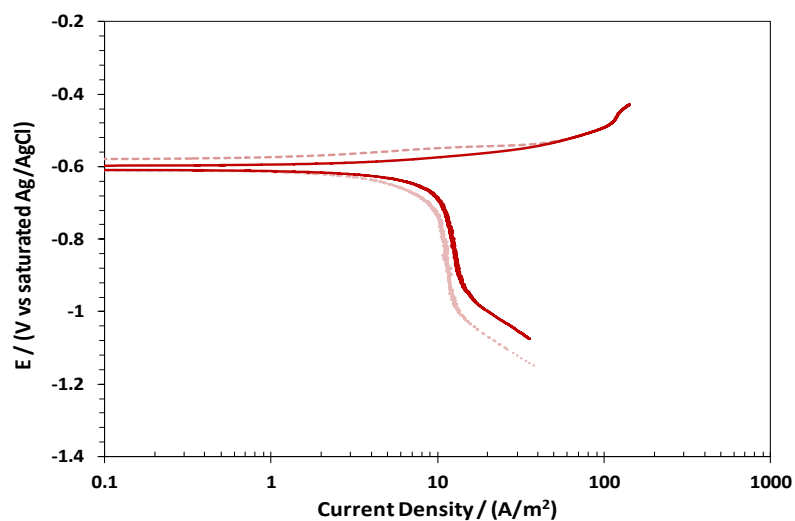


Figure 89: Repeated potentiodynamic sweeps using a X65 at 10 bar pCO₂, pH4.0, 25°C, 3 wt.% NaCl, impeller stirring speed 800 rpm.

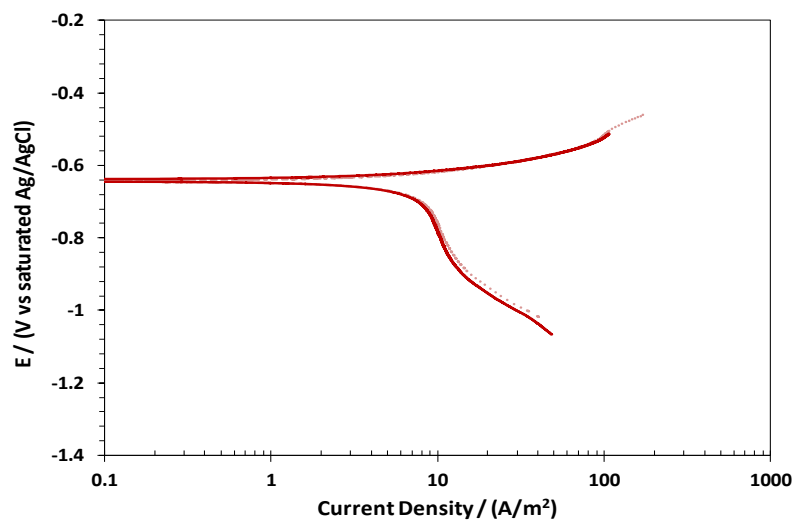


Figure 90: Repeated potentiodynamic sweeps using a X65 at 10 bar pCO₂, pH5.0, 25°C, 3 wt.% NaCl, impeller stirring speed 800 rpm.

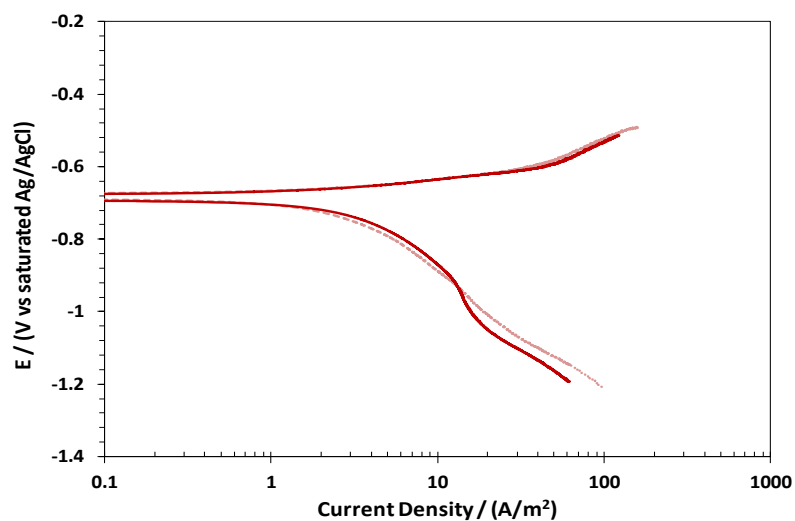


Figure 91: Repeated potentiodynamic sweeps using a X65 at 10 bar pCO₂, pH6.0, 25°C, 3 wt.% NaCl, impeller stirring speed 800 rpm.

APPENDIX C: PERMISSION TO REPRODUCE FIGURES FROM NACE
INTERNATIONAL



NACE International
1440 South Creek Drive
Houston, TX 77084
Tel: 281-228-6219
Fax: 281-228-6319

**Permission to Reproduce Figures,
Photos, and Tables from
Copyrighted Works**

Date: May 5, 2014
Name: Thu Tran Title: Ph.D. Candidate
Company ("Publisher"): Ohio University
Address: 342 West State Street, Athens OH 45701
Tel: 740-593-0283 Fax: 740-593-9949
Email: tt341809@ohio.edu

Material to be Reproduced ("Work"): Please provide a complete description of the material involved. Include the following elements where applicable: publication name, issue date, page number, figure/photo/table number, paper number, conference name, etc.

- "Electrochemical Study and Modeling of H₂S Corrosion of Mild Steel", Yougui Zheng, Bruce Brown, Stojan Nestic - NACE conference, paper No 2426, 2013, Figure 2.
- Same paper in Corrosion Journal, Vol. 70, no. 4, Figure 2, page 354

Reproduction Method ("Publication Media"): Please provide a complete description of how and where the Work will be used. Include the following elements as applicable: publication name, issue, circulation, print run, web site address, conference name, presentation time and place, etc.

It will be used in my dissertation, Ohio University, August 2014

NACE International ("NACE") hereby grants to "Publisher" the right to publish the Work utilizing the Publication Media described above. The publication right granted herein is limited the specific Publication Media described above. To the extent the publication of the Work is to occur by an above-specified date, such as in a particular periodical or at a particular conference, the right granted herein shall automatically terminate upon the date of such occurrence, whether or not the Work is actually published. To the extent the Publication Media is a web site, the publication right is limited to publication at the specific web site URL identified above. Any right granted herein is a limited, non-transferable, non-exclusive right. No other rights in the Work are granted herein.

Publisher shall not edit or modify the Work except to meet the style and graphic requirements of the individual media involved.

The Publisher shall include the following notation with any publication of the Work: © NACE International YEAR.

The Publisher shall include full bibliographic citations of or references to the original NACE source, where applicable.

Publisher shall obtain a copy of the original Work directly from NACE International and shall not utilize copies of the Work from other sources, including the author(s).

To the extent the Work is published on a web site as authorized herein, the Work shall be posted in a file format that does not allow the content of the Work to be easily copied from the Web Site or changed.

As between NACE and Publisher, Publisher acknowledges that NACE owns all rights in the Works.

Publisher shall not be entitled to any compensation for its efforts in promoting the Work.

THE WORK IS PROVIDED "AS IS." ALL EXPRESS OR IMPLIED COVENANTS, CONDITIONS, REPRESENTATIONS OR WARRANTIES, INCLUDING ANY IMPLIED WARRANTY OF MERCHANTABILITY OR FITNESS FOR A PARTICULAR PURPOSE OR CONDITIONS OF ACCURACY, COMPLETENESS OR QUALITY AND THOSE ARISING BY STATUTE OR OTHERWISE IN LAW, ARE HEREBY DISCLAIMED.

Permission to Publish NACE Copy (B)

IN NO EVENT WILL NACE BE LIABLE FOR ANY DIRECT, INDIRECT, PUNITIVE, SPECIAL, INCIDENTAL OR CONSEQUENTIAL DAMAGES IN CONNECTION WITH OR RELATED TO THIS AGREEMENT (INCLUDING LOSS OF PROFITS, USE, DATA, OR OTHER ECONOMIC ADVANTAGE), HOWSOEVER ARISING.

This Agreement and the rights granted herein may be terminated immediately by NACE upon breach of this Agreement by Publisher. Unless earlier terminated, this Agreement and the rights granted herein will automatically terminate 6 months from the Date set forth above. If the Work has not been published within that time period, a new Agreement must be obtained.

Publisher may not, directly or indirectly, sell, assign, sublicense, lease, rent, distribute, or otherwise transfer this Agreement or any rights granted herein, without the prior written consent of NACE.

If any provision of this Agreement is found to be unenforceable, then this Agreement shall be deemed to be amended by modifying such provision to the extent necessary to make it legal and enforceable while preserving its intent. The remainder of this Agreement shall not be affected by such modification.

This Agreement does not create, and shall not be construed to create, any employer-employee, joint venture or partnership relationship between the parties. No officer, employee, agent, servant or independent contractor of either party shall at any time be deemed to be an employee, servant, agent or contractor of any other party for any purpose whatsoever.

This Agreement shall be governed by, and construed and enforced in accordance with, the laws of the State of Texas, without regard to the choice of law provisions of that State.

This Agreement shall only be effective if signed by authorized representatives of both parties. This Agreement constitutes the entire Agreement between the parties with respect to the subject matter of this Agreement. Any change, modification or waiver hereto must be in writing and signed by authorized representatives of both parties.

Other Terms & Conditions: _____

Publisher hereby requests permission to publish the Work described above and agrees to comply with all Terms and Conditions listed above.

Request submitted by:
John Bran
 Printed Name
Ph.D Candidate
 Title
[Signature]
 Signature
05/05/2014
 Date

Request approved by NACE:
Brenda Nitz
 Printed Name
Books Coordinator
 Title
[Signature]
 Signature
May 5, 2014
 Date

Request agreed to by:
Yongqi zheng
 Lead Author Printed Name
Ph.D. student
 Lead Author Title
[Signature]
 Lead Author Signature
05/05/2014
 Date



OHIO
UNIVERSITY

Thesis and Dissertation Services